INTERNATIONAL JOURNAL OF

ENERGY HORIZON

VOLUME: 1 ISSUE: 2
2025

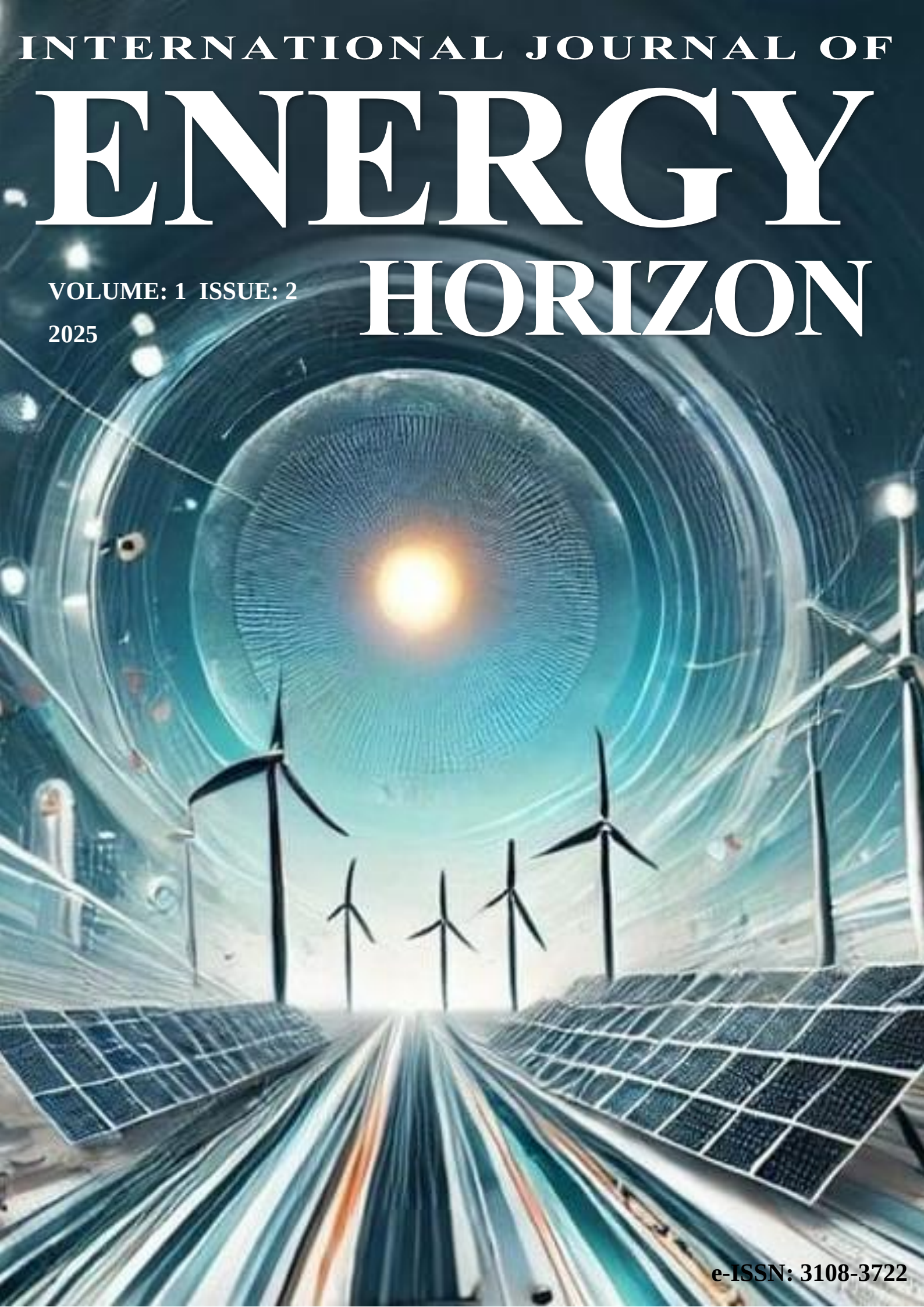

e-ISSN: 3108-3722

Editorial Team

International Journal of Energy Horizon (IJEH)

2025, Volume 1, Issue 2

Contents

International Journal of Energy Horizon 02 (2025) 32-38

International Journal of Energy Horizon

journal homepage: https://dergipark.org.tr/tr/pub/ijeh

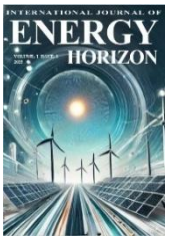

Review Article

Advancing universal energy access: data-driven solutions, and critical importance of interdisciplinary collaboration

Münür Sacit Herdem[1,2,*], Jatin Nathwani[1,3]

[1]Balsillie School of International Affairs (BSIA), Waterloo, ON, Canada
[2]Department of Mechanical Engineering, Adıyaman University, 02040, Adıyaman, Turkey
[3]Department of Management Science, University of Waterloo, 200 University Avenue West, Waterloo, N2L 3G1, ON, Canada
[1]ORCID No:0000-0003-0079-0041
[2]ORCID No:0000-0003-3020-6061

ARTICLE INFO

Article History:

Received:2 September 2025
Accepted:27 September 2025
Available online:30 November 2025

Keywords:

Energy Access
Energy
Renewable Energy
Off-Grid
Artificial Intelligence

ABSTRACT

This critical review paper presents a general overview of the challenges to attain universal energy access and the promise of emerging potential solutions. The barriers to deployment of energy access are described followed by pathways to towards potential solutions. Recommendations include a primary focus on an interdisciplinary approach supported and introduce a novel concept: the "Data in Energy Platform," which leverages data and artificial intelligence (AI) to improve energy access solutions.

1. INTRODUCTION

Energy access is a fundamental component of Sustainable Development Goal (SDG) 7, with the aim to "ensure access to affordable, reliable, sustainable, and modern energy for all" [1]. Key indicators of SDG 7 include Indicator 7.1.1, which measures the proportion of the population with access to electricity, and Indicator 7.1.2, which tracks the proportion of the population primarily relying on clean fuels and technologies for cooking [2]. In 2015, approximately 957.5 million people lacked access to electricity [2]. While significant progress has been made in recent years, energy access remains a pressing issue. The most recent data from 2022 indicate that 685 million people still live without electricity [2]. The challenge extends beyond electricity access. Approximately 2.1 billion people-nearly one-third of the global population-lack access to clean cooking facilities [2]. As a result, many households rely on smoky solid fuels or kerosene, which expose them to harmful indoor air pollution [3]. This pollution is a significant health hazard, contributing to millions of premature deaths annually [4]. Women and children, who spend more time near traditional cooking stoves, are disproportionately affected. Energy access is particularly critical in Sub-Saharan Africa, where many countries face severe challenges in providing modern energy services to their populations. For instance, as of 2022, only 21% of the population in the Democratic Republic of Congo (DRC) had access to electricity, while in Malawi, this figure stood at just 14% [5]. The situation is even more concerning regarding clean cooking access-only 4% of the population in the DRC and a mere 1% in Malawi had access to clean cooking facilities [5]. This lack of access is not unique to these two nations; many other countries in Sub-Saharan Africa experience similar disparities [5,6], highlighting the urgent need for targeted interventions and sustainable solution. While energy access challenges are most severe in less developed regions, they are not confined to these areas. Even in high-income countries, certain communities face significant barriers to reliable energy access, and emerging situations such as natural disasters can further exacerbate these challenges. For instance, Canada struggles with energy access issues in its Indigenous, rural, and remote communities [7, 8]. Approximately 178

*Corresponding author
E-mail address: herdem@adiyaman.edu.tr
journal homepage: https://dergipark.org.tr/tr/pub/ijeh

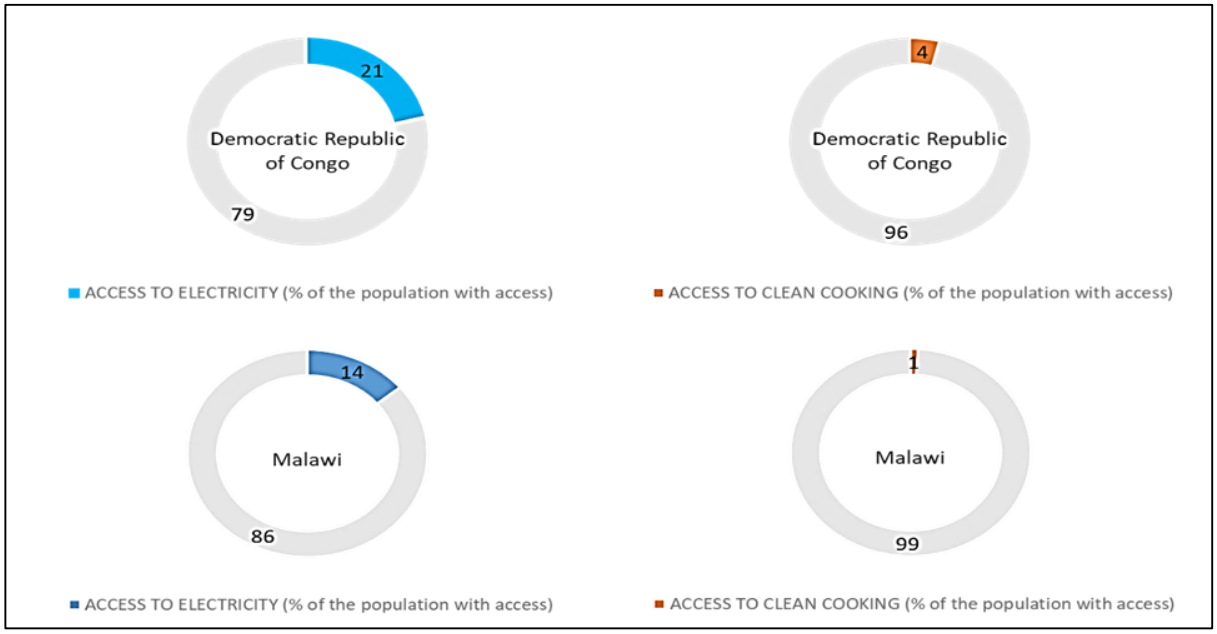

Figure 1. Percentage of the population with access to electricity and cooking in the Democratic Republic of Congo and Malawi (2022). Data sourced from Ref. [5]. For access rates in other countries, refer to Ref. [5]

remote Indigenous and Northern communities remain disconnected from the North American electricity grid and natural gas infrastructure [9]. As a result, these communities primarily rely on diesel fuel for electricity generation and heating, leading to high energy costs, supply vulnerabilities, and environmental concerns [9]. Furthermore, energy access becomes even more critical during emergency situations, such as natural disasters (e.g., earthquakes, wildfires, and extreme winter conditions). These events can disrupt energy infrastructure, leaving affected populations without reliable power and heating. Therefore, strategies to improve energy access must go beyond developing nations and incorporate resilience planning for high-income countries and emergency scenarios. Most existing solutions for energy access have focused on off-grid and decentralized energy systems, which play an increasingly vital role in addressing energy challenges [10]. Hybrid renewable electricity systems have emerged as key components of these solutions, offering flexibility and sustainability. Research in this field has primarily concentrated on three key areas [11]: (i) Deploying off-grid and mini-grid energy systems to support various SDGs; (ii) Assessing the impact of decentralized energy solutions on gender inequalities and disadvantaged communities; (iii) Advancing technologies to enhance the efficiency and scalability of off-grid and mini-grid systems. Beyond electricity access, research on energy access also addresses two critical dimensions [11]: alternative energy options for cooking and new approaches to energy planning, including political and decision-making challenges within energy systems. However, despite these advancements, several key challenges persist. Financial sustainability remains a significant concern, requiring a careful balance between capital expenditure and operational costs to ensure long-term viability [12, 13]. Furthermore, the design of off-grid systems must account for diverse geographical conditions, performance standardization, and modeling limitations [10]. Data is crucial in addressing energy planning, decision-making challenges, and modeling limitations in off-grid decentralized systems. Accurate and reliable data facilitate demand forecasting, storage optimization, and efficient supply management for energy access projects [14]. Additionally, data-driven approaches improve decision-making, reduce risks, and enhance energy projects' scalability and financial viability in underserved communities [14]. For instance, Miles et al. [15] highlight the importance of data in healthcare electrification as a solution to energy access challenges, particularly in the unique demand context of North Kivu. Beyond data, AI is emerging as a powerful tool for designing energy systems in regions lacking access to electricity. AI applications include feature extraction, classification, demand-side management, optimization for energy management, and fault detection [16]. While data and AI offer valuable tools for energy access solutions, the multifaceted nature of energy access challenges necessitates effective interdisciplinary collaboration. Addressing energy access requires integrated engineering, economics, policy, and social sciences efforts to develop holistic and equitable solutions [17]. Numerous technical reports and review papers have examined different aspects of energy access. Kammen et al. [18] analyzed the current energy mix in East Africa and assessed the energy planning efforts of the East African Power Pool (EAPP) within sustainable growth. Their study highlights the EAPP's potential to attract investment and influence both on-grid and off-grid energy initiatives. It demonstrates that East Africa has substantial potential for clean energy development to support economic, social, and environmental goals. Similarly, Corfee-Marlot et al. [19] compiled a report on the challenges and opportunities for delivering clean energy access in Sub-Saharan Africa, focusing on technological advancements, policy reforms, and financing mechanisms. Reviews on off-grid systems are provided in Ref. [20], while sustainable energy access and relevant technologies are highlighted for healthcare facilities in Ref. [21]. However, despite the breadth of existing literature, a significant gap remains in understanding how different disciplines can collaborate to address energy access challenges effectively. Additionally, no dedicated data platform has been designed to integrate interdisciplinary approaches for energy access solutions. This review aims to bridge these gaps. First, we review current energy access solutions. Next, we explore how different disciplines can collaborate to enhance energy access initiatives. Finally, we propose a novel concept: the "Data in Energy Platform," which leverages data and AI to improve energy access solutions. This paper is a guide and foundational resource for organizations and research groups focused on energy access challenges.

2. CURRENT STUDIES AND POTENTIAL SOLUTIONS FOR THE ENERGY ACCESS ISSUE

The research on energy access targets five main areas [11]: decentralized electrification for SDG delivery; equity impacts of distributed services, especially along gender lines; innovation that hardens and scales mini/off-grid systems; pathways to clean cooking; and rethinking planning institutions and the politics that shape energy decisions. Due to their significant advantages, many studies focus on renewable-based, off-grid, and decentralized systems. These advantages include efficient end-use appliances and the potential for significantly reduced costs through low-cost photovoltaics (PVs) [22, 23]; support from available information technologies, particularly mobile phones, and virtual financial services [22]; a substantial decrease in greenhouse gas emissions when replacing diesel generators in regions suffering from inadequate energy access [24]; and a reduction in energy vulnerability in remote, low-income areas lacking sufficient energy access [25]. Of course, the systems' conceptual design, thorough testing, and careful technology selection are critical for fully utilizing renewable-based decentralized systems as solutions for traditional energy access. Building on this foundation, the main efforts of studies on renewable-based off-grid systems have been to develop methodological frameworks and tools that enhance the full utilization of these systems, considering these essential factors. The diversity of global geographies poses significant challenges for the conceptual design and comparison of different off-grid systems. Additionally, energy storage technologies are a key

component of solar and wind-based off-grid systems; thus, evaluating the performance of various energy storage technologies is critical for designing cost-effective, optimal off-grid systems. Considering these factors, Elkadragy et al. [10] developed a data analysis platform and irradiance forecasting models for an off-grid hybrid renewable energy conversion system. The system comprises solar and wind turbine power generators, non-renewable source backup generators, and hybrid battery storage systems consisting of lead-acid and lithium-ion batteries. This system was tested in Sub-Saharan Africa (Uganda) and Nemiah Valley, British Columbia, Canada [10, 26]. Therefore, the studies [10, 26] elucidate the techno-economic challenges of off-grid systems in various global locations. These studies [10, 26] also demonstrate the economic benefits of using hybrid lead-acid and lithium-ion batteries in off-grid systems. Solar off-grid systems have also been investigated in the literature for energy access solutions. Gill-Wiehl et al. drew on a large dataset to examine the scalability and impact of Rwanda's container-based solar PV systems in practice [27]. They assessed how a rapid rollout of these flexible, modular units might serve fast-growing yet resource-constrained communities, combining modeled results with field data across three application areas—water, food, and health—under optimistic and more conservative assumptions. In the optimistic scenario, a single unit could supply daily drinking water for 2,083 people and meet the daily milk consumption of 1,674 people, or fully cover a health clinic's electricity demand. The system itself is a 2 x 2 x 2 m container outfitted with 12 PV modules totaling 3.36 kWp, four 90-Ah GEL/AGM lead-acid batteries, and a 3,000-W charge controller/inverter. Compared to incumbent technologies, this configuration exhibited lower cost variability while minimizing pollutant and greenhouse-gas emissions, indicating a more sustainable option. The researchers have also conducted numerous studies that cover various aspects of off-grid and decentralized systems for regions that lack energy access. One notable investigation by Lee and Callaway [28] investigates the economics and reliability of decentralized solar systems across large spatial scales. Their research focused on stand-alone household solar systems with battery storage in sub-Saharan Africa. They examined how different designs aimed at varying levels of reliability impact system costs and compared these costs to those of national grids designed for equivalent reliability. Moreover, their study considered the effects of changing commodity prices on these cost relationships. Using a fraction of demand served as a measure of reliability, Lee and Callaway developed a multistep optimization process to efficiently compute the least-cost system, considering daily variations in solar resources and the costs of solar and storage components. Furthermore, Szabo et al. [29] provide compelling evidence regarding the cost-effectiveness of solar PV systems compared to diesel-powered electricity generation. Their analysis, covering East Asia, South Asia, and sub-Saharan Africa, reveals that solar systems are more affordable for at least 36% of the unelectrified populations in these regions. By developing geo-referenced estimates of affordability with a high level of resolution, their study identifies unelectrified communities across 71 countries where solar power is a viable alternative, even in competition with low-priced diesel. In addition, Kebir et al. [30] explore the innovative use of second-life batteries combined with solar PVs to provide affordable energy access to primary schools in Kenya. Based on interviews with 12 East African schools, their study assesses various system sizes and configurations. They conducted a techno-economic analysis comparing new and second-life batteries across 48 system scenarios, finding that second-life batteries could reduce the levelized cost of electricity by 5.6–35.3% in 97.2% of the scenarios compared to new batteries and by 41.9–64.5% compared to grid-supplied electricity. Their results show that the small system with a 5 kW solar array and a 5 kWh storage system using second-life batteries has a payback period of 2.9 years. These results in [30] highlight the viability and competitiveness of using second-life batteries for school electrification, significantly reducing costs and waste. The studies mentioned above predominantly focus on renewable-based (mainly solar and wind energies) off-grid systems for energy access. However, Her et al. [31] (2024) conducted a comprehensive study to explore the feasibility of small and micro-modular nuclear reactors for energy access in developing countries. They presented a global analysis assessing regions suitable for nuclear reactor deployment based on physical siting criteria, security, governance, and economic competitiveness. Their findings indicate that technically, reactors in the 1-50 MWe range could serve 70.9% of the populations in developing regions. However, economically, microreactors would not be competitive with renewables and energy storage for 87% of this population due to cost factors. Further diversifying the perspective on energy solutions, another study by Gill-Wiehl et al. [32] focuses on the crucial aspect of the gender-differentiated impact of off-grid solar energy in rural Tanzania. This study uses quantitative surveys and qualitative interviews to investigate the energy justice implications of off-grid solar systems. It critically evaluates and compares the primary goods and capabilities approaches to assess how the distributional benefits of off-grid solar are mediated by gender and class. Interestingly, their case study does not find clear benefits specifically for women or low-income households, suggesting that while off-grid solar usage may be equal, it is not necessarily equitable. The findings highlight the importance of considering gender and class in energy justice, filling a crucial gap in the literature on off-grid solar's impact. The above cited studies focus primarily on power generation from off-grid renewables. However, clean cooking sources and stove technologies are critical to eliminating particulate and carbon monoxide emissions from cooking and preventing several health risks, such as cancer, respiratory infections, and heart disease [33]. Therefore, the literature also addresses the crucial aspect of clean cooking sources and stove technologies for regions, specifically African countries struggling with comprehensive energy access. Gill-Wiehl et al. [34] analyzed the research on the hindrances related to the adoption and consistent use of clean cooking stoves and fuels due to affordability. They examined various affordability aspects of the adoption and regular usage of stoves and fuels, such as initial costs and regular expenses discussed in the clean cooking literature. Their findings revealed various frameworks, definitions, and measurements used in the discussions, with frequent focus on stove prices, fuel expenses, microfinance, and smaller purchase quantities. The researchers suggest financing strategies to address unaffordability should consider how low-income families earn, spend, and save money. They also recommend expanding affordability frameworks to encompass gender, rural/urban disparities, and stove-stacking behavior. Using liquified petroleum gas (LPG) as a clean cooking source as a solution for energy access has also been widely studied. Gill-Wiehl et al. [35] highlight the potential of a community engagement model for public health in promoting the adoption of clean cooking fuels. They propose that this type of community infrastructure model can substantially increase LPG usage when augmented with financial mechanisms like a micro-savings program. This is particularly true in rural, low-income regions. In another study [36], Gill-Wiehl et al. revealed that despite the widespread use of firewood and charcoal, 82% of households preferred LPG. Moreover, their findings suggest that integrating household preferences into clean cooking policies is essential, especially as their data indicates that LPG is preferred and more economical than traditional fuels. When exploring off-grid and clean cooking solutions, researchers have also investigated alternative community-based approaches and critically assessed the limitations of corporate-led market strategies for achieving energy access. Kemabonta and Kammen [37] investigated an alternative approach to addressing energy poverty, focusing on private and community ownership of electricity production factors and emphasizing the importance of economics over mere technical calculations. They argue that traditional interventions often fail by treating energy access as merely a technical issue, neglecting the economic aspects that can empower communities. Their study includes case studies like the Nigerian off-grid mini-grid industry and the Ecoblock pilot project in California, demonstrating how community-based approaches can effectively tackle energy access issues. By prioritizing economic calculation and leveraging community and private property rights in electricity production, their approach suggests a more sustainable and participatory model for addressing energy poverty, moving beyond the limitations of current paradigms that focus primarily on technical solutions. While Kemabonta and Kammen [37] highlight the effectiveness of community-based approaches in empowering local populations and enhancing energy access, Groenewoudt and Romijn [38] provide a contrasting perspective by critically evaluating the corporate-led market approach, which predominates in the Global South. Their review [38] critically assesses the limitations of the corporate-led market approach to off-grid energy access, particularly in the context of the Global South. Their study highlights that while markets facilitate technology diffusion, they prioritize profit over people and the planet, leading to sustainability trade-offs. The authors argue that this market model fails to achieve equitable and sustainable energy access and perpetuates structural injustices by not effectively reaching the poorest or most isolated populations. They propose a more inclusive approach that involves local entrepreneurs, non-profits, and public sectors to negotiate these trade-offs better, suggesting that a pluralistic route might offer a more just and sustainable framework for energy access. This perspective challenges the reliance on foreign-affiliated corporate enterprises and underscores the need for a diversified strategy emphasizing community and local capacities. Reflecting the earlier studies in the literature, various successful energy access projects have been initiated in regions lacking reliable energy sources. These projects generally focus on renewable energy-based decentralized and off-grid systems. Some important activities of these energy access projects [39] can be categorized as follows:

1. **Regional Development and Technical Assessments:** Projects typically focus on identifying energy demand and designing mini-grid systems for diverse communities. This involves comprehensive assessments addressing the water, telecommunications, and energy nexus to enhance productive energy uses.

2. **Strategic Planning and Capacity Building:** These initiatives often include creating platforms for universal electrification that involve developing national and regional plans, extensive training for technical staff, and support for ongoing electrification efforts.

3. **Georeferenced Planning for Universal Access**: Projects aim to develop georeferenced plans to facilitate universal access to electricity, especially targeting remote and isolated areas, to identify and characterize potential consumer units for community and productive usage.

4. **Hybrid Power Systems Design and Evaluation:** These involve designing hybrid power systems that integrate renewable energy generation with battery storage solutions, focused on reducing reliance on traditional diesel generators.

5. **Feasibility Studies and Technical Specifications**: Comprehensive feasibility studies and technical specifications are conducted to review energy options and develop concrete project concepts. These include detailed budgeting and implementation schedules tailored to each community's needs.

3. RECOMMENDATIONS

Traditional studies on energy access have often focused on isolated, siloed solutions, as shown in Sections 2 and 3. However, the energy access challenge is inherently multidimensional, involving aspects such as energy sector governance, technological integration, stakeholder engagement, data collection and analysis, configuration of technology solutions, linkages with other sectors, region-specific customization, financing, social and cultural barriers, planning deficiencies, and limited data availability [13, 40, 41]. Addressing these complexities requires interdisciplinary collaboration [13, 40, 41] and the active participation of diverse stakeholders [42-44]. Figure 2 summarizes traditional and integrated approaches for energy access solutions.

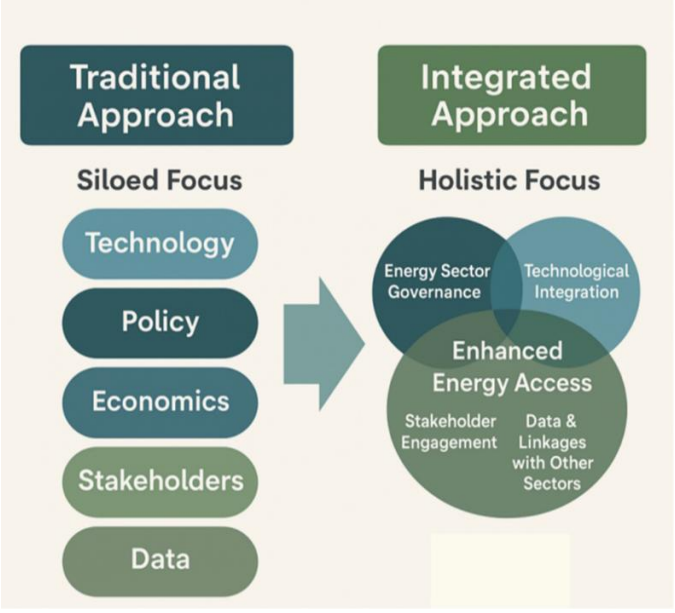

Figure 2. Overview of traditional and integrated approaches to energy access.

In this paper, we propose a preliminary framework to promote an interdisciplinary approach. Additionally, we introduce the concept of a data-driven energy platform to facilitate cross-disciplinary collaboration and foster stakeholder engagement. Such a platform can support the development of innovative, regionally tailored solutions to overcome energy access challenges. Before proceeding

3.1 Interdisciplinary Approach to Solving the Energy Access Problem

The current literature highlights the importance of interdisciplinary collaboration to address the primary challenges of energy access and develop sustainable solutions. Key disciplines identified for their contributions include [40]: Engineering; Economics and Finance; Political Science and International Relations; Environmental Science; Legal Studies; Sociology and Anthropology; Spatial Analysis; Business; Psychology; and Public Health. In our interdisciplinary approach to energy access, we focus on two guiding questions: 1. How can different disciplines be classified into collaborative domains to create a more inclusive governance model? 2. How can these domains manifest across key areas essential to solving the energy access challenge? The global energy access issue is inherently complex, influenced by a wide array of interconnected factors that shape the viability and effectiveness of potential solutions. To tackle this, we propose four primary domains: D1 (Energy Generation, Devices, and Advanced Materials), D2 (Microgrids for off-grid solutions), D3 (Internet and Communication Technology (ICT) for energy system optimization), and D4 (Environmental and Human Dimensions of energy use). This interdisciplinary framework is vital for creating comprehensive solutions that address the various aspects of energy access. Bringing together expertise from STEM fields, social sciences, and humanities is crucial for driving the sustainable development of energy systems. The literature stresses the need to integrate financial, technical, and social insights to create lasting solutions for energy access challenges [22, 41, 45-47]. Overcoming barriers such as remote monitoring, market identification, logistics, resource management, and addressing user needs requires collaboration from researchers across these disciplines [22, 41, 47]. Such interdisciplinary cooperation not only fosters idea exchange but also enhances the effectiveness of the solutions proposed. At the core of this approach is the integration of innovations in energy generation and storage (D1) with advancements in microgrid technology (D2) to improve energy system efficiency and cost-effectiveness. Additionally, incorporating AI and data science (D3) with insights into social and environmental factors influencing energy usage (D4) results in systems that are not only effective but also responsive to community needs. This approach ensures solutions that are both theoretically sound and practically feasible, particularly in remote or underserved regions.

This interdisciplinary approach manifests across several critical areas:

1. **Integration of Technical, Economic, and Social Factors:** Using data science and AI to design, create, and implement microgrids in remote, off-grid regions demonstrates the importance of aligning technical strategies with social and economic considerations. Factoring in community-specific socio-economic, behavioural, and cultural elements enhances the acceptance and sustainability of these solutions. Data-driven decision-making tools, tailored to the unique characteristics of renewable energy sources and demographic needs, provide reliable, contextually appropriate energy solutions [48].

2. **Socio-economic and Environmental Intersection:** In the contemporary business environment, creating sustainable business models that balance economic viability with sociocultural values is essential. This requires embedding environmental stewardship, equity, diversity, and inclusion into operational strategies. Interdisciplinary collaboration, drawing on insights from cultural anthropology and sociology, ensures that solutions align with local cultures and are socially responsible and sensitive to diverse community needs.

3. **Policy, Governance, and Community Engagement:** Expertise in public policy, governance, and law is critical for addressing the multifaceted challenges of energy access initiatives. Insights from these disciplines contribute to developing comprehensive strategies that account for legal and regulatory frameworks, public administration, and the social impacts of energy policies. Prioritizing community involvement and participatory methods in planning and implementation ensures that energy access solutions meet local needs and expectations. Involving local communities, stakeholders, and relevant organizations in decision-making provides a more holistic understanding of specific obstacles and opportunities for energy access. Additionally, incorporating educational, psychological, and social principles into community development strategies is essential for fostering sustainable and inclusive energy access. By considering the diverse needs and aspirations of various communities, programs can be designed to improve access to energy resources and contribute to broader societal development and well-being. Drawing on expertise from multiple fields and emphasizing community involvement and holistic development approaches enable more effective design and implementation of energy access initiatives, promoting equity and sustainability.

Addressing logistical and security challenges related to delivering energy equipment to remote areas is essential for strengthening private-sector investments in energy access across the Global South. Shifting from a focus on "capital intensity" to "data intensity" is a key strategy for overcoming financial obstacles, supporting the creation of sustainable business models, and promoting the widespread adoption of clean energy solutions. This multifaceted approach not only advances energy access in underserved communities but also contributes to poverty alleviation, socio-economic development, and environmental sustainability within the region.

3.2 Data in Energy Platform

Different stakeholders should collaborate on the energy access issue to create innovative solutions. Sharing data and knowledge between different players is one of the most critical factors in effective collaboration. Sulzer et al.[49] suggest a platform-based design for an energy system, and Fioriti et al. [48] discuss data platform guidelines and a prototype for microgrids and energy systems. Sulzer et al. [49] suggest a platform-based design (PBD) for effectively integrating renewable energy sources. In the context of energy systems, PBD (Platform-Based Design) is a methodology that streamlines the complex design of integrated systems by separating functions from architectures, identifying different levels of abstraction, and repurposing components. The semiconductor and automotive industries inspire the platform. The core of PBD is the development of modular components that can be reused and combined in various ways, ultimately aiding in faster market entry and lowering implementation risks. It improves interoperability, stimulates innovation, enhances reliability, and increases the flexibility of energy system designs. When PBD is aligned with the energy hub concept, it facilitates a holistic strategy for design and operation that spans various sectors, disciplines, and domains. The integration of these concepts leads to the creation of energy systems that are sustainable, affordable, and robust. Digital Twins and Building Information Modeling (BIM) are essential in the PBD, enabling efficient data sharing among diverse stakeholders. Digital twins integrate multiple datasets and are frequently refreshed with real-time measurement data. Moreover, PBD utilizes BIM to enhance and automate the design workflow. BIM establishes an extensive data framework that facilitates information sharing among various stakeholders and disciplines within the building sector. Fioriti et al. [48] also suggest data platform guidelines and develop a prototype for microgrids and energy access to overcome the key challenges in energy access. These challenges are listed in [48] as resource constraints, lack of granular data, high cost of traditional approaches, complex data collection, data inconsistency, stakeholder diversity, poor data quality, and uncertain demand. These challenges make it difficult to plan and deploy energy access projects in rural and underserved areas [48]. Therefore, Fioriti et al. [48] propose a platform to overcome these issues. Specifically, the platform addresses data quality issues in energy access projects through several mechanisms, including a two-fold approval process, moderator validation, reward point system, user roles and permissions, data licensing and attribution, and flexible data structure. In this work, we suggest a Data-in-Energy Platform for Energy Access projects as a preliminary idea inspired by [49] and [48]. Figure 3 illustrates a general framework of this platform. This platform should include valuable features suggested in [49] and [48]. Additionally, the Data-in-Energy Platform should consist of the features below, unlike the suggested platforms in [49] and [48]:

- **AI Integration and Disaster Response:** Unlike the platforms in [49] and [48], the Data-in-Energy Platform should leverage AI for rapid, on-demand configuration and response capabilities. For instance, its "Rapid Response Capability" could address natural disasters, providing immediate, location-specific energy system designs.

- **Global 'Energy Extension Service' and Dynamic Business Models:** The Data-in-Energy Platform should support emerging business models by providing data-rich decision-making resources, which would dynamically support entrepreneurs and small and medium-sized enterprises in the energy access sector. The inclusion of this type of data infrastructure can help lower financial and logistical barriers, specifically in under-resourced regions.
- **AI-Driven Custom Energy Solutions:** Unlike the platforms in [49] and [48], the Data-in-Energy Platform should include generative AI to develop and visualize custom energy solutions in real-time. By enabling users to input specific parameters, it can adapt the energy system design to local needs, making it a powerful tool for marginalized or remote communities.
- **Data-in-Energy Platform as a Tool for Universal Energy Access and Policy:** The Data-in-Energy Platform should aim to contribute to SDGs by shaping equitable policies and governance models, benefiting energy access at local, national, and international levels. Its AI-driven insights can help policymakers align local regulations with real-time data, strengthening its potential for influencing policy.

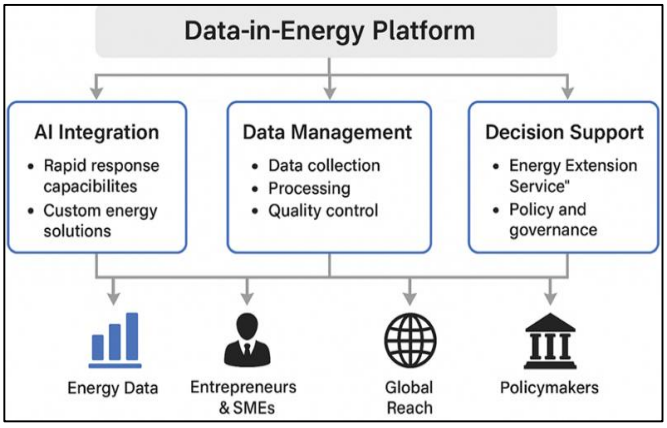

Figure 3. Simplified superstructure of the Data-in-Energy Platform.

We suggest the Data-in-Energy platform as an early idea in this paper. In future works, we aim to improve this idea in detail by collaborating with researchers from different disciplines.

4. CONCLUSION AND FUTURE WORK

As the global energy landscape is shaped by rapid geopolitical shifts and diverse challenges around priorities, the urgency of the energy access issue becomes increasingly apparent. Here we have reviewed the potential solutions to meet the challenges of for energy access highlight the positive the role of data in energy access issues. The literature shows we have different technological solutions for the energy access issue. However, the problem has multidimensional challenges. To overcome these challenges, an interdisciplinary approach is critical and our capacity to exploit and utilize data with digital technologies and AI techniques. We provide our perspective the importance and strengths of a multidisciplinary approach and propose a novel 'data-in-energy' platform.

In future work, we will focus on using data to address the energy access issue and the main features of the data-in-energy platform. Moreover, we want to improve our interdisciplinary approach to energy access issues.

Decleration

The first author used Grammarly, Grammarly AI, and ChatGPT-4o to assist with language editing. After using these tools, both authors reviewed the manuscript thoroughly and take full responsibility for its content.

Acknowledgement

The authors gratefully acknowledge Philipp Bleichinger, Daniel Kammen, Clark Miller, and Malcolm McCulloch for their valuable insights and past discussions on energy access solutions.

REFERENCES

[1] United Nations, "Goal 7: Ensure access to affordable, reliable, sustainable and modern energy for all," https://sdgs.un.org/goals/goal7.

[2] International Energy Agency, "Tracking SDG7: The Energy Progress Report, 2024," 2024. https://www.iea.org/reports/tracking-sdg7-the-energy-progress-report-2024.

[3] World Economic Forum, "How to end energy poverty and reach net-zero emissions," Jul. 2021. https://www.weforum.org/agenda/2021/07/how-to-end-energy-poverty-net-zero-emissions/.

[4] A. Gill-Wiehl, D. M. Kammen, and B. K. Haya, "Pervasive over-crediting from cookstove offset methodologies," Nat. Sustain., vol. 7, no. 2, pp. 191–202, 2024.

[5] ESMAP, "Tracking SDG 7, The Energy Progress Report," https://trackingsdg7.esmap.org/.I. Sarbu and C. Sebarchievici, "A

comprehensive review of thermal energy storage," *Sustainability*, vol. 10, no. 1, Art. no. 191, 2018, doi: 10.3390/su10010191. (proquest.com)

[6] World Economic Forum, "Ending global energy poverty—how can we do better?," Nov. 2019. https://www.weforum.org/agenda/2019/11/energy-poverty-africa-sdg7/.

[7] Government of Canada, "Sustainable Development Goal 7: Affordable and clean energy," https://www.canada.ca/en/employment-social-development/programs/agenda-2030/afforadable-clean-energy.html.

[8] S. Duran, J. Hrenyk, F. G. Sahinyazan, and E. Salmon, "Re-righting renewable energy research with Indigenous communities in Canada," J. Clean. Prod., 2024, Art. no. 141264.

[9] Canada Energy Regulator, "Market snapshot: clean energy projects in remote indigenous and northern communities," 2023. https://www.cer-rec.gc.ca/en/data-analysis/energy-markets/market-snapshots/2023/market-snapshot-clean-energy-projects-remote-indigenous-northern-communities.html.

[10] M. M. Elkadragy et al., "Off-grid and decentralized hybrid renewable electricity systems data analysis platform (OSDAP): A building block of a comprehensive techno-economic approach based on contrastive case studies in Sub-Saharan Africa and Canada," J. Energy Storage, vol. 34, p. 101965, 2021.

[11] Y. Mulugetta, E. Ben Hagan, and D. Kammen, "Energy access for sustainable development," Environ. Res. Lett., vol. 14, no. 2, p. 020201, 2019.

[12] V. Bandi, T. Sahrakorpi, J. Paatero, and R. Lahdelma, "The paradox of mini-grid business models: A conflict between business viability and customer affordability in rural India," Energy Res. Soc. Sci., vol. 89, p. 102535, 2022.

[13] Y. Mulugetta et al., "Africa needs context-relevant evidence to shape its clean energy future," Nat. Energy, vol. 7, no. 11, pp. 1015–1022, 2022.

[14] T. S. Ustun et al., "Data standardization for smart infrastructure in first-access electricity systems," Proc. IEEE, vol. 107, no. 9, pp. 1790–1802, 2019.

[15] S. Miles et al., "Internet of Things could Shape Healthcare Facility Electrification: Evidence from the Democratic Republic of the Congo," SSRN, 2024. [Online]. Available: SSRN 4983104.

[16] Y. Zhou, "Advances of machine learning in multi-energy district communities–mechanisms, applications and perspectives," Energy AI, vol. 10, p. 100187, 2022.

[17] J. Nathwani and D. M. Kammen, "Affordable energy for humanity: a global movement to support universal clean energy access," Proc. IEEE, vol. 107, no. 9, pp. 1780–1789, 2019.

[18] D. M. Kammen, V. Jacome, and N. Avila, "A clean energy vision for East Africa," 2015.

[19] J. Corfee-Morlot et al., "Achieving clean energy access in sub-Saharan Africa," OECD, Paris, France, 2019.

[20] S. Mandelli et al., "Off-grid systems for rural electrification in developing countries: Definitions, classification and a comprehensive literature review," Renew. Sustain. Energy Rev., vol. 58, pp. 1621–1646, 2016.

[21] A. Franco et al., "A review of sustainable energy access and technologies for healthcare facilities in the Global South," Sustain. Energy Technol. Assess., vol. 22, pp. 92–105, 2017.

[22] P. Alstone, D. Gershenson, and D. M. Kammen, "Decentralized energy systems for clean electricity access," Nat. Clim. Change, vol. 5, no. 4, pp. 305–314, 2015.

[23] F. Egli et al., "The cost of electrifying all households in 40 Sub-Saharan African countries by 2030," Nat. Commun., vol. 14, no. 1, p. 5066, 2023.

[24] D. Baldi et al., "Planning sustainable electricity solutions for refugee settlements in sub-Saharan Africa," Nat. Energy, vol. 7, no. 4, pp. 369–379, 2022.

[25] N. Fox, "Increasing solar entitlement and decreasing energy vulnerability in a low-income community by adopting the Prosuming Project," Nat. Energy, vol. 8, no. 1, pp. 74–83, 2023.

[26] M. M. M. Elkadragy, "A comprehensive techno-economic methodological approach for Off-grid and decentralized Hybrid Renewable Electricity Systems (OHRES): Based on contrastive case studies in Canada and Sub-Saharan Africa," Ph.D. dissertation, Karlsruher Inst. Technol., 2021.

[27] A. Gill-Wiehl et al., "Techno-economic scenario analysis of containerized solar energy for use cases at the food/water/health nexus in Rwanda," Dev. Eng., vol. 8, p. 100110, 2023.

[28] J. T. Lee and D. S. Callaway, "The cost of reliability in decentralized solar power systems in sub-Saharan Africa," Nat. Energy, vol. 3, no. 11, pp. 960–968, 2018.

[29] S. Szabó et al., "Mapping of affordability levels for photovoltaic-based electricity generation in the solar belt of sub-Saharan Africa, East Asia and South Asia," Sci. Rep., vol. 11, no. 1, p. 3226, 2021.

[30] N. Kebir et al., "Second-life battery systems for affordable energy access in Kenyan primary schools," Sci. Rep., vol. 13, no. 1, p. 1374, 2023.

[31] G. F. L'Her et al., "Potential for small and micro modular reactors to electrify developing regions," Nat. Energy, pp. 1–10, 2024.

[32] A. Gill-Wiehl, I. Ferrall, and D. M. Kammen, "Equal goods, but inequitable capabilities? A gender-differentiated study of off-grid solar energy in rural Tanzania," Energy Res. Soc. Sci., vol. 91, p. 102726, 2022.

[33] A. Gill-Wiehl and D. M. Kammen, "A pro-health cookstove strategy to advance energy, social and ecological justice," Nat. Energy, vol. 7, no. 11, pp. 999–1002, 2022.

[34] A. Gill-Wiehl, I. Ray, and D. Kammen, "Is clean cooking affordable? A review," Renew. Sustain. Energy Rev., vol. 151, p. 111537, 2021

[35] A. Gill-Wiehl, S. Sievers, and D. M. Kammen, "The value of community technology workers for LPG use: A pilot in Shirati, Tanzania," Energy Sustain. Soc., vol. 12, pp. 1–16, 2022.

[36] A. Gill-Wiehl et al., "Evaluation of the preference for and viability of clean cookstove adoption in rural Tanzania," Energy Sustain. Soc., vol. 13, no. 1, p. 42, 2023.

[37] T. Kemabonta and D. M. Kammen, "A community based approach to universal energy access," Electr. J., vol. 34, no. 3, p. 106921, 2021.

[38] A. C. Groenewoudt and H. A. Romijn, "Limits of the corporate-led market approach to off-grid energy access: A review," Environ. Innov. Soc. Transit., vol. 42, pp. 27–43, 202

[39] TramaTecnoAmbiental, "TramaTecnoAmbiental." [Online]. Available: https://www.tta.com.es/en. [Accessed: Oct. 3, 2025].

[40] B. K. Sovacool, M. Bazilian, and M. Toman, "Paradigms and poverty in global energy policy: Research needs for achieving universal energy access," *Environmental Research Letters*, vol. 11, no. 6, p. 064014, 2016.

[41] V. C. Broto, L. Stevens, E. Ackom, J. Tomei, *et al.*, "A research agenda for a people-centred approach to energy access in the urbanizing global south," *Nature Energy*, vol. 2, no. 10, pp. 776–779, 2017.

[42] M. J. Herington, E. Van de Fliert, S. Smart, C. Greig, *et al.*, "Rural energy planning remains out-of-step with contemporary paradigms of energy access and development," *Renewable and Sustainable Energy Reviews*, vol. 67, pp. 1412–1419, 2017.

[43] B. L. Robinson, M. J. Clifford, and S. Jewitt, "TIME to change: Rethinking humanitarian energy access," *Energy Research & Social Science*, vol. 86, p. 102453, 2022.

[44] B. L. Robinson, A. Halford, and E. Gaura, "From theory to practice: A review of co-design methods for humanitarian energy ecosystems," *Energy Research & Social Science*, vol. 89, p. 102545, 2022.

[45] S. C. Bhattacharyya, "Energy access programmes and sustainable development: A critical review and analysis," *Energy for Sustainable Development*, vol. 16, no. 3, pp. 260–271, 2012.

[46] K. E. Jenkins, S. Spruit, C. Milchram, J. Höffken, and B. Taebi, "Synthesizing value sensitive design, responsible research and innovation, and energy justice: A conceptual review," *Energy Research & Social Science*, vol. 69, p. 101727, 2020.

[47] S. B. Miles, J. Kersey, E. Cecchini, and D. M. Kammen, "Productive uses of electricity at the energy-health nexus: Financial, technical and social insights

from a containerized power system in Rwanda," *Development Engineering*, vol. 7, p. 100101, 2022.

[48] D. Fioriti, N. Stevanato, P. Ducange, F. Marcelloni, E. Colombo, and D. Poli, "Data platform guidelines and prototype for microgrids and energy access: Matching demand profiles and socio-economic data to foster project development," *IEEE Access*, 2023.

[49] M. Sulzer, M. Wetter, R. Mutschler, and A. Sangiovanni-Vincentelli, "Platform-based design for energy systems," *Applied Energy*, vol. 352, p. 121955, 2023.

International Journal of Energy Horizon 02 (2025) 39-60

International Journal of Energy Horizon

journal homepage: https://dergipark.org.tr/tr/pub/ijeh

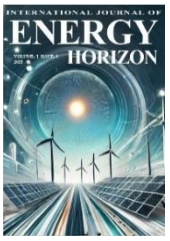

Review Article

Alkaline Water Electrolysis: A review on technological progress, market dynamics, and environmental implications

Alperen Çankaya[1,2,*], Ahmed Emin Kılıç[1,2], Yüksel Kaplan[3,4]

[1] Ankara Yıldırım University, Faculty of Engineering and Natural Science, Mechanical Engineering Department, Ankara, Türkiye
[2] Hydrogen Technologies and Energy Research Centre, Ankara Yıldırım Beyazıt University, Ankara, Türkiye
[3] Niğde Ömer Halisdemir University, Prof. Dr. T. Nejat Veziroğlu Clean Energy Res Ctr, TR-51240 Niğde, Türkiye
[4] Niğde Ömer Halisdemir University, Faculty of Engineering, Department of Mechanical Engineering, Niğde, Türkiye
[1]ORCID No: 0000-0002-4137-7862
[2]ORCID No: 0000-0002-8472-9426
[3]ORCID No: 0000-0002-0186-6063

ARTICLE INFO

Article History:

Received: 18 June 2025
Revised: 22 September 2025
Accepted:17 October 2025
Available online:30 November 2025

Keywords:

Alkaline electrolysis
Green hydrogen
Hydrogen production
Hydrogen economy
Sustainability

ABSTRACT

As global climate change continues to change rapidly, the development of sustainable and environmentally friendly energy technologies that can replace fossil fuels has become one of the top priorities in energy policy and research. Renewable energy sources such as geothermal, wind, and solar energy play a critical role in low-emission energy production; however, due to structural limitations such as intermittency and dependence on weather conditions, they cannot alone provide a continuous and reliable energy supply. In this context, hydrogen energy stands out as a strategic energy carrier that offers a solution to the intermittent nature of renewable energy sources, thanks to its high energy density, broad potential for use across different sectors, and long-term energy storage capacity. Green hydrogen, in particular, is of critical importance in terms of converting and storing excess renewable electricity production for reuse when needed. This eliminates the temporal mismatch between energy production and consumption, minimizing the carbon footprint of energy systems. Among current hydrogen production methods, alkaline water electrolysis (AWE) stands out due to its commercial maturity, relatively low investment and operating costs, stable operating performance, and ability to adapt to variable renewable energy inputs. Considering this, current developments in alkaline electrolyzer technologies are systematically examined in terms of principles, components and materials, performance optimization approaches, market dynamics, techno-economic assessments, and environmental and sustainable dimensions.

1. INTRODUCTION

Energy is one of the most basic needs not only for humans but for all living things, and global energy demand is increasing day by day. Due to its direct correlation with global warming and its impact on the environment, green energy is distinguished as an indispensable and sustainable solution to meet this demand. It is expected that global energy demand will increase by 2.2% in 2024, which is significantly higher than the average annual growth rate of 1.3% seen during the period from 2013 to 2023. Besides, total energy-related CO_2 emissions reached an all-time high of 37.8 Gt CO_2 in 2024, marking a 0.8% increase. This increase led to record-breaking atmospheric CO_2 concentrations of 422.5 ppm in 2024, which was approximately 3 ppm higher than in 2023 and 50% higher than pre-industrial levels [1]. Global warming and the resulting environmental problems are increasingly severe, and this is having a detrimental effect on the world. Fossil fuels, in all their forms, are extensively utilized due to their relatively inexpensive and readily available nature, yet this is the primary cause of these issues. While current energy demands may be met by the continued use of fossil fuels, irreversible damage is caused to all living things and the environment. Renewable energy sources such as solar [2,3], wind [3,4], hydroelectric [5], geothermal [6], biomass [7], tidal energy [8] and wave energy [9] are the first solution that comes to mind at this point, and these resources are becoming more important than ever. In contrast to fossil fuels, these energy sources engender negligible or near-zero greenhouse gas emissions, thereby contributing to the endeavour to combat climate change and air pollution. Their plentiful supply and long-term financial benefits make them a practical and lasting answer to the world's increasing energy requirements. Conversely, while renewable energy sources are sustainable, they are susceptible to erratic production due to meteorological conditions and seasonal fluctuations. Moreover, the effective management of energy resources and the establishment of infrastructure such as wind farms and solar power plants necessitate substantial land areas. Additionally, the existence of appropriate

*Corresponding author
E-mail address: alperencankaya@aybu.edu.tr
journal homepage: https://dergipark.org.tr/tr/pub/ijeh

storage solutions and grid integration is a critical requirement for these resources, as these elements can have a direct impact on the efficiency and reliability of renewable energy systems. The intermittent nature of renewable energy sources and the associated production and storage requirements are increasing the need for alternative and flexible energy carriers. Hydrogen, a high energy content and carbon-free fuel, plays a crucial role in overcoming these problems and occupies a strategic position in the future of the energy sector [10,11]. Furthermore, as an energy carrier, it can directly contribute to clean energy production with the aid of technologies based entirely on renewable energy sources. In this context, the main method used to split water into hydrogen and oxygen using renewable energy sources is water electrolysis. Various types of electrolyzers with different designs and operating principles have been developed, each offering specific advantages and limitations. This diversity enables adaptation to different application areas and energy sources in hydrogen production [12-15]. However, the four main electrolysis technologies that have attracted the most attention in the literature and industry are those that stand out for their technological maturity and performance characteristics: Alkaline water electrolysis (AWE), proton exchange membrane water electrolysis (PEMWE), solid oxide electrolysis cell (SOEC) and anion exchange membrane water electrolysis (AEMWE) [16-18]. The characterization of these technologies are presented in a comparatively in Table 1.

Table 1. The characterization of the four types of water electrolysis technologies [19,20].

	AWE	**PEMWE**	**AEMWE**	**SOEC**
Operating Temperature	70-90 °C	50-80 °C	40-60 °C	700-850 °C
Operating Pressure	1-30 bar	<70 bar	<35 bar	1 bar
Cathode Reaction	$2H_2O + 2e^- \rightarrow H_2 + 2OH^-$	$2H^+ + 2e^- \rightarrow H_2$	$2H_2O + 2e^- \rightarrow H_2 + 2OH^-$	$H_2O + 2e^- \rightarrow H_2 + O^{2-}$
Anode Reaction	$2OH^- \rightarrow H_2O + \frac{1}{2}O_2 + 2e^-$	$H_2O \rightarrow 2H^+ + \frac{1}{2}O_2 + 2e^-$	$2OH^- \rightarrow H_2O + \frac{1}{2}O_2 + 2e^-$	$O^{2-} \rightarrow \frac{1}{2}O_2 + 2e^-$
Overall Reaction	$H_2O \rightarrow H_2 + \frac{1}{2}O_2$	$H_2O \rightarrow H_2 + \frac{1}{2}O_2$	$H_2O \rightarrow H_2 + \frac{1}{2}O_2$	$H_2O \rightarrow H_2 + \frac{1}{2}O_2$
Electrolyte	Potassium hydroxide (KOH) 5-7 $molL^{-1}$	PFSA membranes	DVB polymer support with KOH or $NaHCO_3$ $1molL^{-1}$	Yttria-stabilized Zirconia (YSZ)
Separator	ZrO_2 stabilized with PPS mesh	Nafion	Fumatech	Solid electrolyte YSZ
Electrode/ Catalyst (Oxygen side)	Nickel coated perforated stainless steel	Iridium oxide	High surface area Nickel or NiFeCo alloys	Perovskite-type (LSCF, LSM)
Electrode/ Catalyst (Hydrogen side)	Nickel coated perforated stainless steel	Platinum nanoparticles on carbon black	High surface area nickel	Ni/YSZ
Porous Transport Layer Anode	Nickel mesh (not always present)	Platinum coated sintered porous titanium	Nickel foam	Coarse Nickel-mesh or foam
Porous Transport Layer Cathode	Nickel mesh	Sintered porous titanium or carbon cloth	Nickel foam or carbon Cloth	None
Bipolar plate anode	Nickel-coated stainless steel	Platinum-coated titanium	Nickel-coated stainless steel	None
Bipolar plate cathode	Nickel-coated stainless steel	Gold-coated titanium	Nickel-coated Stainless steel	Cobalt-coated stainless steel
Frames and sealing	PSU, PTFE, EPDM	PTFE, PSU, ETFE	PTFE, Silicon	Ceramic glass
H_2 purity	99.5–99.9998%	99.9–99.9999%	99.9–99.9999%	99.9%
Efficiency	50%–78%	50%–83%	57%–59%	89% (laboratory)
Development status	Mature	Commercialized	R & D	R & D
Lifetime (stack)	60 000 h	50 000–80 000 h	>30 000 h	20 000 h
Capital costs (stack) min. 1 MW	USD 270/kW	USD 400/kW	Unknown	>USD 2000/kW
Capital costs (stack) min. 10 MW	USD 500–1000/kW	USD 700–1400/kW	Unknown	Unknown

Table 2. The technical advantages and limitations of four types of water electrolysis [20].

	AWE	PEMWE	AEMWE	SOEC
Advantages	➢ Commercial usage for industry applications. ➢ Well-known technology ➢ Relatively inexpensive ➢ Long-term stability	➢ Operating in high current densities. ➢ Quick response ➢ High purity gases ➢ Compact system design	➢ Noble metal-free electrocatalysts ➢ Low concentrated (1 M KOH) liquid electrolyte	➢ High working temperature ➢ High efficiency
Challenges	➢ Limited current density ➢ High concentrated (5-7 M KOH) liquid electrolyte ➢ Crossover of the gases	➢ Expensive cost of cell component ➢ Acidic electrolyte ➢ Electrocatalysts made from noble metals	➢ Restricted stability ➢ Under development	➢ Confined stability ➢ Under development

Table 2 provides a comparison of the technical advantages and limitations of four types of water electrolysis. Notwithstanding the fact that PEMWE technology currently proffers considerable advantages such as high current density, expeditious start-up/stop capability, and rapid response to fluctuating renewable energy inputs, it has only seen significant progress in commercialization in recent years due to the high cost of materials, such as iridium/platinum-based catalysts [21]. In contrast, AEMWE technology is still in the early stages of development and is currently being researched at laboratory scale. Moreover, in view of its compatibility with non-precious metal catalysts in alkaline environments, AEMWE boasts considerable potential in comparison with PEMWE with regard to cost [22]. Nevertheless, the effectiveness and capability of this technology are contingent on the creation of state-of-the-art anion exchange membranes (AEMs) with high conductivity and stability. Current AEMs exhibit limited stability and low ionic conductivity, particularly at high temperatures, which poses a significant challenge to the technology's widespread adoption. Therefore, there is a pressing need for extensive research and development endeavours to foster heightened competition among the four electrolysis technologies and to enhance the commercial viability of AEMWE. On the other hand, SOEC technology significantly reduces energy consumption during electrolysis thanks to its high energy conversion efficiency and annihilates the requirement for noble metal catalysts. The development of this technology is being limited by two main factors. Firstly, the requirement to operate at high temperatures. Secondly, the need to maintain chemical and mechanical stability in high-humidity environments [23-24]. Among these technologies, AWE is distinguished by its comparatively low cost, long lifespan, suitability for large-scale industrial applications, high-purity hydrogen production capacity, and eco-friendliness. Indeed, AWE was the first electrolysis technology used for industrial-scale hydrogen production, which is a significant development in the field. Moreover, it has accomplished the production of green hydrogen on a megawatt scale, establishing itself as a favoured commercialization approach and a dependable solution for large-scale, cost-effective production of hydrogen of a high purity [25]. This review article aims to thoroughly analysis of the key role of (AWE) technology, which is highly developed, in producing green hydrogen. The piece's structural framework includes an analysis of AWE's essential principles, electrode reactions, components, and materials used, as well as an investigation of performance enhancement methods. Additionally, a thorough outlook on AWE is provided by exploring market trends, techno-economic evaluations, and environmental and sustainability considerations. The study gives a brief overview of the main results, explaining the current role of AWE and its possible future use in green hydrogen production.

2- FUNDAMENTALS OF ALKALINE WATER ELECTROLYZER (AWE)

The operating principle of an alkaline water electrolyzer is predicated on the separation of water into its constituent parts by means of electrical energy. This process is known as electrochemical water splitting. The process of electrochemical water splitting can be viewed as a pair of half-cell reactions: one at the cathode (the hydrogen evolution reaction, or HER) and the other at the anode (the oxygen evolution reaction, or OER). These reactions are commonly carried out in highly conductive alkaline electrolyte solutions such as potassium hydroxide (KOH) or sodium hydroxide (NaOH). The cathode undergoes a reduction reaction, producing hydrogen gas, while the anode undergoes an oxidation reaction, producing oxygen gas. The working principle of AWE is presented schematically in Figure 1.

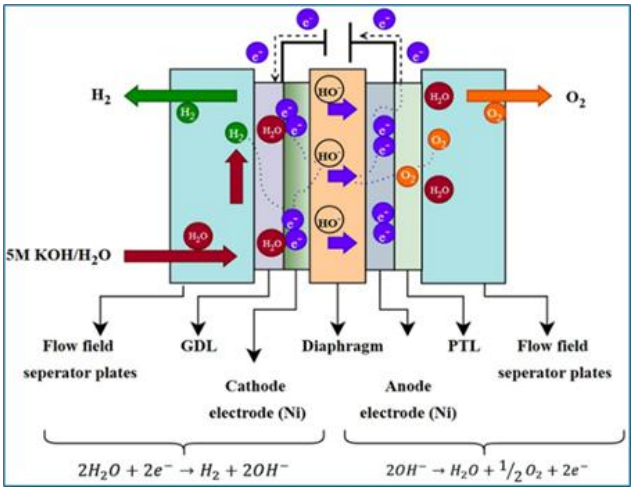

Figure 1. Schematic representation of the working principle of AWE. Adapted from Kumar, S. S., & Lim, H. (2022), [20], licensed under CC BY 4.0.

2.1. Electrochemical Reactions

2.1.1. Hydrogen Evolution Reaction (HER) Mechanism

The rate of HER in alkaline media is much slower, with a reaction rate that is roughly two to three orders of magnitude lower than in acidic media. The main reason for this sluggishness is the need for a water dissociation step at the start of the reaction, which creates an extra energy barrier [26,27].

The HER process in alkaline media follows the Volmer–Heyrovsky or Volmer–Tafel step, as demonstrated in the following equations [28-29]:

Volmer step:

$$H_2O + e^- \rightarrow OH^- + H^* \quad (1)$$

Heyrovsky step:

$$H_2O + e^- + H^* \rightarrow OH^- + H_2 \quad (2)$$

Tafel step:

$$H^* + H^* \rightarrow H_2 \quad (3)$$

The splitting of water molecules and the adsorption of hydrogen are explained by the Volmer step. The next step is to produce hydrogen using either the Heyrovsky process or the Tafel process. Figure 2 shows alkali HERs, which consist of adsorption and desorption processes.

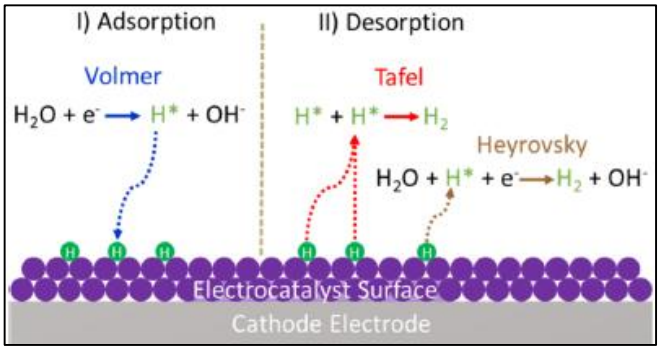

Figure 2. A representation of the alkaline hydrogen evolution reaction mechanism. Reproduced from Tüysüz, H.(2024), [30], licensed under CC BY 4.0.

2.1.2. Oxygen Evolution Reaction (OER) Mechanism

The OER is a complex and kinetically slow reaction. It involves four electron transfers. It is generally considered the main bottleneck. This limits the overall efficiency of water electrolysis. The overall OER equation in an alkaline environment is [31,32]:

$$4OH^- \rightarrow O_2 + H_2O(l) + 4e^- \quad (4)$$

The schematic of the alkaline OER mechanism on the catalyst surface is shown Figure 3. Two primary models have been proposed to explain the OER mechanism. The first is the classical adsorbed evolution mechanism (AEM). The second is the novel lattice oxygen-mediated mechanism (LOM).

2.1.2.1. Absorbed Evolution Mechanism

This is the most widely accepted process, which goes through four successive proton-electron transfer stages involving intermediates attached to active sites (*) on the catalyst surface [33,34].

$$OH^- + * \rightarrow HO^* + e^- \quad (5)$$

$$HO^* + OH^- \rightarrow O^* + H_2O + e^- \quad (6)$$

$$O^* + OH^- \rightarrow HOO^* + e^- \quad (7)$$

$$HOO^* + OH^- \rightarrow * + O_2 + H_2O + e^- \quad (8)$$

2.1.2.2. Lattice Oxygen Mechanism

This alternative mechanism, which has been suggested for certain catalysts (particularly perovskites and oxyhydroxides), involves oxygen atoms from the catalyst's crystal structure participating in the reaction. Lattice oxygen mechanism has the potential to disrupt the conventional scaling relationships of the adsorbed evolution mechanism, thereby lowering the energy barrier and consequently enhancing catalytic activity [35,36].

2.2. Historical Evolution and Industrial Maturity

The origins of water electrolysis technology date back more than 200 years. This expedition, which commenced with the observation of the electrolytic water splitting occurrence by Paets van Troostwijk and Rudolph Deiman in 1789, was established on a scientific basis with the creation of Faraday's Law in 1833. This law defined the concept of water electrolysis scientifically by establishing the quantitative relationship between the electrical energy consumed and the amount of gas produced [37]. The scaling up of this technology accelerated in the early 20th century. For instance, between 1885 and 1887, an electrolyzer was developed by d'Arsonval to produce pure oxygen for his physiological experiments. A perforated iron cylinder was used as an electrode, a cloth bag was used as a diaphragm, and a 30% KOH solution was used as the electrolyte [38].

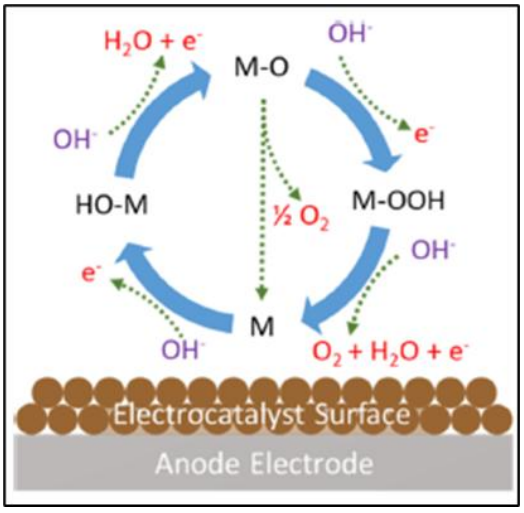

Figure 3. A representation of the alkaline oxygen evolution reaction mechanism. Reproduced from Tüysüz, H.(2024), [30], licensed under CC BY 4.0.

Significant milestones in the development of industrial hydrogen production techniques were the discovery of alkaline water electrolysis by Dmitry Lachinov in 1888 and the commercialization of asbestos as a separator (diaphragm) in 1890. In the early 1900s, nickel-based materials were recognized as excellent candidates for catalysing the oxygen and hydrogen evolution reactions (OER and HER). Modern alkaline water electrolysis (AWE) technology was established in the 1920s [39]. The growing demand for hydrogen in industrial applications, particularly in the production of ammonia fertiliser, has led to the rapid development of this technology. In 1939, the first large-scale water electrolysis factory with a capacity of 10,000 Nm³ of hydrogen per hour went into operation, and in 1948, the first pressurized industrial electrolyzers, such as the LURGI system, were manufactured [38]. AWE is the most mature and economical technology, having been used commercially for over a century. Because of its advanced technology readiness rating and minimal financial outlay, it is at the vanguard of green hydrogen manufacturing [40]. Moreover, understanding the historical development of AWE technology is important for grasping the industry's evolutionary progress. Indeed, the chronological representation of industrial progress in AWE is shown in Figure 4.

3. KEY COMPONENTS AND MATERIALS

Alkaline electrolyzers consist of basic components, including electrodes, an electrolyte and a membrane. One of the significant advantages of AWE technology is that these systems do not require precious metals or high-cost materials. The electrolyzer's reliability, efficiency and safety depend directly on the design and long-term stability of its fundamental components, as well as their material properties.

3.1. Electrodes

Electrodes are the reaction zone where water molecules undergo electrochemistry to form oxygen and hydrogen. Two electrodes are used in alkaline electrolyzers: an anode and a cathode. Each has its own specific function and importance. Electrolyzers that perform water electrolysis are similar to fuel cells in that they also consist of an anode and a cathode separated by an electrolyte [42]. The electrodes are in direct contact with the electrolyte. In alkaline electrolyzers, the electrodes are separated from the electrolyte and membrane.

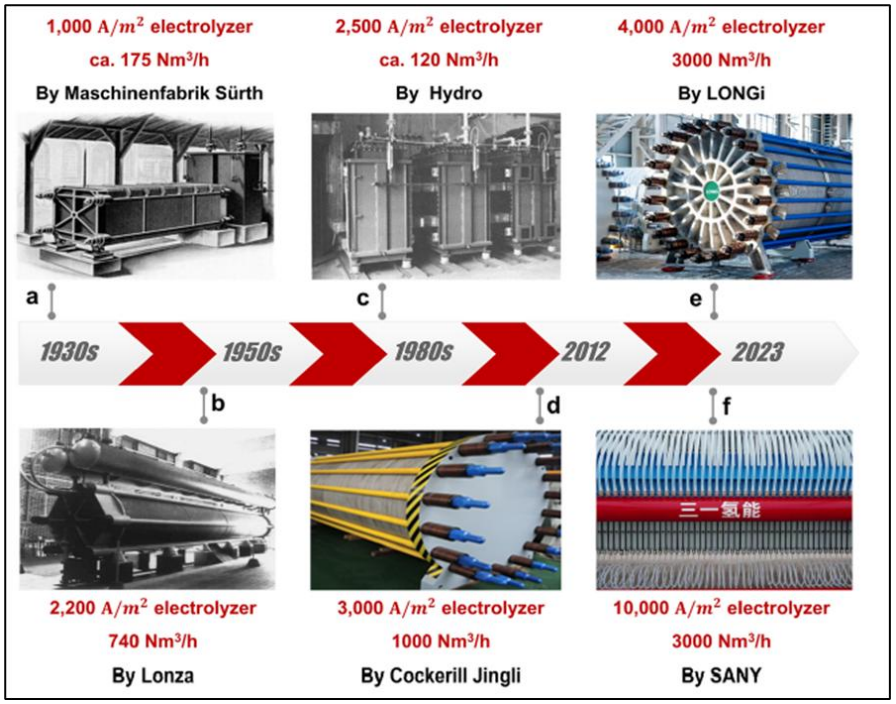

Figure 4. A diagram illustrates the progression of industrial advancements within the AWE domain. Reproduced with permission from Deng, L. et al. (2024), [41].

In other words, the electrodes that connect the electrochemical cells to an external electrical circuit carry out electron transfer. During the reaction, gas bubbles containing hydrogen and oxygen form on the cathode and anode surfaces, respectively [43]. The selection of materials is a critical factor that directly affects the efficiency of reactions occurring at electrodes. Therefore, selecting the right electrode materials is crucial for designing a high-performance alkaline electrolyzer. The two electrodes must be able to withstand corrosion in alkaline environments, have high electrical conductivity and be structurally stable. Although noble metals such as platinum (Pt) and iridium (Ir) can be used to achieve these properties, the most significant advantage of alkaline electrolyzers is that they can be manufactured using low-cost materials. That's why, high-cost noble metals are usually not used in designs. Nickel (Ni) and nickel alloys are widely used due to their high electrocatalytic activity, corrosion resistance and affordability [44]. The materials used in alkaline electrolyzer electrodes are shown in Table 3.

Table 3. The various materials used in electrodes and their properties [45]

Electrode Material	Catalytic Activity	Corrosion Resistance	Electrical Conductivity	Stability	Typical Compositions/Examples	References
Nickel-based	High	Good	Moderate	Good	Ni, Ni-Fe, Ni-Mo, Ni-Mo-Cd, Ni-Zn, Ni-Al, Ni-Sn, Ni-Co, Ni-Cr, Ni-Cu, Ni-P, Ni-W, Ni-Mn	[44,46,47]
Oxide-Based	Moderate to High	Excellent	High	Excellent	NiO, Co3O4, FeOOH, NiFe2O4, LaNiO3, La0.6Sr0.4CoO3, Ba0.5Sr0.5Co0.8Fe0.2O3-δ	[48,49]
Platinum-group	Excellent	Excellent	High	Excellent	Pt, Pt-Ir, Pt-Ru,Pt-Ni, Pt-Co, Pt-Dy, Pt–Ce, Pt–Sm, Pt–Ho	[50,51]
Transition Metal Oxides	Moderate	Good	Moderate to High	Good	RuO2, IrO2, TiO2, WO3, MnOx, FeOx	[52,53]
Perovskite Oxides	High	Good	High	Good	LaNiO3, La0.6Sr0.4CoO3, Ba0.5Sr0.5Co0.8Fe0.2O3-δ,SrNb0.1Co0.7Fe0.2O3-δ	[54,55]
Nanostructured Materials	High	Good to Excellent	High	Excellent	Ni nanoparticles, NiO nanotubes, Co3O4 nanowires, Pt-Ni nanowires	[56-60]

3.2. Electrolyte

The type and concentration of the electrolyte, as well as the temperature conditions, determine ion conductivity. This directly impacts intracellular resistance and overall efficiency. A stable ion environment and high conductivity reduce energy consumption while increasing the rate of hydrogen production. The main role of the electrolyte in alkaline electrolyzers is to facilitate the movement of ions between the electrodes, thereby supporting the electrochemical process. The electrolyte's role is to carry the required hydroxide (OH^-) ions to the electrodes during the process of water decomposition, thereby enabling the reactions to take place. Therefore, the electrolyte solution must be selected carefully to ensure the performance and efficiency of alkaline water electrolysis systems is optimized. The most common electrolytes used in alkaline electrolyzers today are solutions of potassium hydroxide (KOH) and sodium hydroxide (NaOH) [44]. The most common types of electrolyte are these two because they supply high levels of hydroxide ions and minimize ohmic losses. When comparing these two substances, producers of alkaline electrolyzers generally prefer potassium hydroxide to sodium hydroxide because of its superior electrolyte conductivity at temperatures between 50°C and 80°C. The most frequently cited electrolyte type is potassium hydroxide's aqueous solution, with a concentration of 25% to 30% by weight [61,62]. The efficiency of an electrolyzer is significantly affected by electrolyte concentration. Elevating the electrolyte concentration of potassium hydroxide and sodium hydroxide concomitantly augments the hydroxide ions within the electrolyte. An increase in hydroxide ions precipitates a marked acceleration in the rate of water decomposition. This, in turn, leads to an increase in the rate of hydrogen production. Although this may appear to be an effective way to increase electrolyzer efficiency, it is not. It is crucial to determine the appropriate electrolyte concentration because high concentrations can have negative side effects on the system. For instance, an elevated electrolyte concentration has the capacity to impede ion and electron flow, diminish cell voltage efficiency, and curtail the aggregate energy efficiency of the electrolysis process, thereby diminishing the overall system efficiency [63]. Therefore, selecting the correct electrolyte concentration is key to optimize the performance of an alkaline electrolyzer, in terms of both ion transport and temperature control, as well as maintaining appropriate pH conditions. Research is ongoing into developing electrolyte solutions that can improve the performance of alkaline electrolyzer systems [44,64]. In particular, research on lithium hydroxide (LiOH) and barium hydroxide ($Ba(OH)_2$) has shown promising results. These alternative electrolytes have the potential to offer advantages such as higher ionic conductivity and reduced electrode degradation in certain applications [44]. Furthermore, alkaline electrolyzers can use different types of electrolytes. A comparison of these electrolyte types and their basic properties is provided in Table 4.

Table 4. Properties of the most commonly used electrolytes

Electrolyte Solution	Concentration [44]	Conductivity [62]	Corrosiveness [65]	Safety [44]	Carbonation Sensitivity [62,66]
Potassium Hydroxide (KOH) Concentrated (45%)	High	High	High	Low	High
Diluted Potassium Hydroxide (KOH) Concentration (20-30%)	Moderate	Moderate	Moderate	Moderate	High
Sodium Hydroxide (NaOH)	High	High	High	Low	High
Potassium Carbonate (K_2CO_3)	High	High	Moderate	Moderate	Low
Lithium hydroxide (LiOH)	High	High	High	Moderate	Moderate
Barium hydroxide (Ba(OH_2))	High	High	High	Low	Moderate
Alkaline Polymer	Variable	Variable	Low	High	Low
Solid-State	Variable	Variable	Low	High	-
Electrolyte Trisodium phosphate (Na_3PO_4)	High	High	Moderate	Moderate	Low
Sodium bicarbonate ($NaHCO_3$)	High	Moderate	Low	High	Low
Sodium metaborate ($NaBO_2$)	High	Moderate	Moderate	Moderate	Low
Sodium hydrogen phosphate (Na_2HPO_4)	High	High	Moderate	Moderate	Low

3.3. Membrane

The main objective of the membrane in an alkaline electrolyser is to separate the produced hydrogen and oxygen gases. While the membrane separates these gases, it must allow hydroxide ions to pass through. Therefore, it can be said that the membrane is the most complex element of the alkaline electrolyzer. Additionally, the membrane operates in a highly alkaline environment with a pH of around 14, so it must be corrosion-resistant in the long term. In general, membranes can be split into two types: microporous membranes and exchange membranes [67]. Both membranes have the same principal purpose which is being ion-permeable while setting apart produced hydrogen and oxygen gases. Microporous membranes are lightweight, permeable materials with pores that are usually between 0.1 and 10 µm in size. Size exclusion and other filtration techniques are used in the design of these membranes to selectively permit the passage of some molecules, ions, or particles while obstructing others. On the other hand, Ion-selective membranes called exchange membranes are made to allow the passage of some ions while obstructing the passage of others. The kind of ion that these membranes transport determines their classification. If an exchange membrane allows positively charged ions transportation, then it is called cation exchange membranes. Moreover, a membrane that allows negative ion exchange, is named anion exchange membranes. A suitable membrane has to perform high quality of gas separation at working current densities. Also, it must show low ionic resistance for not to decrease the efficiency of the system. In the early stages of the development of alkaline electrolyzers, asbestos was widely used as the primary material for diaphragms and membranes. Nevertheless, owing to the significant health hazards it presented during setup and upkeep, its usage was progressively discontinued and substituted by more secure and long-lasting membrane techniques. Zirconium oxide-filled polyolefin-based diaphragms, such as Zirfon®, are the most common materials developed today to replace asbestos [68,69]. Thanks to its high mechanical strength, chemical stability and low gas permeability, Zirfon has become the standard in commercial alkaline electrolyzers. Polyolefin-based polymers, composite ceramic-polymer membranes, and alkaline-stable polymer membranes are also prominent material groups in AWE applications. Membrane/diaphragm materials are generally divided into four basic categories: Ion-conductive polymer membranes (e.g., perfluorosulfonic acid-based membranes), Alkali-stable polymer membranes (e.g., aryl ether ketone or polyethylene-based membranes), Composite membranes (e.g., polymer/ceramic hybrid structures), Gel electrolyte membranes. The safety of gas separation, ion conductivity and long-term stability of alkaline electrolyzers has been significantly improved by these developments [70]. Figure 5 shows a schematic representation of the historical development of membrane types.

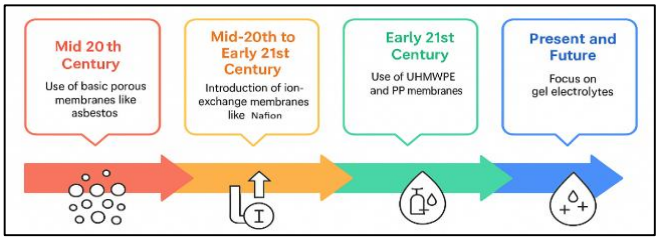

Figure 5. Evolution of Electrolyzer Membranes: From asbestos to gel electrolytes

3.4. Cell Design

Containment part of the alkaline electrolyzers is called cell frame or housing. It provides the system with structural integrity and support, ensuring that the electrolyzer operates unaffected by environmental conditions. The prevention of electrolyte and produced gas leakage is also the responsibility of the cell frame. When assembled in stacks, the cell frame functions as a connecting element, thereby uniting individual cells. It connects the cells in series electrically. Consequently, the production of hydrogen increases when individual cells are connected. The specified requirements are typically met by selecting nickel-plated steel or other corrosion-resistant materials for the cell frame [45].

3.4.1. Cell Design Configurations

The quality of alkaline electrolyzers is affected by the design and configuration of the cells. The aim of cell design is to optimize system performance by arranging its key components as specified. These key components have been configured to provide ionic conductivity and the separation of production gases, as well as reducing energy losses during electrochemical reactions. Cells are assembled into stacks, with connections between them either in series or in parallel. There are three main types of cell design, as described in the literature: monopolar, bipolar and zero-gap [71,72].

3.4.1.1. Monopolar Design

The monopolar cell design is notable for its adaptability and simplicity, allowing cells to be easily added or removed. In this set-up, the cells are arranged side by side, with each cell having its own electrode and electrolyte housing. Furthermore, as each electrode is connected directly to an external power source, it is possible to connect all cells in parallel. All monopolar cells have the same voltage applied to each electrode pair [45,71]. The monopolar design offers a modular structure and ease of maintenance. This design's primary configuration is characterised by the following advantages. In contrast, the disadvantages of the monopolar designinclude insufficient energy efficiency, high electrical resistance and limited current density. Consequently, most commercial alkaline electrolyzer manufacturers prefer a bipolar design for their cells [37]. Figure 6 shows a schematic representation of the monopolar design.

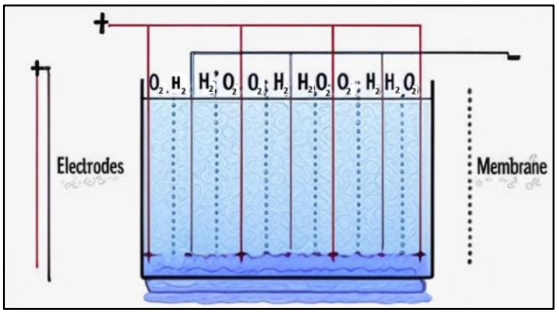

Figure 6. Monopolar Cell Design. Adapted from Scott, K. (2019), [67].

3.4.1.2. Bipolar Design

In a bipolar cell design, the cells are connected in series. This is achieved by connecting only the side electrodes to the direct current (DC) power source. This means that each cell shares an electrode with its neighbouring cell [45]. The result of this is that the flowing current polarises each electrode. Oxidation reactions take place at one of them, while reduction reactions take place at the other electrode [67]. The bipolar cell design is notable for its significant advantages, including its compact structure, reduced ohmic losses and more homogeneous current distribution. The system can be designed more compactly by applying the electric current only to the end (side) electrodes in this configuration. Therefore, a greater number of cells can be accommodated within the same volume compared to the monopolar design. Connecting the cells directly reduces the distance between the electrodes, thereby decreasing ohmic losses and ensuring the electrical current is used efficiently. Furthermore, many commercially produced electrolyzers use a bipolar design, which increases current densities while reducing cell voltage [67]. However, the bipolar cell design also has some disadvantages, which include the fact that it is less efficient and more costly than other designs. It has a more complex structure than the monopolar configuration. This requires more sophisticated production and installation processes, which increases costs. Furthermore, as all cells are connected in series, identifying a faulty cell when a malfunction occurs is difficult. This results in higher maintenance costs and the necessity for specialized knowledge in maintenance procedures [71]. Figure 7 shows a schematic representation of the bipolar design.

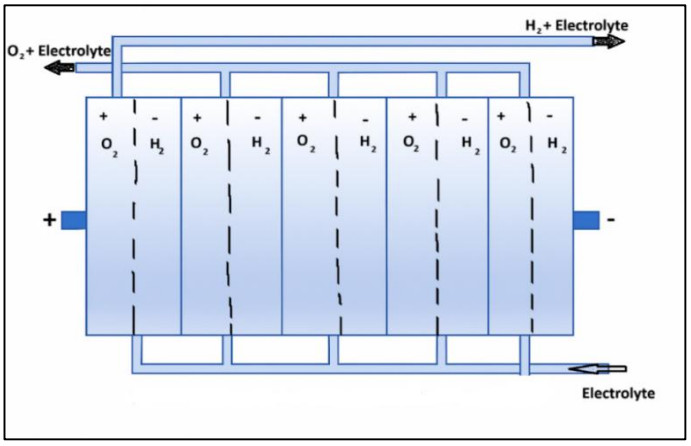

Figure 7. Bipolar Cell Design. Adapted from Scott, K. (2019), [67].

3.4.1.3. Zero-Gap Design

The main aim of zero-gap design is to reduce the space between electrodes, even bringing the electrodes into direct contact with the membrane to get rid of ohmic losses and thus boost current density as much as possible. Selecting this design improves mass transport within the cell, reduces ohmic losses and achieves higher current densities. Furthermore, preventing damage caused by gas bubbles makes cell performance more stable [72,73]. However, achieving long-term suitability for a zero-gap design requires the use of specialised electrode and separator materials. Furthermore, electrolyte management poses a significant challenge in this configuration [45]. In summary, although it offers improved performance, the zero-gap design is considered to be a more complex, costly and highly specialised approach. The zero-gap design is shown schematically in Figure 8. A comparison of the monopolar, bipolar and zero-gap cell designs of alkaline electrolyzers is given in Table 5.

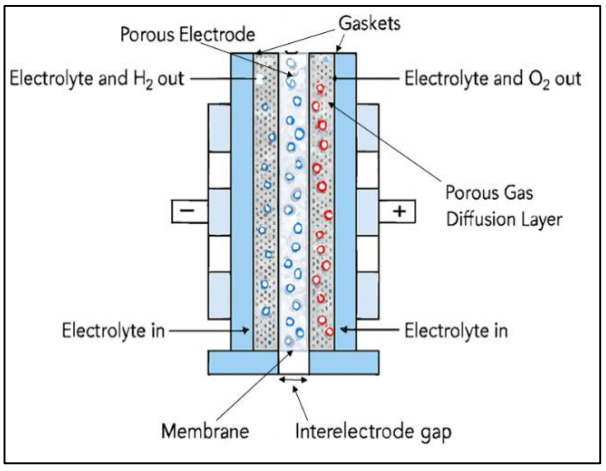

Figure 8. Zero-gap Cell Design. Adapted from Scott, K. (2019), [67].

Table 5. A comparison of monopolar, bipolar and zero-gap cell designs in alkaline electrolyzer.

	Monopolar [45,71]	Bipolar [45,71]	Zero-gap [72,73]
Advantages	➢ Simple and adaptable design ➢ Easy addition and removal of cells ➢ Low production cost	➢ Compact Design ➢ Lower ohmic losses ➢ Better current distribution ➢ Common in commercial application	➢ Minimum distance between electrodes ➢ Reduction in ohmic losses ➢ Higher current density ➢ Improvement in mass transfer ➢ Reduction in gas bubble effects
Challenges	➢ Requires a larger volume ➢ High ohmic losses ➢ Lower current density	➢ More complex production and installation ➢ Higher cost ➢ Difficulty in detecting faults. ➢ High maintenance cost	➢ Requires specialized membrane/electrode materials ➢ Electrolyte management is challenging ➢ More complex and costly design

4. PERFORMANCE OPTIMIZATION STRATEGIES

Many factors influence the performance of alkaline electrolyzers. These include the operational system conditions, gas bubble dynamics, gas crossover, porosity, computer-aided design (CAD) studies, and system integration. These factors have a direct impact on intracellular processes, playing a decisive role in energy efficiency, gas purity and long-term stability. Consequently, a methodical evaluation of these factors is paramount for enhancing performance and conducting a thorough analysis.

4.1. Operating Conditions

The three key operating factors to consider when using an alkaline electrolyzer are temperature, pressure and current. The value of these parameters is directly affected by the current density and the properties of the electrode surface. Controlling these parameters properly improves system performance and increases energy efficiency. Moreover, ensuring optimal operating conditions significantly reduces production costs and enhances system safety. Temperature effect: via raising the working temperature enhances the conductivity of electrolytes and electrode reaction rates and decreases cell voltage. In a zero-gap cell of 0.1 mm thick diaphragm, about 1.8 A/cm^2 nominal current density at about 100 °C was observed [74]. According to Ren et al. [75], it is possible to achieve high current densities while maintaining a low cell voltage of 80°C. Their research demonstrated that high current densities can be achieved with low voltage values, particularly at this temperature. According to Abdin et al. [76]: The best range of temperature was between or raises reaction rates and reduces the problem of handling heat.

Pressure effect: This effect is useful for minimizing power usage, since direct compression of hydrogen can be achieved. Solovey et al. [77] observed efficiency improvements of up to 15% in membrane-less cells operated at 60–70 MPa. Similarly, Valderrama [78] emphasized the economic benefits of high-pressure systems. However, the probability of gas crossover and mechanical strain increases with high pressure. Simulations indicate that the optimal pressure for achieving Faraday efficiency and gas purity is around 5 bar, but pressures of around 8 bar can make operation at low loads difficult [74]. Successful outcomes also report a cell voltage of 2.29 V at 1.67 A/cm² [79]. Intermediate levels of current density offer the best balance between monetary efficiency and production volume. The surface characteristics of the electrode are as follows: Roughness and porosity of electrodes maximizes the electrochemically active area, thereby increasing the rate of reaction. However, Abdin et al. have shown that high roughness can reduce efficiency due to increased gas adsorption, and that moderate roughness provides the best performance [76]. Performance can also be enhanced by techniques such as moulding with ice, which eliminates ohmic resistance in nickel-based electrodes [80]. Lithographically generated microstructures that allow bubbles to be separated twice as fast offer twice the efficiency.

In conclusion, the optimization of temperature, pressure, current density and electrode surface morphology together contributes significantly to both increasing the energy efficiency and hydrogen production potential in alkaline electrolyzers. Table 6 illustrates the impact of different parameters on performance.

Table 6. The performance effects on the parameters.

Parameter	Range	Performance Effect	References
Temperature	25–100 °C	Low cell voltage at high temperatures, high conductivity, high efficiency	[75,76]
Pressure	1–70 MPa	Up to 15% increase in efficiency, direct hydrogen compression; increased crossover at high pressure	[74, 77, 78, 81]
Surface roughness	Low-Medium	Medium roughness is optimal; excessive roughness increases gas retention; special microstructures accelerate bubble separation	[76,80]

4.2. Bubble Dynamics

The bubbling of hydrogen and oxygen produced during the electrolysis process in alkaline electrolyzers has a significant impact on its efficiency. Due to the accumulation of bubbles on the electrode surface, the liquid layer transferred

towards the electrolyte thickens, decreasing ion conductivity and exerting a screening effect on the liquid layer [82]. Additionally, the presence of freely circulating bubbles in the liquid phase expands ion transport and causes a 'void effect' that increases the internal resistance of the cell [82]. Bubble formation occurs via three primary mechanisms: nucleation and growth; reaching a critical size; and detachment from the surface. Before reaching a critical size, bubbles accumulate on the surface and cover the active sites of the electrodes, reducing the surface area available for reaction. This effect becomes more pronounced with increasing current densities, ultimately leading to increased energy consumption [66,83]. Some studies have shown that pressure changes facilitate the removal of bubbles from the surface, thereby reducing ohmic losses [84]. Haverkort and Rajaei found that maintaining a gap of just 0.2 mm between the electrode and diaphragm significantly reduces bubble-induced ohmic losses [73]. However, although zero-gap designs are highly energy efficient, they are difficult to implement in practice due to their complexity and the materials required [85]. Figure 9 shows the schematic diagram illustrating the distribution of bubble formation locations on the electrode surface.

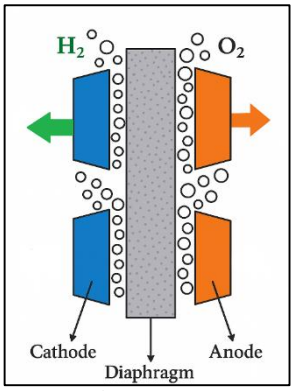

Figure 9. Spatial Distribution of Bubble Generation Sites on the Electrode Surface. Adapted from Ding, S. et al. (2022), [86].

There are various strategies for improving bubble separation. The first involves applying external influences. For example, external stimuli such as magnetic fields (Lorentz force) or ultrasonic vibrations can be employed to increase the separation of bubbles from the surface. These methods enhance reaction efficiency by maintaining an active electrode interface. Indeed, experimental studies have shown that applying ultrasound results in a 10–25% reduction in cell voltage and a significant increase in Faraday efficiency [87]. Another method is surface modification. Superhydrophobic or superaerophobic coatings applied to electrode surfaces can inhibit bubble coalescence, enabling the formation of smaller bubbles that dissociate more quickly. To illustrate, nickel electrode surfaces boasting circular microarray structures have been documented as offering elevated bubble dissociation rates in comparison to flat surfaces, effecting an approximate doubling of the reaction rate [82]. Therefore, the dynamics of bubble formation must be considered alongside electrode surface design and operating conditions. The impact of different parameters on performance is illustrated by Table 7.

4.3. Gas Crossover

Some of the hydrogen produced in alkaline electrolyzer cells can pass through the diaphragm or membrane to the counter electrode. This reduces cell efficiency and decreases gas purity, as well as posing a safety risk. Excessive gas concentration in the liquid phase is one of the main causes of increased crossover tendency [88]. The influence of operating parameters is crucial for hydrogen permeation. Trinke et al. measured the hydrogen permeation level to be 3–5 mA/cm² at a current density of 1 A/cm², and found that the permeation rate increased dramatically with temperature [89]. Furthermore, while 20–60 times supersaturation can be seen in zero gap cells at the diaphragm–electrode interface, this value drops to 2–4 times with the addition of a 0.5 mm gap between the electrodes [90]. It is suggested that adding a gap, particularly on the cathode side, can greatly reduce hydrogen permeation.

The role of membrane materials in limiting hydrogen permeation and improving electrolyzer performance is critical. The development of membranes that can simultaneously prevent gas permeation and provide high ionic conductivity has been achieved for this purpose. The Zirfon® (ZrO_2/polysulfone)-based structure is the most widely used membrane in industry today. However, further performance enhancement is possible with new-generation composite membranes. To illustrate, a 0.35 mm-thick PVA-coated Zirfon membrane reduced surface resistance to less than 0.17 Ω cm² and almost completely eliminated liquid flow thanks to its porous PVA coating [91]. Another innovative approach is the PPS/YSZ composite membrane. This membrane provides superior performance, delivering a high bubble pressure of 2.93 bar, minimum surface resistance of just 0.21 Ω cm² and 99.9% hydrogen purity [92]. Wettability and porosity are critical parameters that directly impact the performance of the diaphragm. When the wettability of the diaphragm surface drops below 30%, the membrane resistance increases and the current density decreases accordingly. This can have a negative impact on the overall efficiency of the electrolyzer [86]. On the other hand, when the diaphragm's porosity exceeds 30%, the separation of gas is possible more rapidly. However, excessively high porosity can lead to unwanted gas leakage. Therefore, achieving the optimum porosity level is critical for balancing performance, as it maintains ionic conductivity while limiting gas permeation. Table 8 presents the gas crossover rates observed in different membrane/diaphragm materials at 80 °C with a 30% KOH electrolyte.

Table 7. The performance impact on the parameters.

Parameter	Range/Property	Effect	Ref.
Electrode–diaphragm distance	0–0,2 mm	Ohmic losses decrease at small distances	[73,85]
Bubble size	Small – Medium	Small size results in rapid separation and low surface coverage	[66]
Surface modification	Superhydrophobic/ micro-patterned Ni	Prevents bubble coalescence and increases separation rate	[82]
External stimulus	Ultrasonic, magnetic field	Ohmic losses decrease by 10–25%, increasing efficiency	[84]

Table 8. The gas crossover rates observed in different membrane/diaphragm materials

Die Type / Material	Current Density (mA/cm²)	Voltage (V)	Resistance (Ω·cm²)	H_2 Gas Crossover (mol·cm^{-1}·s^{-1}·bar^{-1})	References
Zirfon PERL (ZrO_2/polysulfone)	771–1765	2,0–2,6	0,27	$1{,}85 \times 10^{-11}$	[93]
Thin Zirfon with PVA coating	861–1890	2,0–2,6	0,267	$1{,}12 \times 10^{-11}$	[91,94]
PPS/YSZ composite	—	—	0,21	—	[92]
ZTA (ZrO_2 toughened Al_2O_3)	2000	2,1	0,15	$10{,}7 \times 10^{-12}$	[95]

4.4. Porosity

Porosity is a fundamental structural parameter that plays a decisive role in the ion conductivity, gas separation, and mass transfer of both electrodes and diaphragms. Pore size, distribution, and total porosity ratio directly affect both cell impedance and gas leakage. It is possible to examine the porosity phenomenon under two basic headings, namely electrode porosity and diaphragm porosity. Electrode porosity: Porous electrodes (e.g. nickel foam with a porosity of over 90%) increase the reaction area by expanding the active surface area. This reduces overpotentials and increases current density. In industrial applications, braided or mesh-structured nickel electrodes are generally preferred. However, very high porosity levels can cause gas bubbles to become trapped in the pores and block them. To overcome this problem, channeled or asymmetric pore structures have been developed. Kim and colleagues, for instance, came up with a design that involved using pores measuring 5 μm on one electrode surface and 100 μm on the other. This structure enables gases to exit through the small pores and separate rapidly from the large pores, achieving outstanding performance at a current density of approximately 0.5 A/cm² [82]. Diaphragm porosity: Diaphragms must have a controlled pore structure that permits the free movement of ions while preventing gas permeation. Standard Zirfon UTP 500 diaphragms are composed of a porous material reinforced with inorganic fillers and reinforced with polyethylene fabric [91]. The porosity of such diaphragms is generally below 30%, which limits ion conductivity and increases intracellular resistance. As an alternative option, greater levels of porosity can encourage the movement of ions while simultaneously boosting gas permeation. Ding and colleagues have indeed observed that high porosity can enhance reaction efficiency by facilitating the rapid decomposition of certain gases. However, this increase in efficiency can also result in an elevated risk of gas crossover [86]. Table 9 shows the effect of porosity on the component.

Table 9. Effect of porosity on the components

Component	Porosity (%) / Structural Feature	Effect	References
Ni foam	>90	High active surface, low overpotential, high current	[82]
AsymmetricNi	5–100 μm pores	Rapid gas separation, high performance	[95]
Zirfon UTP 500	Medium	High ion conductivity, limited gas passage	[91]
PVA-coated membrane	Medium + coating	Low gas passage, low resistance	[94]
Low porosity membrane	<30	High resistance, low efficiency	[94]

4.5. CAD Studies

In recent years, CAD-based numerical modelling and CFD simulations have become an important area of research in the optimization of the performance of alkaline electrolyzers, complementing experimental studies. Rodríguez and Amores [96] used COMSOL software to compare their two-dimensional (2D) CFD model with experimental data and validate polarization curves with an error of less than 1% under different operating parameters (temperature, electrolyte conductivity and electrode–diaphragm distance). This study enabled more accurate modelling of current density distribution, gas-liquid profiles and ohmic losses by examining the effects of both electrochemical and fluid dynamics simultaneously. On the other hand, Xue et al. [97] used a three-dimensional (3D) Euler-Euler approach to model two-phase flows with CFD, studying various channel geometries (single, double and triple inlet) and spherical protrusions. Electrolytic structures exhibiting a variety of geometric models are demonstrated in Figure 10.

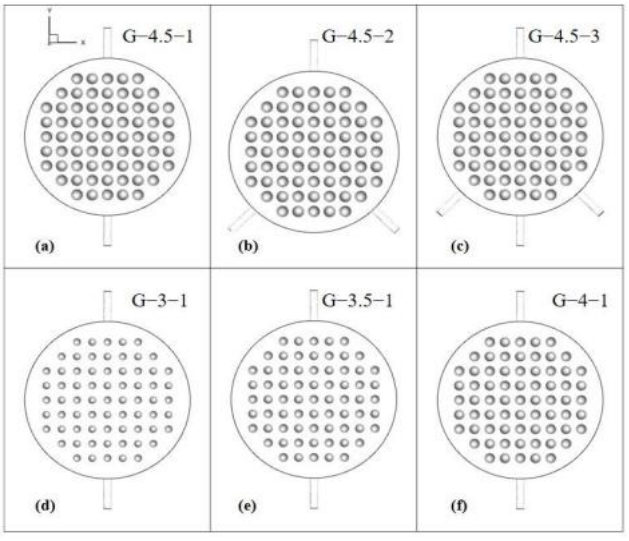

Figure 10. Electrolytic chambers with various geometric design. Reproduced from Zue, L. et al. (2024), [97], licensed under CC BY 4.0.

The model defined the area of the porous media membrane, implemented user-defined functions (UDFs) based on Faraday's law for the gas generation source terms and used an optimized mesh structure with refined regions. The findings indicate that the three-inlet model reduces the outlet hydrogen concentration by around 22% compared to the benchmark model while significantly improving flow and temperature distribution. It was also demonstrated that increasing the radius of the spherical protrusions improves flow uniformity and reduces gas accumulation. Figure 11 shows the electrolyte velocity distribution, electrolyte temperature distribution and H_2 gas volume fraction distribution in electrolytic cells with different input numbers.

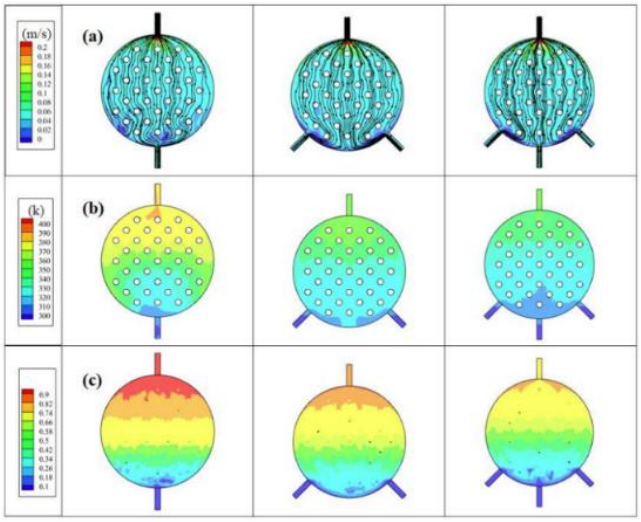

Figure 11. In electrolytic cells with various inlet quantities: (a) the distribution of electrolyte velocity, (b) the distribution of electrolyte temperature, and (c) the distribution of H_2 gas volume fraction. Reproduced from Zue, L. et al. (2024), [97], licensed under CC BY 4.0.

CFD-based simulations directly impact flow channel design, gas-liquid separation and energy efficiency. Therefore, CFD has the potential to be a highly effective design tool for future industrial-scale electrolyzer applications.

4.6. System Integration

Alkaline electrolyzers contribute to grid balancing, particularly when used alongside renewable energy sources. Integrating them into a traditional energy system increases energy usage efficiency and reduces grid load by converting excess electrical energy into hydrogen production [98]. In this context, the integration of an electrolyzer requires a combined evaluation of multi-component systems, such as power electronics, thermal management and control strategies. For instance, Zhao et al. modelled a 500 kW alkaline electrolyzer system by analysing the medium voltage converter topology and control algorithms. The study tested the system's resilience in the face of voltage fluctuations, demonstrating that the DC link voltage could be maintained at 95% [99]. The performance of electrolyzer systems depends critically on power electronics and grid connection. These systems are usually connected to the grid via a direct current (DC) link and a power converter. The quality of power is subject to direct influence from parameters such as grid impedance (short-circuit ratio) and switching frequency [100]. The model developed by Zhao and colleagues suggests that the short-circuit ratio is a key factor in determining total harmonic distortion. Additionally, it has been reported that the designed control system can maintain 95% of the DC link voltage even with a 20% voltage drop [99]. Thermal Management and Balance of Plant (BoP): Efficient thermal management involves maintaining the electrolyzer stack at a constant temperature and removing the generated waste heat effectively. However, in dynamic operating modes, heat transfer delays can lead to fluctuations in stack temperature, which can have a negative impact on the efficiency of the system as a whole. Jiang et al. [98] developed a model based on the equivalent circuit approach, demonstrating that heat transfer delays can cause the stack temperature to temporarily overheat by up to 10°C, thereby shortening the system's lifespan. Dynamic control strategies: In order to adapt to the fluctuating nature of renewable energy sources, the current and voltage of the electrolyzer must be adjusted quickly. In this context, the performance and service life of cells are directly affected by dynamic operating modes (e.g. load-following or current ramp control). Jiang et al. [98] investigated how the system responds to random changes in the current. They showed that transient thermal extremes arising during this process can significantly shorten the stack's life. Figure 12 shows that provides a general overview of a system for the industrial-scale production of green H_2 in AWE.

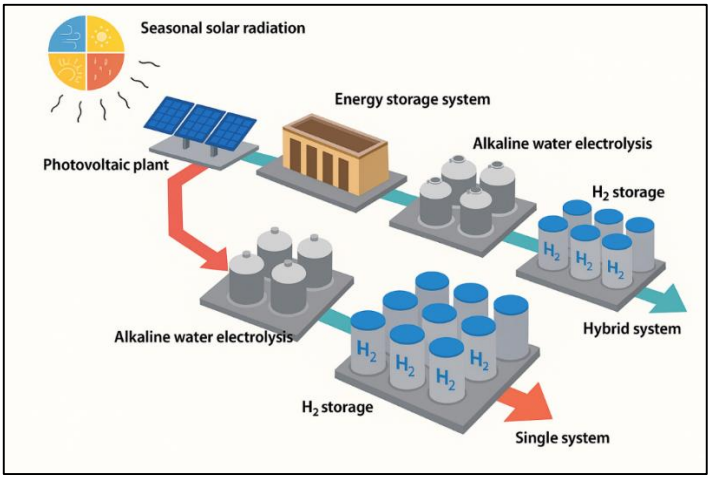

Figure 12. General overview of a system for the industrial-scale production of green hydrogen. Adapted from Lee, H. et al. (2022), [101].

5. MARKET OUTLOOK AND TECHNO-ECONOMICS

Global energy transition pathways increasingly position hydrogen as a cross-sector decarbonization vector, enabling energy storage, industrial feedstock substitution, and deep-abatement in hard-to-electrify segments. The International Energy Agency projects that demand for low-emission hydrogen could approximately triple by 2030 in its net-zero aligned framing, while remaining below total potential demand without stronger policies [102]. Complementing this, system-wide scenarios indicate clean hydrogen demand could expand to roughly 125–585 $Mt \cdot y^{-1}$ by 2050 depending on transition pace and technology learning [103]. Against this backdrop, alkaline water electrolyzers (AWEs)—owing to their cost advantage, commercial maturity, durability, and use of abundant non-noble catalysts—are strategically positioned for large-scale, renewable-integrated hydrogen supply. In line with current EU regulations, “renewable hydrogen” is defined as RFNBO-compliant under the 2023 Delegated Acts, which impose additionality and temporal/geographic correlation requirements, while “low-carbon hydrogen” is classified as meeting a life-cycle GHG intensity ≤ 3.38 kg CO_2e/kg H_2 (≈ 70 % below the fossil comparator) under the EU Gas Decarbonisation Package [104,105]. Table 10 summaries recent quantitative hydrogen deployment targets across the EU, Türkiye and selected MENA states. These policy ambitions—ranging from the EU’s 40 GW electrolyzer goal by 2030 to Türkiye’s 2–5 GW roadmap and multi-megaton hydrogen export plans in Oman and the UAE—provide direct signals to investors and technology developers [106-111]. These targets and definitions are not just high-level aspirations; they actively shape deployment priorities, steering capital toward AWE configurations that combine techno-economic feasibility with sectoral fit in the near to medium term.

Table 10. National and regional hydrogen deployment targets (EU, Türkiye, MENA)

Region / Country	Electrolyzer / H_2 Target	Hydrogen Type	Timeline	References
European Union	6 GW by 2024; 40 GW by 2030; 10 Mt domestic + 10 Mt imports by 2030	Renewable	2024–2030	[106,107]
Türkiye	2 GW by 2030; 5 GW by 2035; 70 GW by 2053; H_2 cost < USD 2.4/kg (2035) → USD 1.2/kg (2053)	Renewable	2030–2053	[108]
UAE	1.4 Mtpa low-carbon H_2 by 2031; 15 Mtpa by 2050	Low-carbon focus	2031–2050	[109]
Oman	1 Mtpa by 2030; 3.75 Mtpa by 2040; 7.5–8.5 Mtpa by 2050	Low-carbon focus	2030–2050	[110]
Saudi Arabia (NEOM)	~600 t/day green H_2 (as ammonia) under construction	Low-carbon focus	2026 (start-up)	[111]

5.1. Large-Scale Applications

5.1.1. Industrial Decarbonization Use-Cases

Alkaline water electrolysis (AWE) is emerging as a key technology for the industrial production of hydrogen, providing a reliable and cost-effective alternative to methods based on fossil fuels. Unlike steam methane reforming, the AWE process is clean by nature, producing only hydrogen and oxygen at the point of manufacture. Thanks to its durability and longevity, AWE technology is a suitable solution for the continuous, large-scale supply of hydrogen for processes such as ammonia synthesis, methanol production, refining and the production of direct reduced iron (DRI) in steelmaking. Furthermore, when used alongside suitable post-stream conditioning techniques, hydrogen purities of over 99–99.99% can be attained, thereby meeting the stringent feedstock requirements of these industrial processes [61,112]. The success of the industrial-scale implementation of alkaline water electrolysis (AWE) hinges on the compatibility of the hydrogen produced with the specific needs of downstream processes. In this context, three key integration elements stand out: delivery pressure, feed buffering and purification. These elements ensure the reliable application of AWE technology in processes such as ammonia synthesis, methanol production, refining and steelmaking using direct reduced iron (DRI). In particular, the hydrogen delivery pressure must be tailored to the target sector. Synthesis processes in ammonia and methanol plants, for example, typically require hydrogen feed pressures in the 30–50 bar range, whereas refinery fuel gas networks usually operate at 2–4 bar. Similarly, DRI-based steelmaking requires a hydrogen feed pressure of 30–50 bar to maintain stable reducing conditions [113,114]. In hydrogen supply management, recycling loops and buffer storage are as critical as pressure optimization. Ammonia and methanol plants often incorporate recycling circuits to maximize the efficiency with which they utilize hydrogen, while refineries utilize buffer storage solutions to balance demand-related fluctuations. In DRI applications, specialized hydrogen buffer systems help to maintain stable furnace atmospheres and prevent fluctuations in metallisation rates [115]. Purification strategies also play a decisive role in meeting the stringent purity requirements of each process. In the production of ammonia and methanol, pressure swing adsorption (PSA) systems are usually employed to attain a hydrogen purity level of at least 99.999%. Depending on process flexibility, refiners can choose between PSA and membrane separation technologies. Similarly, PSA systems are widely used in direct reduced iron (DRI) steel production to ensure the quality of the raw materials [116].

5.1.2. System Scaling and Balance-of-Plant

Integrating AWE systems with renewable energy and grid infrastructure significantly increases their scalability and economic viability. Assuming certain conditions, economic assessments have reported hydrogen production costs of approximately $2.94–$3.32 per kilogram for solar-powered AWE systems, and of $6.33–$8.87 for hybrid PV–wind configurations [117]. Furthermore, continuous advances in cell architecture and nickel-based electrode technologies enhance the durability of systems and improve their tolerance to variable renewable energy inputs. At the plant scale, balance-of-plant (BoP) components such as rectifiers, DC–DC converters, gas–liquid separators, dryers, deoxidisers, compression and storage units, and safety systems play a decisive role in determining both the system's footprint and its reliability.

5.1.3. Gas Purity, Crossover, and Safety

Increased gas permeation through the diaphragms can be caused by part-load operation, which can in turn reduce product purity. Carbon-based supercapacitor architectures have been proposed as a solution to this problem. These architectures enable the separation of hydrogen and oxygen evolution over time, thereby reducing gas crossover. Furthermore, the system can support high current densities of 0.952 $A \cdot cm^{-2}$ at 70°C [118]. Furthermore, multi-stage purification systems (gas-liquid separation, cooling/condensation, adsorption, drying, and palladium-based deoxidation) are critical for ensuring product purity at an industrial level. In practice, these systems can achieve a purity level of 99.999%, rendering hydrogen safe for use [119].

5.1.4. Comparative Context (AWE vs PEMWE vs SOEC)

Global hydrogen demand is rapidly increasing in line with decarbonization targets in industry, transportation, and energy storage. In this context, large-scale electrolyzer systems (particularly AWE, PEMWE, and SOEC technologies) play a critical role in low-carbon hydrogen production by integrating with renewable energy sources. The characterization of these technologies for large-scale applications are presented in a comparatively in Table 11. As of 2023, global electrolysis capacity reached approximately 1.4 GW, and annual production capacity reached 25 GW. An installed capacity of 230-520 GW is projected by 2030; however, only approximately 20 GW of these projects have reached final investment decisions [102].

Table 11. Comparative Characteristics of AWE, PEMWE, and SOEC Technologies for Large-Scale Applications

Feature	AWE	PEMWE	SOEC	Reference
Technology Maturity	Mature, widely deployed	Medium, rapidly adopted	Emerging, pilot-scale	**[120]**
Operating Voltage	1.8–2.0 V	1.8–2.2 V	1.0–1.3 V (at high temperature)	**[120]**
Efficiency (HHV)	60–70%	65–75%	80–90%	**[102]**
Dynamic Response	Slow, less flexible	Fast, suitable for intermittent power	Moderate, sensitive to thermal cycling	**[120]**
Lifetime & Durability	Long, robust materials	Medium, requires PGM electrodes	Medium, ceramic degradation risk	**[120]**
CAPEX	Low	Medium	High	**[102]**
OPEX	Low	Medium	Medium–High	**[102]**
LCOH ($/kg H_2)*	2–4	3–6	4–7	**[102]**
BoP Considerations	Standard rectifiers, compressors, storage	DC-DC converters, high-pressure systems	High-temperature heat integration, specialized components	**[120]**

Relative to PEMWE, AWEs typically operate at lower current densities but with lower specific capital cost and non noble catalysts; compared with SOEC, AWEs avoid high temperature materials challenges and offer higher commercial maturity today. Consequently, AWEs often dominate in large, base loaded installations where capex and stack replacement costs drive levelized costs, while PEM's faster dynamics may be preferred for highly intermittent duty cycles [102]. In terms of application, AWE stands out with its low investment cost and long lifespan, particularly in baseload generation. PEM, with its high dynamic response, is preferred for direct integration with intermittent sources such as wind and solar. SOEC, on the other hand, stands out with its high temperature efficiency (80-90% HHV), but due to its technological maturity and high capital expenditures, it has not yet reached widespread commercial use. At the industrial scale, these technologies are actively implemented in ammonia, methanol, and steel production, energy storage, and grid balancing projects [102].

5.1.5. Transitional/Near-Term Applications

In transitional applications, oxyhydrogen (H_2/O_2) generated by small-scale alkaline water electrolyzers (AWEs) has been investigated for combustion enhancement in compression-ignition (CI) engines. For example, experiments on a 10 HP single-cylinder diesel engine demonstrated approximately 14% fuel savings at optimized HHO flow rates, alongside significant reductions in CO (~23%) and NO_x (~15.5%) emissions, without requiring major engine modifications [121, 122]. Exhaust emissions in these studies were quantified using a full-flow constant-volume dilution tunnel system, with non-dispersive infrared (NDIR) analyzers for CO/CO_2 and chemiluminescence detectors for NO_x, following ISO 8178 test cycle protocols [123]. This ensured repeatable measurements under standardized load conditions. Despite these promising results, scalability to large marine, heavy-duty, or stationary power plants remains constrained due to: the relatively low volumetric energy density of HHO, the parasitic electrical demand of in-situ electrolyzers, and the diminishing net

efficiency gains at higher power outputs. Consequently, HHO-assisted combustion is generally considered a niche or bridging solution, suited for targeted emission mitigation and incremental efficiency improvements in existing diesel fleets, until fully decarbonized alternatives (e.g., 100% hydrogen combustion or fuel cells) become economically and infrastructurally viable.

5.2. Renewable Integration

Integrating alkaline water electrolyzers (AWEs) with renewable energy infrastructure can significantly increase the scalability and economic viability of systems. Studies have shown that integrating AWE with large-scale photovoltaic (PV) and wind energy systems can significantly reduce hydrogen production costs, achieving competitive prices and high efficiency under optimal operating conditions. For instance, the cost of producing hydrogen has been reported to range from $2.94–$3.32 per kg when using solar energy alone. In contrast, for integrated configurations using both PV and wind systems, the cost ranges from approximately $6.33–$8.87 per kg [124]. Furthermore, improvements in electrolysis design and system integration are enhancing the technology's durability, operational flexibility and compatibility with variable renewable energy sources. The combination of renewable energy and AWE shows great promise in meeting hydrogen needs in areas such as energy storage, transportation, chemical synthesis, and other industrial applications. This shows that AWE will be crucial in developing a sustainable hydrogen economy [125]. AWEs can absorb surplus wind generation, mitigating curtailment and converting variability into storable hydrogen for later use in industry, transport, or power. In high-wind penetration regions, curtailment can reach 5–15% of annual potential output—equivalent to >1 TWh/year in some European and Chinese provinces [102]. If captured for electrolysis, this surplus could produce over 200 kt H_2 annually in certain markets.

5.2.1. Multi-Energy System

Multi-energy systems (MES) represent an innovative approach that aims to optimize energy production and consumption by integrating different energy streams, such as electricity, heat and hydrogen, thereby providing cross-sectoral flexibility. In this context, alkaline water electrolysis units (AWEs) play a critical role in MES structures due to their capacity to convert renewable electricity into green hydrogen and their ability to recover heat generated during the process. Integrating AWEs increases system efficiency and enables the development of operational strategies that support sustainability and economic benefits [126,127]. Alkaline water electrolyzers (AWEs) produce hydrogen and significantly improve energy utilization by recovering waste heat generated during electrolysis. A detailed dynamic model has been developed to characterize the interactions between electricity, heat and hydrogen, and to capture the non-linear relationship between electrolysis efficiency, temperature and energy flows. The Economic Model Predictive Control (EMPC) approach optimizes daily operations by integrating a mixed integer linear programming (MILP) framework with the nonlinear P2H2 model. This achieves high computational efficiency while maintaining model accuracy. Indeed, this methodology demonstrates that cost savings can be achieved by 59% compared to rule-based strategies and 38% compared to traditional economic strategies without the P2H2 model. Using AWEs within the MES framework enables the storage of excess renewable energy as hydrogen, mitigates wind disruption and enables heat recovery for district heating systems (DHSs). In the context of Denmark's Bornholm Energy Island, for example, AWEs have played an active role in dynamically balancing energy flows by integrating with wind turbines, combined heat and power (CHP) plants, and battery energy storage systems (BESS) [127,128].

5.2.2. Grid Services and Operational Flexibility

When equipped with the right power electronics and control systems, alkaline water electrolyzers (AWEs) can help balance the grid by providing limited load-following capabilities. By contrast, PEM electrolyzers can typically handle load increases of around 5–10% of their nominal capacity per second, whereas slower-responding AWE systems operate at load ramp rates of around 1–5 MW per minute. However, AWEs can maintain minimum stable loads of around 10–20% of their nominal capacity, but require a cold restart that takes several minutes. Although there is less precise performance data for AWEs in the literature than for PEM systems, industrial-scale dynamic performance studies have confirmed these operational limitations [129,130,131]. In order to expand the operational range of alkaline water electrolyzers (AWEs) and reduce degradation caused by frequent cycling, intensive research is being conducted into new diaphragm materials and advanced control strategies. Meanwhile, AWEs and other electrolyzer technologies are increasingly being recognized as flexible resources capable of providing ancillary services such as frequency regulation, rotational reserve and voltage support. The ability of these systems to operate as controllable loads is dependent on their ability to adjust their power draw according to grid needs. However, the economic viability of these services depends not only on technical capabilities, but also on supportive regulatory frameworks, appropriate market structures (e.g. minimum bid sizes) and favourable operating conditions. From a market balance perspective, the participation of electrolyzers in ancillary services is largely limited by policy and market factors. This results in only a small amount of an electrolyzer's capacity being allocated to such services [131,132].

5.3. CAPEX, OPEX and LCOH

The design and economic evaluation of alkaline electrolyzers is predominantly informed by a cost-benefit analysis of capital expenditure (CAPEX) and operational expenditure (OPEX). Whilst alkaline systems generally offer lower capital costs (CAPEX) compared to PEM electrolyzers, both CAPEX and operating costs (OPEX) must be considered when selecting a technology. In the context of business operations, particularly with regard to the field of operations management, OPEX can exert considerable influence on the overall cost structure. Comprehensive capital expenditure (CAPEX) and operating expenditure (OPEX) modelling, incorporating financial metrics such as return on investment (ROI) and net present value (NPV), allows for more accurate investment evaluations and contributes to risk management by providing insights into equipment failures, maintenance requirements, and electricity price fluctuations.

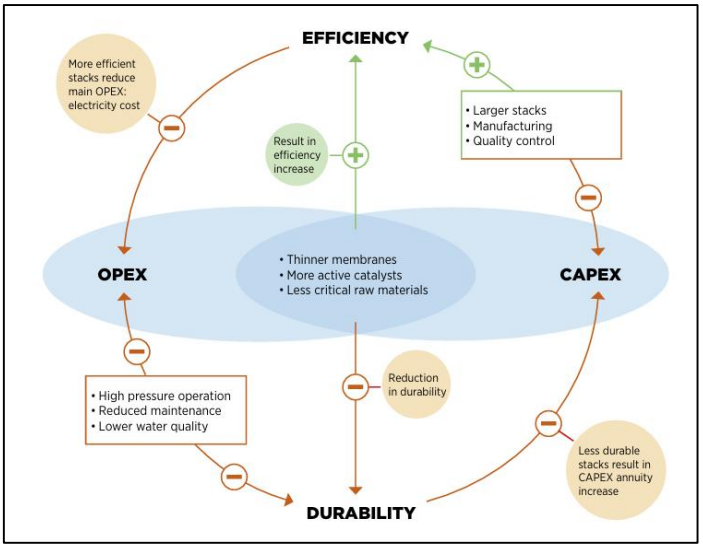

Figure 13. The relationship between efficiency, durability and cost in electrolyzers. Reproduced from IRENA (2020), [19].

From an operational perspective, labour, maintenance, and minor consumables (e.g. deionized water and KOH) constitute the second-highest cost items after electricity. The enhancement of economic sustainability can be achieved through the improvement of system performance and the strategic utilization of affordable renewable electricity. In general, considering CAPEX and OPEX calculations in conjunction with performance criteria and energy efficiency considerations enables the development of cost reduction strategies for large-scale applications and forms the basis for both the economic and environmental sustainability of alkaline electrolyzer projects [133]. Figure 13 provides a schematic representation illustrating the interplay between efficiency, durability, and cost in electrolyzers [19].

As stated in the 2020 report by the International Renewable Energy Agency (IRENA), the integration of reduced electricity production costs and the utilization of high-efficiency, long-life electrolyzers has the potential to offset approximately 80% of the costs associated with hydrogen production. It is projected that, in the long term, there will be a reduction in the cost of green hydrogen production by up to 85%, attributable to a combination of factors, including a reduction in electricity supply costs, increased capital investments in electrolyzers, and optimization of system efficiency [19]. As illustrated by Figure 14, a hypothetical cost-reduction scenario is proposed for the production of hydrogen.

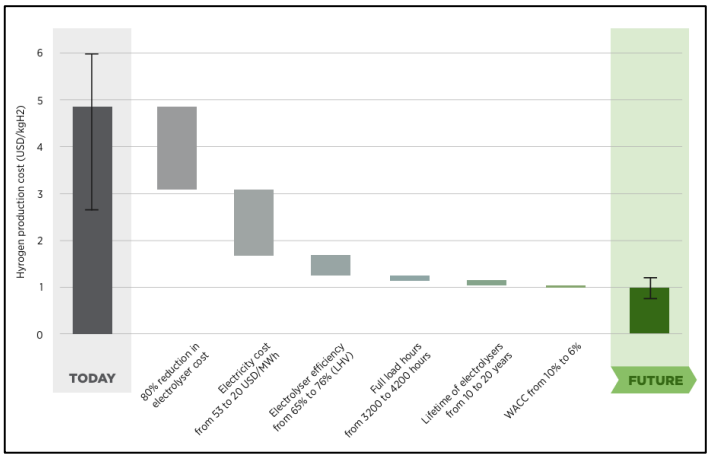

Figure 14. Scenario for reducing hydrogen production cost. Reproduced from IRENA (2020), [19].

5.3.1. OPEX (Operational Expenditure) Analysis

Operating costs (OPEX) for alkaline electrolyzers represent a pivotal factor in determining the economic sustainability of the system. Electricity consumption has been identified as the primary operational expenditure (OPEX) item, with approximately 60-80% of hydrogen production costs directly associated with electricity costs. In addition to electricity, labour, maintenance and repair activities, and minor consumables (e.g. deionized water, sealants) constitute other important components of OPEX. The proportion of total operating costs accounted for by electricity is typically between 50 and 80 per cent, depending on the scale of the plant, thus making it the largest component of OPEX. For instance, at a pilot manufacturing facility located in the city of Seongnam, the augmentation of its daily operational hours from four to twenty-four hours led to an escalation in electricity expenditures from 54% to 71%. Concurrently, expenditures on labour and the depreciation of equipment diminished [134]. This clearly demonstrates that an increase in operating hours has a direct impact on the relative cost of labour and maintenance, while concomitantly increasing the weight of energy costs in OPEX. The cost of electricity, which is the largest contributor to OPEX in alkaline electrolyzers, strongly depends on the energy source. Renewable options such as solar PV and onshore wind are preferred for green hydrogen production; however, their intermittent availability can limit operational hours and, consequently, affect OPEX. According to the U.S. Energy Information Administration, the levelized cost of electricity (LCOE) for new resources entering service in 2028 is estimated in Table 12 [135]. This table highlights that selecting low-cost renewable electricity can significantly reduce OPEX in green hydrogen production, emphasizing the importance of energy source choice for economic sustainability. Operating costs are slightly affected by the water feedstock. For every kilogram of hydrogen produced, large-scale alkaline electrolyzers require approximately 14 liters of deionized water [136]. Similarly, the electrolyte potassium hydroxide (KOH), currently sold at approximately $0.563 per kilogram, contributes negligibly to operating costs [137].

Table 12. Estimated LCOE for new resources entering service in 2028 [135].

Technology	Source	LCOE [USD/kWh]
dispatchable	ultra-super critical coal	0.089 $/kWh
	biomass	0.077 $/kWh
	advanced nuclear	0.071 $/kWh
	combined-cycle	0.042 $/kWh
	geothermal	0.037 $/kWh
resource-constrained	wind, offshore	0.100 $/kWh
	hydroelectric	0.057 $/kWh
	PV-battery hybrid	0.036 $/kWh
	wind, onshore	0.031 $/kWh
	solar PV	0.023 $/kWh
capacity resource	combustion turbine	0.128 $/kWh
	battery storage	0.118 $/kWh

The facility's configuration and operating method have a significant impact on labor and maintenance costs. Generally, operating, maintenance, and administrative labor costs account for 15–18% of total operating costs, ranging from $42,890 to $171,560 annually [134]. The main component of maintenance is chimney replacement, which has historically cost approximately half the original chimney price. However, if such a replacement is undertaken with the objective of extending the system's lifespan, it can be considered a capital expense (CAPEX) [136]. Consequently, the OPEX analysis reveals that electricity accounts for the largest share of operating costs, while labour, maintenance, and consumables have more limited but still notable secondary effects. Strategic focus on energy efficiency, low-cost renewable electricity, and optimized maintenance and workforce planning can substantially enhance the economic viability of alkaline hydrogen production.

Figure 15. OPEX Components of AWE System

5.3.2. CAPEX (Capital Expenditure) Analysis

Capital expenditures (CAPEX) refer to the initial costs associated with the installation and long-term operation of alkaline electrolyzers. Key elements of CAPEX include the electrolyzer stack, the membrane electrode assembly (MEA), and Balance of Plant (BoP) systems, in addition to installation and engineering, procurement, and construction (EPC) activities. It is imperative to comprehend the concept of capital expenditure (CAPEX) in order to assess the economic viability of green hydrogen production, especially in the context of scaling and technological considerations. As demonstrated in Figure 16, the cost breakdown for a 1 MW Alkaline electrolyzer system is illustrated.

The electrolyzer stack is the central component, where the electrochemical reactions occur. Stack costs typically account for 40–50% of total CAPEX, with electrodes and diaphragms comprising the largest portion [19]. The accompanying material summary in Table 6 illustrate the components used in baseline (2020) and advanced (2030) AE stack designs. Such advancements in materials, combined with higher current densities and improved manufacturing processes, are projected to reduce stack costs from 242–388 €/kW in 2020 to 52–79 €/kW by 2030 [138,139]. Automation, learning-by-doing, and economies of scale are highlighted as critical factors driving these reductions. As illustrated in Table 13, the materials selected for the fundamental and sophisticated design of the AWE stack have been meticulously delineated.

Table 13. Materials used in baseline and advanced design AWE stack [138]

Components	Baseline (2020)	Advanced (2030)
Separator	Zirfon UTP 500	Zirfon UTP 220
Cathode	Ni plated perforated Carbon steel (156 μm)	Ni Mesh
Anode	Ni plated perforated Carbon steel (156 μm)	Raney Ni Coating (75 μm) Ni Mesh
Mattress	Not applicable	Ni mattress
Frames	Carbon steel (NEL design)	PSU+ 30% Glass Fiber
Gasket	Rubber	PTFE
Bipolar Plate	Ni plated Carbon steel (200 μm)	Ni plated Carbon steel (200 μm)
End Plates	Carbon Steel	Carbon Steel

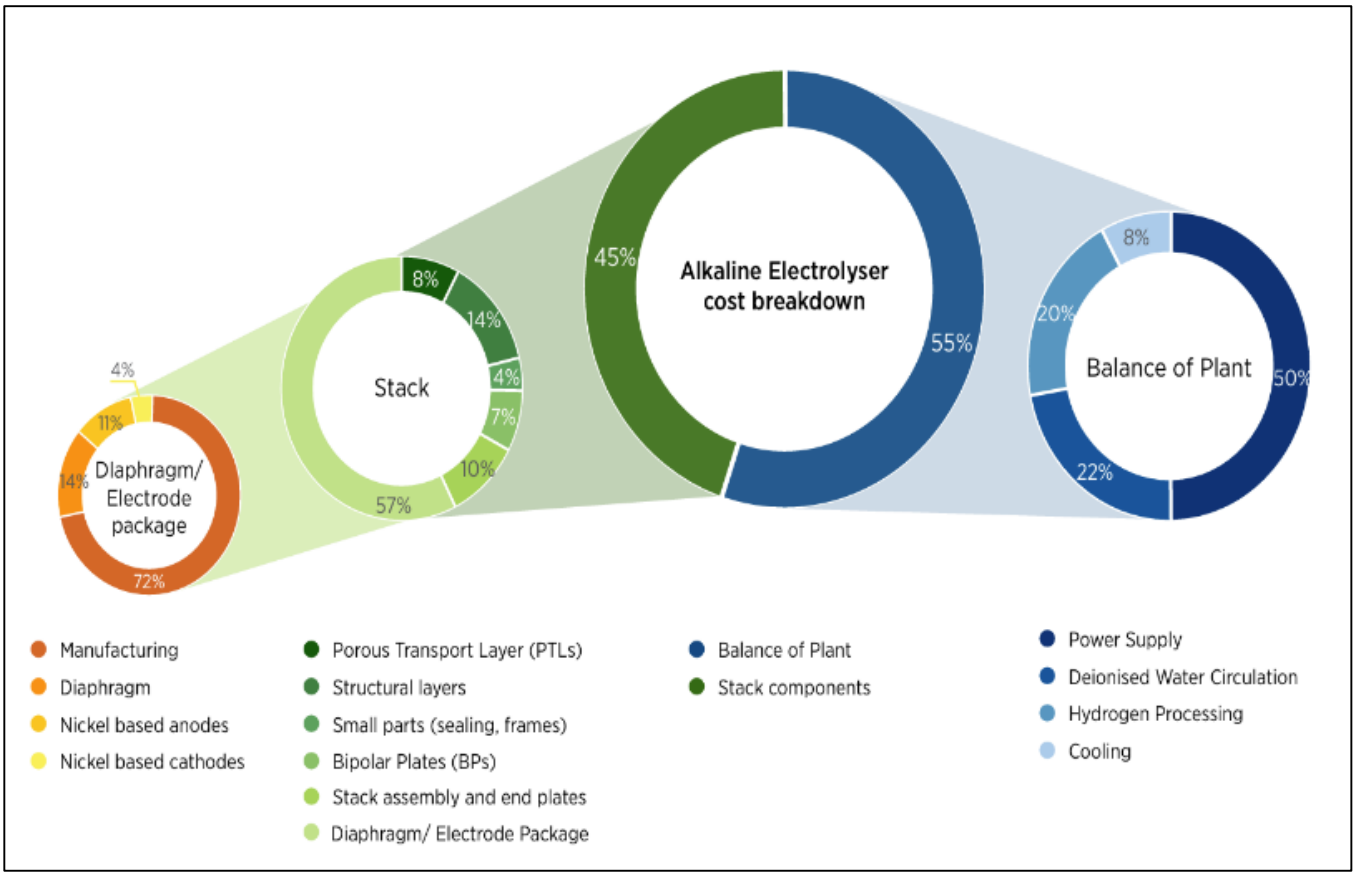

Figure 16. Cost breakdown for 1 MW AWE System. Reproduced from IRENA (2020), [19]

5.3.3. Levelized Cost of Hydrogen (LCOH)

Water treatment units, pumps, compressors, tanks for storing hydrogen and oxygen, electrical infrastructure, mechanical piping, and instrumentation are among the crucial auxiliary systems that make up the BoP. BoP's proportional share declines with scaling, even though it can account for as much as 60% of the overall system cost for small-scale electrolyzers [140]. The most expensive components of BoP are cooling systems and power electronics, particularly AC/DC rectifiers; however, modular designs and system optimization can reduce costs by up to 10% [141]. For instance, a 100 MW system's mechanical BoP is expected to drop from $515 to $418/kW, but the electrical BoP might marginally rise as a result of increased power demands [139]. Installation and commissioning, including EPC activities, are additional CAPEX components. These cover site preparation, mechanical and electrical connections, technical design, and logistics. Future projections for 1 MW alkaline systems estimate total CAPEX in the range of USD 700–1000/kW, with costs decreasing further for larger-scale plants due to economies of scale and design optimization [140,142,143].

The levelized cost of hydrogen (LCOH) is a critical metric for evaluating the long-term economic viability of a system. The term 'LCOH' is defined as a holistic function of factors such as total capital expenditures (CAPEX), operating expenses (OPEX), electricity price, system life, and annual production [144]. Therefore, the application of LCOH analysis provides a comprehensive evaluation of technological efficiency. In addition to this, it also reflects fluctuations in price, as well as economies of scale effects that occur within the domain of energy markets. LCOH for electrolyzers using renewable electricity has been estimated in a number of studies. Shaner et al. discovered 6–12 USD/kgH_2 for alkaline electrolyzers integrated with PV systems [145], while Yu et al. reported a range of 2.28–7.43 USD/kgH_2 in various countries [146]. With estimates of 3.50 to 5.46 USD/kgH_2 for nuclear PWR-powered systems, AE technologies can also make use of current nuclear power, resulting in lower hydrogen costs [147]. Renewable-based LCOH may eventually reach levels competitive with nuclear-powered systems as a result of declining material costs and seasonal intermittency issues as renewable energy technologies advance [148]. Regional analyses further demonstrate the influence of energy source and grid integration on LCOH. For instance, based on electrolyzer costs of $250/kW reported by IRENA, the LCOH for a 0.7 MW small-scale facility operating 20 hours per day is approximately $12.8/kg$H_2$, slightly lower than the $15.6/kg$H_2$ calculated using actual operational data [19,134]. When grid electricity was added to solar-only systems in Japan's Kyushu region, the LCOH went down from $3.61/kg$H_2$ to $3.20/kg$H_2$. Wind-only systems went down from $3.57/kg$H_2$ to $2.49/kg$H_2$ under the same conditions [149]. The LCOH in Saudi Arabia changes based on how renewable energy is combined with electrolyzers and fuel cells. The LCOH values for PV-FC systems are between 40 USD/kgH_2 in Jeddah and 45.4 USD/kgH_2 in Dhahran. Wind-FC systems usually cost more, with prices ranging from 55.8 USD/kgH_2 in Jeddah to 57.7 USD/kgH_2 in Dhahran. The lowest LCOH value for hybrid PV-Wind-FC setups is 47.2 USD/kgH_2 in Riyadh, and the highest is 63.8 USD/kgH_2 in Toronto. These results highlight that both the choice of renewable energy technology and regional factors, such as solar and wind resource availability, significantly influence hydrogen production costs [150]. As illustrated in Table 14, a comparative analysis of hydrogen production costs per kilogramme is presented, with data drawn from various countries and technologies. Table 14 provides a comparative overview of the costs associated with hydrogen production per kilogramme across various countries and technologies. The data presented in the Table 14 unequivocally demonstrates that LCOH is not a static figure, but a dynamic metric requiring multidimensional analysis. Geographic and regional factors have been identified as having a significant impact on final costs. For instance, the high wind potential in Ireland allows for a competitive LCOH target of 2.75 €/kgH2. Conversely, analysis for China assuming a thermal-dominated grid results in a significantly higher LCOH of approximately 3.996 €/kgH2 (RMB 33.30/kg) [152,153]. This indicates that the cost of green hydrogen is contingent on the cost and carbon intensity of the electricity utilized. It has been demonstrated by a considerable number of studies that electricity costs account for more than 60-70% of total LCOH [151-155]

Table 14. Levelized cost of hydrogen values in various countries and technologies.

LCOH Value ($/kg or €/kg)	Production Method / Technology	Region / Country	Main Focus	Ref.
For AWE; 4.605 $/kg$H_2$ (unsubsidized) 1.605 $/kg$H_2$ (with IRA) For PEMWE: 5.485 $/kg$H_2$ (unsubsidized) 2.485 $/kg$H_2$ (with IRA)	Wind-powered Electrolysis, Green H_2 ,(AWE, PEMWE)	USA (Wyoming)	The Inflation Reduction Act (IRA) tax credits have a dramatic effect on reducing costs for LCOH.	[151]
For 2030 Projection: ranges from 3.53 €/kgH_2 to 4.01 €/kgH_2 For 2040 Projection: ranges from 2.75 €/kgH_2 to 3.34 €/kgH_2	Green H_2 (PEMWE)	Ireland (Dublin, Wexford, Cork)	The impact of the potential of regional renewable resources (Wind offshore and Solar PV) on LCOH and future cost projections.	[152]
For SMR: 17.60 RMB/kg For CGH: 10.70 RMB/kg For SMR+CCUS: 20.06 RMB/kg For ATR+CCUS: 19.94 RMB/kg For CGH+CCUS: 11.45 RMB/kg For MSW: 10.95 RMB/kg For AWE: 33.30 RMB/kg For PEMWE: 34.85 RMB/kg For SOEC: 38.42 RMB/kg (1 RMB ≅ 0,14 $)	Natural gas hydrogen production (SMR, SMR + CCUS, ATR + CCUS), Coal hydrogen production (CGH, CGH + CCUS), municipal solid waste hydrogen production (MSW), and AWE, PEWE, SOEC	China	To analyse the production costs and cost structures of nine hydrogen production processes operating at the same scale.	[153]
For Grid; LCOH with oxygen: 7.91 €/kgH_2 LCOH without oxygen: 7.44 €/kgH_2 For Grid+PV: LCOH with oxygen: 6.75 €/kgH_2 LCOH without oxygen: 6.28 €/kgH_2	Green H_2 (AWE)	Germany	In order to ascertain the most profitable financial model for the energy system project. two scenarios were examined: the operation of the on-site water electrolysis with electricity from the grid only, or with a combination of its own PV system and PV electricity supplied from the grid.	[154]
For Gray H_2 (SMR): LCOH between 1.50 and 2.50 $/kg$H_2$ For Blue H_2 (SMR+CCS): LCOH between 2.00 and 3.50 $/kg$H_2$ For Green H_2 (Electrolysis): LCOH between 3.50 and 6.00 $/kg$H_2$	Gray H_2 (SMR) Blue H_2 (SMR+CCS) Green H_2 (Electrolysis)	USA	A thorough and detailed techno-economic assessment of hydrogen production for different hydrogen colors, including an analysis of cost structures, investment feasibility, infrastructure challenges and policy-driven market dynamics.	[155]

5.3.3.1. LCOH Results for Base Current and Future Cases

A decline in LCOH is expected worldwide by 2050. On average, there was a decline of approximately 35% by 2030, followed by a further 30% by 2050. An average cost of approximately 0.67 to 2.6 USD/kg is expected for 2050 [156]. These trends can be linked to energy policies, electricity costs, and access to renewable energy in different regions. The average LCOH value for Europe is set at $2/kg in 2022, with further declines expected [157]. However, the United Arab Emirates is projected to reach similar values to Europe by 2050 [158]. Europe is particularly cost-advantaged using renewable energy sources. A detailed LCOH analysis employing the H2A model was conducted in a report published by the National Renewable Energy Laboratory (NREL). The study evaluated both low-pressure (LP) and high-pressure (HP) existing centralized scenarios, as well as future centralized LA technology scenarios. The analysis was predicated on the assumption that the plant would operate at a capacity factor of 97%, and that the electricity price would be $0.03/kWh. In such circumstances, the total installation cost of a 100 MW plant was estimated at $125.9 million, while the cost of a 1 GW plant was estimated at $779.5 million. However, given the recent technological advances and the impact of economies of scale, significant cost reductions are anticipated. Indeed, it is predicted that in the future, the installation cost of a 100 MW system could fall to $85.3 million, and the cost of a 1 GW system could fall to $516.2 million [139]. The findings indicate that both technological advances and scale-up play critical roles in making AWE systems more competitive in the long term. Consequently, LCOH analysis is a critical tool for determining the economic competitiveness of AWE technology. As demonstrated in Figure 17, the competitiveness of alkaline electrolyzers in hydrogen production at costs below $2/kg is contingent on the accessibility of low-cost electricity supply and the scalability advantages offered by the technology.

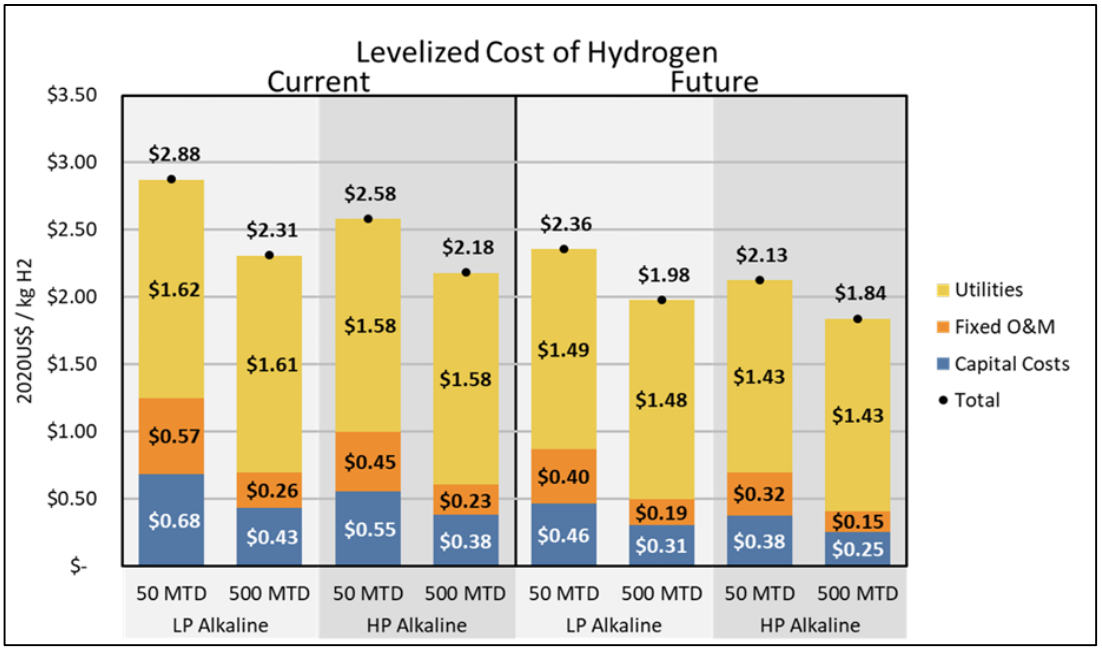

Figure 17. Projected levelized cost of hydrogen (LCOH) summarized by sub-component for low pressure (LP) and high pressure (HP) Alkaline. Reproduced from Acevedo, Y. M. et al. (2023), [139], licensed under CC BY 4.0.

6. ENVIRONMENTAL AND SUSTAINABILITY CONSIDERATIONS

While alkaline water electrolyzers (AWEs) offer significant economic advantages in scaling up green hydrogen production, they also require comprehensive environmental and sustainability assessment. In this context, life cycle analyses (LCAs), water use, gas purity, and recycling strategies are of critical importance in order to understand the technology's long-term environmental impacts and its sustainability potential.

6.1. Lifecycle Analysis (LCA)

As delineated by the ISO 14040 and ISO 14044 standards, life cycle analysis (LCA) constitutes a pivotal environmental management instrument. This analytical framework involves the examination of the prospective interactions between a technical system (techno sphere) and the surrounding environment. A thorough Life Cycle Assessment (LCA) of alkaline electrolyzers necessitates the evaluation of the environmental implications at each stage of the process, encompassing raw material extraction, production, operation, end-of-life disposal, and recycling [159]. For instance, Hoppe and Minke's study demonstrates that the production of an AWE system from recycled materials results in a 50% reduction in global warming potential (GWP) in comparison with copper materials [160]. In addition, the research conducted by Koj et al. on the German case study has revealed a crucial link between nickel usage and water treatment processes, and the substantial environmental impact of AWE systems. However, the same study posits that emissions will gradually decrease, falling from 27.5 kg CO_2-eq per kg H_2 produced to 1.33 kg CO_2-eq by 2045, thanks to technological advances and increased integration of renewable energy [161]. The issue of end-of-life disposal remains a critical consideration for the environmental sustainability of alkaline electrolyzers. In this regard, the development of closed-loop recycling systems has the potential to both minimize waste and reduce reliance on raw material extraction. A number of studies have been conducted that suggest implementing effective recycling strategies can reduce the environmental impact of the system by as much as 30% [162,163].

6.2. Water Use, Gas Purity and Recycling Strategies

Water, the primary input for hydrogen production, is a key factor to consider in AWE's environmental assessment. It is estimated that approximately 9 liters of pure water are required to produce 1 kilogram of hydrogen. This underscores the critical importance of effective water management in large-scale hydrogen production projects. It is evident that seawater desalination and wastewater reuse are two sustainable strategies that are of particular importance in regions experiencing water stress [164,165]. AWE systems have also been demonstrated to be capable of producing hydrogen of a high degree of purity (>99.9%), however, the effective maintenance of gas purity is dependent upon the effective use of pressure swing adsorption (PSA), membrane separation, and gas-liquid separators. Moreover, the recovery and reuse of the KOH electrolyte solutions employed in the system have been shown to result in a reduction of environmental waste and a corresponding decrease in operating expenses. Within this paradigm, closed-loop recycling strategies are pivotal to ensure the long-term environmental sustainability of AWE [160,163].

6.3. Comparison with Other H_2 Production Methods

The impact of AWE on environmental sustainability is more clearly delineated when compared to other hydrogen production methods. Steam methane reforming (SMR), the predominant method of hydrogen production, with a global share exceeding 90%, has been found to generate approximately 8–10 kg of CO_2 per 1 kg of hydrogen [19,166]. Furthermore, coal gasification has an even higher emissions intensity. Conversely, AWE produces negligible direct emissions when operated with renewable energy [161]. While PEM electrolysis offers higher current densities and compact designs, the use of rare and costly metals such as platinum and iridium represents a significant sustainability constraint. Systems utilising SOEC technology demonstrate considerable potential for efficiency enhancement; however, they are also susceptible to long-term stability and material durability concerns arising from the elevated operating temperatures [20,45]. In this context, AWE is distinguished as the most mature and viable option in terms of balancing sustainability and environmental benefits, owing to its inexpensive, abundant nickel-based electrode materials and long-life design.

7. CONCLUSION

This study comprehensively examines the role of alkaline water electrolysis (AWE) technology in green hydrogen production, a technology central to the global energy transition. In the context of the global climate change emergency, there is an increasing need for low-carbon energy carriers, and the strategic importance of hydrogen is becoming ever more apparent. This study provides substantial evidence to support the conclusion that AWE is a significant technology in the production of green hydrogen, owing to its commercial maturity, low investment and operating costs, stable performance, and its capacity for integration with renewable energy sources. The performance and economic viability of AWE are directly related to the design and material properties of key components such as electrodes, electrolytes, membranes, and separators. Recent advancements in membrane technologies, electrode materials with enhanced corrosion resistance, and more efficient electrolyte solutions have contributed to increased energy efficiency and extended system life. Furthermore, advancements in cell design, exemplified by bipolar and zero-gap configurations, have facilitated enhanced current densities and diminished ohmic losses, thereby augmenting the technology's competitiveness. Nevertheless, challenges such as efficiency losses at part loads and limited dynamic response time persist as areas for improvement in the domains of material utilization and system control. From an economic perspective, analyses of capital expenditure (CAPEX), operating expenditure

(OPEX) and levelized cost of hydrogen (LCOH) calculations demonstrate that AWE offers a sustainable and viable solution for large-scale green hydrogen production. The affordability of low-cost renewable electricity sources, economies of scale, and advanced control strategies have been shown to have a significant impact on the cost of hydrogen production. Projections from organizations such as the National Renewable Energy Laboratory (NREL) and the International Renewable Energy Agency (IRENA) indicate that, with technological advancements, it may be possible to achieve hydrogen production costs below $2/kg, which would render AWE a significant component of energy markets in the long term. In this context, in countries with high renewable energy potential – especially Türkiye – AWE is expected to emerge as a competitive option for both energy storage solutions and industrial process integration. However, in order to achieve this potential, it is essential that infrastructure, storage, and distribution investments are supported by a comprehensive national roadmap. The present study evaluates alkaline water electrolysis (AWE) technology from multiple perspectives, including, but not limited to, electrochemical and material considerations. Additionally, the investigation encompasses a holistic framework that considers market dynamics, policy objectives, and environmental sustainability. In addition, the study provides an analytical assessment that comprehensively examines the strategic roadmaps of Türkiye and the MENA region, relating these objectives to electrolyzer efficiency, cell/system design, and cost drivers. It thereby demonstrates the potential of regional energy transformation with concrete technical and economic indicators. A review of the extant literature indicates that research on next-generation membranes and catalysts for AEM and SOEC is currently fragmented, and that differences in CAPEX–OPEX methodologies and currencies limit the comparability of results. It is vital to enhance the scale and scope of experimental and modelling research on the integration of renewable energy, in order to adapt technologies to actual real-world field conditions and develop robust business models. Therefore, the present study is distinguished not only by its comprehensive review of the relevant literature, but also by its integration of the policy-market-technology axis. This integration provides a guiding framework for the design of future research and the development of future applications. In conclusion, the advantages of AWE technology in terms of environmental sustainability, economic viability and technical maturity position it at the center of green hydrogen production. Future studies are advised to concentrate on the following areas: high-performance electrode and membrane materials, advanced electrolyte solutions, new cell designs and intelligent control strategies. In addition, the implementation of solutions in areas such as system integration and the recovery of waste heat, in addition to adaptation to multi-energy systems (MES), is expected to enhance AWE's efficiency, thereby contributing to the promotion of both economic and environmental sustainability. This will enable AWE to become a leading technology not only in today's clean energy systems, but also in future ones.

Acknowledgment

The authors would like to express their sincere thanks to Senanur Tekin, Erdem Erçakmak, İbrahim Yıldız, Mahmut Esad Aslan and İsmail Korkmaz for their valuable contributions and insights.

REFERENCES

[1] Global Hydrogen Review 2025, Paris. [Online]. Available: https://www.iea.org/reports/global-energy-review-2025, Accessed: Mar. 2025.

[2] C. M. S. Kumar et al., "Solar energy: A promising renewable source for meeting energy demand in Indian agriculture applications," Sustainable Energy Technologies and Assessments, vol. 55, 102905, 2023.

[3] H. Khurshid, B. S. Mohammed, A. M. Al-Yacouby, M. S. Liew, and N. A. W. A. Zawawi, "Analysis of hybrid offshore renewable energy sources for power generation: A literature review of hybrid solar, wind, and waves energy systems," Developments in the Built Environment, vol. 19, 100497, 2024.

[4] Q. Shao and H. W. Lo, "Advancing renewable energy technologies in remote areas: Exploring key success factors and interdependencies for sustainable wind energy development," Sustainable Energy Technologies and Assessments, vol. 79, 104367, 2025.

[5] S. Serag, A. Echchelh, and B. Morrone, "Hydroelectric and hydrogen storage systems for electric energy produced from renewable energy sources," Energy Engineering: Journal of the Association of Energy Engineers, vol. 121, no. 10, p. 2719, 2024.

[6] N. A. Pambudi and I. R. Nanda, "Understanding knowledge, perception, and acceptance of geothermal energy among Indonesian students: Implications for sustainable renewable energy initiatives," Sustainable Energy Technologies and Assessments, vol. 79, 104357, 2025.

[7] F. Ceglia, E. Marrasso, C. Roselli, and M. Sasso, "Energy and environmental assessment of a biomass-based renewable energy community including photovoltaic and hydroelectric systems," Energy, vol. 282, 128348, 2023.

[8] M. Bianchi and I. F. Fernandez, "A systematic methodology to assess local economic impacts of ocean renewable energy projects: Application to a tidal energy farm," Renewable Energy, vol. 221, 119853, 2024.

[9] A. Alanazi, "Evaluating the feasibility of wave energy converters for renewable energy expansion in Saudi Arabia," Results in Engineering, vol. 25, 103956, 2025.

[10] L. Mulky et al., "An overview of hydrogen storage technologies – Key challenges and opportunities," Materials Chemistry and Physics, vol. 325, 129710, 2024.

[11] C. Tarhan and M. A. Çil, "A study on hydrogen, the clean energy of the future: Hydrogen storage methods," Journal of Energy Storage, vol. 40, 102676, 2021.

[12] B. Oussmou, S. Sigue, and S. Abderafi, "Review of green hydrogen production technologies, to choose the optimal process of electrolysis–renewable energy," Renewable and Sustainable Energy Reviews, vol. 225, 116205, 2026.

[13] S. Bhardwaj and A. Jayant, "Advancements in electrolysis technologies: Exploring the potential of oxyhydrogen as a clean energy source," Fuel, vol. 389, 134522, 2025.

[14] K. J. Yoon, S. Lee, S. Y. Park, and N. Q. Minh, "Advances in high-temperature solid oxide electrolysis technology for clean hydrogen and chemical production: materials, cells, stacks, systems and economics," Progress in Materials Science, Art. no. 101520, 2025.

[15] S. G. Nnabuife et al., "Integration of renewable energy sources in tandem with electrolysis: A technology review for green hydrogen production," International Journal of Hydrogen Energy, vol. 107, pp. 218–240, 2025.

[16] M. Chatenet et al., "Water electrolysis: from textbook knowledge to the latest scientific strategies and industrial developments," Chemical Society Reviews, vol. 51, no. 11, pp. 4583–4762, 2022.

[17] J. Chi and H. Yu, "Water electrolysis based on renewable energy for hydrogen production," Chinese Journal of Catalysis, vol. 39, no. 3, pp. 390–394, 2018.

[18] M. El-Shafie, "Hydrogen production by water electrolysis technologies: A review," Results in Engineering, vol. 20, Art. no. 101426, 2023.

[19] IRENA, Green Hydrogen Cost Reduction: Scaling Up Electrolysers to Meet the 1.5 °C Climate Goal. International Renewable Energy Agency, Abu Dhabi, ISBN: 978-92-9260-295-6, 2020. [Online]. Available: https://www.irena.org/-/media/Files/IRENA/Agency/Publication/2020/Dec/IRENA_Green_hydrogen_cost_2020.pdf, Accessed: Oct. 2025.

[20] S. S. Kumar and H. Lim, "An overview of water electrolysis technologies for green hydrogen production," Energy Reports, vol. 8, pp. 13793–13813, 2022.

[21] N. Sezer, S. Bayhan, U. Fesli, and A. Sanfilippo, "A comprehensive review of the state-of-the-art of proton exchange membrane water electrolysis," Materials Science for Energy Technologies, vol. 8, pp. 44–65, 2025.

[22] S. Palmas et al., "Anion exchange membrane: A valuable perspective in emerging technologies of low temperature water electrolysis," Current Opinion in Electrochemistry, vol. 37, Art. no. 101178, 2023.

[23] X. Wu, Y. Chen, and Y. Ma, "Research progress of solid oxide electrolysis cell system: dynamic modeling and control," Renewable and Sustainable Energy Reviews, vol. 225, 116166, 2026.

[24] Y. Du et al., "The development of solid oxide electrolysis cells: Critical materials, technologies and prospects," Journal of Power Sources, vol. 607, Art. no. 234608, 2024.

[25] S. Sebbahi et al., "A comprehensive review of recent advances in alkaline water electrolysis for hydrogen production," International Journal of Hydrogen Energy, vol. 82, pp. 583–599, 2024.

[26] Y. Zheng, Y. Jiao, A. Vasileff, and S. Z. Qiao, "The hydrogen evolution reaction in alkaline solution: from theory, single crystal models, to practical electrocatalysts," Angewandte Chemie International Edition, vol. 57, no. 26, pp. 7568–7579, 2018.

[27] J. Wang, F. Xu, H. Jin, Y. Chen, and Y. Wang, "Non-noble metal-based carbon composites in hydrogen evolution reaction: Fundamentals to applications," Advanced Materials, vol. 29, no. 14, Art. no. 1605838, 2017.

[28] T. Reier, H. N. Nong, D. Teschner, R. Schlögl, and P. Strasser, "Electrocatalytic oxygen evolution reaction in acidic environments – Reaction mechanisms and catalysts," Advanced Energy Materials, vol. 7, no. 1, Art. no. 1601275, 2017.

[29] E. Liu et al., "Unifying the hydrogen evolution and oxidation reactions kinetics in base by identifying the catalytic roles of hydroxyl-water-cation adducts," Journal of the American Chemical Society, vol. 141, no. 7, pp. 3232–3239, 2019.

[30] H. Tüysüz, "Alkaline water electrolysis for green hydrogen production," Accounts of Chemical Research, vol. 57, no. 4, pp. 558–567, 2024.

[31] E. Fabbri, A. Habereder, K. Waltar, R. Kötz, and T. J. Schmidt, "Developments and perspectives of oxide-based catalysts for the oxygen evolution reaction," Catalysis Science & Technology, vol. 4, no. 11, pp. 3800–3821, 2014.

[32] X. Zhang and A. Bieberle-Hütter, "Modeling and simulations in photoelectrochemical water oxidation: from single level to multiscale modeling," ChemSusChem, vol. 9, no. 11, pp. 1223–1242, 2016.

[33] J. K. Nørskov et al., "Origin of the overpotential for oxygen reduction at a fuel-cell cathode," The Journal of Physical Chemistry B, vol. 108, no. 46, pp. 17886–17892, 2004.

[34] J. Rossmeisl, Z. W. Qu, H. Zhu, G. J. Kroes, and J. K. Nørskov, "Electrolysis of water on oxide surfaces," Journal of Electroanalytical Chemistry, vol. 607, no. 1–2, pp. 83–89, 2007.

[35] N. Zhang and Y. Chai, "Lattice oxygen redox chemistry in solid-state electrocatalysts for water oxidation," Energy & Environmental Science, vol. 14, no. 9, pp. 4647–4671, 2021.

[36] Z. F. Huang et al., "Chemical and structural origin of lattice oxygen oxidation in Co–Zn oxyhydroxide oxygen evolution electrocatalysts," Nature Energy, vol. 4, no. 4, pp. 329–338, 2019.

[37] Z. Y. Yu et al., "Clean and affordable hydrogen fuel from alkaline water splitting: past, recent progress, and future prospects," Advanced Materials, vol. 33, no. 31, Art. no. 2007100, 2021.

[38] N. Guillet and P. Millet, "Alkaline water electrolysis," in Hydrogen Production: Electrolysis, pp. 117–166, 2015.

[39] J. Hou and M. Yang, Green Hydrogen Production by Water Electrolysis. Taylor & Francis, 2024, p. 362.

[40] B. Lee et al., "Integrative techno-economic and environmental assessment for green H_2 production by alkaline water electrolysis based on experimental data," Journal of Environmental Chemical Engineering, vol. 9, no. 6, Art. no. 106349, 2021.

[41] L. Deng et al., "Bubble evolution dynamics in alkaline water electrolysis," eScience, Art. no. 100353, 2024.

[42] F. Gambou, D. Guilbert, M. Zasadzinski, and H. Rafaralahy, "A comprehensive survey of alkaline electrolyzer modeling: electrical domain and specific electrolyte conductivity," Energies, vol. 15, no. 9, Art. no. 3452, 2022.

[43] M. Bodner, A. Hofer, and V. Hacker, "H_2 generation from alkaline electrolyzer," Wiley Interdisciplinary Reviews: Energy and Environment, vol. 4, no. 4, pp. 365–381, 2015.

[44] A. S. Emam, M. O. Hamdan, B. A. Abu-Nabah, and E. Elnajjar, "A review on recent trends, challenges, and innovations in alkaline water electrolysis," International Journal of Hydrogen Energy, vol. 64, pp. 599–625, 2024.

[45] S. Dash, A. Singh, S. K. Surapraraju, and S. K. Natarajan, "Advances in green hydrogen production through alkaline water electrolysis: A comprehensive review," International Journal of Hydrogen Energy, vol. 83, pp. 614–629, 2024.

[46] B. V. Tilak, A. C. Ramamurthy, and B. E. Conway, "High performance electrode materials for the hydrogen evolution reaction from alkaline media," Proceedings of the Indian Academy of Sciences – Chemical Sciences, vol. 97, no. 3, 1986, pp. 359–393. New Delhi: Springer India.

[47] Y. Zhang et al., "High-efficiency and stable alloyed nickel-based electrodes for hydrogen evolution by seawater splitting," Journal of Alloys and Compounds, vol. 732, pp. 248–256, 2018.

[48] S. R. Ede and Z. Luo, "Tuning the intrinsic catalytic activities of oxygen-evolution catalysts by doping: a comprehensive review," Journal of Materials Chemistry A, vol. 9, no. 36, pp. 20131–20163, 2021.

[49] D. Zhou et al., "Recent advances in non-precious metal-based electrodes for alkaline water electrolysis," ChemNanoMat, vol. 6, no. 3, pp. 336–355, 2020.

[50] D. M. F. Santos, C. A. C. Sequeira, D. Macciò, A. Saccone, and J. L. Figueiredo, "Platinum–rare earth electrodes for hydrogen evolution in alkaline water electrolysis," International Journal of Hydrogen Energy, vol. 38, no. 8, pp. 3137–3145, 2013.

[51] T. Tang et al., "Synergistic electrocatalysts for alkaline hydrogen oxidation and evolution reactions," Advanced Functional Materials, vol. 32, no. 2, Art. no. 2107479, 2022.

[52] R. R. Raja Sulaiman, W. Y. Wong, and K. S. Loh, "Recent developments on transition metal-based electrocatalysts for application in anion exchange membrane water electrolysis," International Journal of Energy Research, vol. 46, no. 3, pp. 2241–2276, 2022.

[53] Y. Li et al., "Progress on the design of electrocatalysts for large-current hydrogen production by tuning thermodynamic and kinetic factors," Advanced Functional Materials, vol. 34, no. 28, Art. no. 2316296, 2024.

[54] H. Michishita et al., "Cathodic performance of $La_{0.6}Sr_{0.4}CoO_3$ perovskite oxide for platinum-free alkaline water electrolysis cell," Journal of the Electrochemical Society, vol. 155, no. 9, p. B969, 2008.

[55] D. D. Matienzo, T. Kutlusoy, S. Divanis, C. Di Bari, and E. Instuli, "Benchmarking perovskite electrocatalysts' OER activity as candidate materials for industrial alkaline water electrolysis," Catalysts, vol. 10, no. 12, Art. no. 1387, 2020.

[56] F. Ganci et al., "Nanostructured Ni based anode and cathode for alkaline water electrolyzers," Energies, vol. 12, no. 19, Art. no. 3669, 2019.

[57] F. Ganci, S. Lombardo, C. Sunseri, and R. Inguanta, "Nanostructured electrodes for hydrogen production in alkaline electrolyzer," Renewable Energy, vol. 123, pp. 117–124, 2018.

[58] X. Li, X. Hao, A. Abudula, and G. Guan, "Nanostructured catalysts for electrochemical water splitting: current state and prospects," Journal of Materials Chemistry A, vol. 4, no. 31, pp. 11973–12000, 2016.

[59] A. Kong et al., "Robust $Pt/TiO_2/Ni(OH)_2$ nanosheet arrays enable outstanding performance for high current density alkaline water electrolysis," Applied Catalysis B: Environmental, vol. 316, Art. no. 121654, 2022.

[60] C. Liu, F. Yang, A. Schechter, and L. Feng, "Recent progress of Ni-based catalysts for methanol electrooxidation reaction in alkaline media," Advanced Sensor and Energy Materials, vol. 2, no. 2, Art. no. 100055, 2023.

[61] J. Brauns and T. Turek, "Alkaline water electrolysis powered by renewable energy: A review," Processes, vol. 8, no. 2, Art. no. 248, 2020.

[62] F. Gambou, D. Guilbert, M. Zasadzinski, and H. Rafaralahy, "A comprehensive survey of alkaline electrolyzer modeling: electrical domain and specific electrolyte conductivity," Energies, vol. 15, no. 9, Art. no. 3452, 2022.

[63] F. Razmjooei et al., "Elucidating the performance limitations of alkaline electrolyte membrane electrolysis: dominance of anion concentration in membrane electrode assembly," ChemElectroChem, vol. 7, no. 19, pp. 3951–3960, 2020.

[64] A. Alashkar, A. H. Alami, and M. Mahmoud, "Advancements in electrolyzer materials for green hydrogen production," 2025.

[65] C. A. C. Sequeira, D. P. Cardoso, L. Amaral, B. Šljukić, and D. M. F. Santos, "Corrosion-resistant materials for alkaline water electrolyzers," Corrosion, vol. 76, no. 12, pp. 1155–1176, 2020.

[66] K. Zeng and D. Zhang, "Recent progress in alkaline water electrolysis for hydrogen production and applications," Progress in Energy and Combustion Science, vol. 36, no. 3, pp. 307–326, 2010.

[67] K. Scott, Ed., Electrochemical Methods for Hydrogen Production. Royal Society of Chemistry, 2019, pp. 28–58.

[68] M. F. Ali et al., "Zirconia toughened alumina-based separator membrane for advanced alkaline water electrolyzer," Polymers, vol. 14, no. 6, Art. no. 1173, 2022.

[69] M. Paidar, V. Fateev, and K. Bouzek, "Membrane electrolysis — History, current status and perspective," Electrochimica Acta, vol. 209, pp. 737–756, 2016.

[70] D. Henkensmeier et al., "Separators and membranes for advanced alkaline water electrolysis," Chemical Reviews, vol. 124, no. 10, pp. 6393–6443, 2024.

[71] Y. S. K. De Silva, P. H. Middleton, and M. L. Kolhe, "Performance comparison of mono-polar and bi-polar configurations of alkaline electrolysis stack through 3-D modelling and experimental fabrication," Renewable Energy, vol. 149, pp. 760–772, 2020.

[72] R. Phillips and C. W. Dunnill, "Zero gap alkaline electrolysis cell design for renewable energy storage as hydrogen gas," RSC Advances, vol. 6, no. 102, pp. 100643–100651, 2016.

[73] J. W. Haverkort and H. Rajaei, "Voltage losses in zero-gap alkaline water electrolysis," Journal of Power Sources, vol. 497, Art. no. 229864, 2021.

[74] M. T. De Groot, J. Kraakman, and R. L. G. Barros, "Optimal operating parameters for advanced alkaline water electrolysis," International Journal of Hydrogen Energy, vol. 47, no. 82, pp. 34773–34783, 2022.

[75] Z. Ren, J. Wang, Z. Yu, C. Zhang, S. Gao, and P. Wang, "Experimental studies and modeling of a 250-kW alkaline water electrolyzer for hydrogen production," Journal of Power Sources, vol. 544, Art. no. 231886, 2022.

[76] Z. Abdin, C. J. Webb, and E. M. Gray, "Modelling and simulation of an alkaline electrolyser cell," Energy, vol. 138, pp. 316–331, 2017.

[77] V. V. Solovey et al., "Development of high pressure membraneless alkaline electrolyzer," International Journal of Hydrogen Energy, vol. 47, no. 11, pp. 6975–6985, 2022.

[78] C. Valderrama, "High-temperature electrolysis," in Encyclopedia of Membranes (pp. 1–3). Berlin, Heidelberg: Springer, 2015.

[79] N. P. Sakkas, F. Gillung, K. Thummar, R. Abang, and L. Röntzsch, "Advanced pressurized alkaline water electrolysis at high temperatures up to 130 °C," International Journal of Hydrogen Energy, vol. 149, Art. no. 150075, 2025.

[80] F. Xiao et al., "Aligned porous nickel electrodes fabricated via ice templating with submicron particles for hydrogen evolution in alkaline water electrolysis," Journal of Power Sources, vol. 556, Art. no. 232441, 2023.

[81] Y. Chen, J. Liu, and L. Feng, "Transient analysis of a green hydrogen production and storage system using alkaline electrolyzer," Fuel, vol. 324, Art. no. 124752, 2022.

[82] L. Yang et al., "Recent progress of enhanced bubble separation in alkaline water electrolyzer," 2023.

[83] K. C. Sandeep et al., "Experimental studies and modeling of advanced alkaline water electrolyser with porous nickel electrodes for hydrogen production," International Journal of Hydrogen Energy, vol. 42, no. 17, pp. 12094–12103, 2017.

[84] M. M. Bakker and D. A. Vermaas, "Gas bubble removal in alkaline water electrolysis with utilization of pressure swings," Electrochimica Acta, vol. 319, pp. 148–157, 2019.

[85] V. Kienzlen, D. Haaf, and W. Schnurnberger, "Location of hydrogen gas evolution on perforated plate electrodes in zero gap cells," International Journal of Hydrogen Energy, vol. 19, no. 9, pp. 729–732, 1994.

[86] S. Ding et al., "Analysis of the effect of characteristic parameters and operating conditions on exergy efficiency of alkaline water electrolyzer," Journal of Power Sources, vol. 537, Art. no. 231532, 2022.

[87] M. Dreoni et al., "Alkaline electrolysis CFD modeling and application: A novel expression for a volume fraction-dependent current density," in Proceedings of the 37th International Conference on Efficiency, Cost, Optimization, Simulation and Environmental Impact of Energy Systems (ECOS), Rhodes, Greece, vol. 30, Jun. 2024.

[88] D. L. Martinho and T. Berning, "A conceptual approach to reduce the product gas crossover in alkaline electrolyzers," Membranes, vol. 15, no. 7, Art. no. 206, 2025.

[89] P. Trinke et al., "Hydrogen crossover in PEM and alkaline water electrolysis: mechanisms, direct comparison and mitigation strategies," Journal of The Electrochemical Society, vol. 165, no. 7, p. F502, 2018.

[90] R. L. G. Barros, J. T. Kraakman, C. Sebregts, J. van der Schaaf, and M. T. de Groot, "Impact of an electrode–diaphragm gap on diffusive hydrogen crossover in alkaline water electrolysis," International Journal of Hydrogen Energy, vol. 49, pp. 886–896, 2024.

[91] X. Luo et al., "Porous PVA skin-covered thin Zirfon-type separator as a new approach boosting high-rate alkaline water electrolysis beyond 1000 hours' lifespan," eScience, vol. 4, no. 6, Art. no. 100290, 2024.

[92] H. Gao et al., "High-performance composite membranes: embedding yttria-stabilized zirconia in polyphenylene sulfide fabric for enhanced alkaline water electrolysis efficiency," Small, vol. 21, no. 1, Art. no. 2407008, 2025.

[93] S. Kim et al., "Highly selective porous separator with thin skin layer for alkaline water electrolysis," Journal of Power Sources, vol. 524, Art. no. 231059, 2022.

[94] H. I. In Lee et al., "The synthesis of a Zirfon-type porous separator with reduced gas crossover for alkaline electrolyzer," International Journal of Energy Research, vol. 44, no. 3, pp. 1875–1885, 2020.

[95] M. F. Ali et al., "Zirconia toughened alumina-based separator membrane for advanced alkaline water electrolyzer," Polymers, vol. 14, no. 6, Art. no. 1173, 2022.

[96] J. Rodríguez and E. Amores, "CFD modeling and experimental validation of an alkaline water electrolysis cell for hydrogen production," Processes, vol. 8, no. 12, Art. no. 1634, 2020.

[97] L. Xue, S. Song, W. Chen, B. Liu, and X. Wang, "Enhancing efficiency in alkaline electrolysis cells: optimizing flow channels through multiphase computational fluid dynamics modeling," Energies, vol. 17, no. 2, Art. no. 448, 2024.

[98] Y. C. Jiang et al., "Holistic dynamic modeling and simulation of alkaline water electrolysis systems based on heat current method," Energies, vol. 17, no. 23, Art. no. 6202, 2024.

[99] W. Zhao, M. R. Nielsen, M. Kjær, F. Iov, and S. M. Nielsen, "Grid integration of a 500 kW alkaline electrolyzer system for harmonic analysis and robust control," e-Prime – Advances in Electrical Engineering, Electronics and Energy, vol. 5, Art. no. 100217, 2023.

[100] M. O. Qays, I. Ahmad, D. Habibi, A. Aziz, and T. Mahmoud, "System strength shortfall challenges for renewable energy-based power systems: A review," Renewable and Sustainable Energy Reviews, vol. 183, Art. no. 113447, 2023.

[101] H. Lee et al., "Outlook of industrial-scale green hydrogen production via a hybrid system of alkaline water electrolysis and energy storage system based on seasonal solar radiation," Journal of Cleaner Production, vol. 377, Art. no. 134210, 2022.

[102] U. Remme, Global Hydrogen Review 2024. IEA: Paris, France, 2024.

[103] C. Gulli, B. Heid, J. Noffsinger, M. Waardenburg, and M. Wilthaner, Global Energy Perspective 2023: Hydrogen Outlook. McKinsey Energy Solutions, Jan. 10, 2024. [Online]. Available: https://www.mckinsey.com/industries/oil-and-gas/our-insights/global-energy-perspective-2023-hydrogen-outlook, Accessed: Oct. 2025.

[104] European Commission, Commission Delegated Regulation (EU) 2023/1184 (RFNBO additionality/temporal/geographical correlation), Feb. 10, 2023. [Online]. Available: https://energy.ec.europa.eu/publications/renewable-hydrogen-delegated-acts_en

[105] European Parliamentary Research Service (EPRS), "Decarbonised gases and hydrogen package: low-carbon hydrogen definition (≈ 3.38 kg CO_2e/kg H_2)," May 6, 2025; see also EWI (2024) explainer. [Online]. Available: https://www.europarl.europa.eu/thinktank/; https://www.ewi.uni-koeln.de/en/news/what-is-low-carbon-hydrogen/, Accessed: Oct. 2025.

[106] European Commission, "A Hydrogen Strategy for a Climate-Neutral Europe," COM(2020) 301, Jul. 8, 2020. [Online]. Available: https://energy.ec.europa.eu/system/files/2020-07/hydrogen_strategy.pdf

[107] European Commission, REPowerEU Plan (hydrogen targets: 10 Mt domestic + 10 Mt imports by 2030), May 18, 2022. [Online]. Available: https://commission.europa.eu/strategy-and-policy/priorities-2019-2024/repowereu_en

[108] T.C. Enerji ve Tabii Kaynaklar Bakanlığı, "Türkiye Ulusal Hidrojen Teknolojisi Stratejisi ve Yol Haritası," n.d. [Online]. Available: https://enerji.gov.tr/duyuru-detay?id=20316

[109] UAE Government, "National Hydrogen Strategy 2031," n.d. [Online]. Available: https://u.ae/en/about-the-uae/strategies-initiatives-and-awards/strategies-plans-and-visions/environment-and-energy/national-hydrogen-strategy

[110] Sultanate of Oman, Ministry of Energy and Minerals, "Hydrogen Oman (Hydrom) targets," n.d. [Online]. Available: https://hydrom.om/Media/Pdf/Oman-Green-Hydrogen-Strategy-2024.pdf

[111] Air Products / ACWA Power / NEOM, "NEOM Green Hydrogen project (≈ 600 t/day)," 2023–2024. [Online]. Available: https://www.airproducts.com/energy-transition/neom-green-hydrogen-complex; https://acwapower.com/en/projects/neom-green-hydrogen-project, Accessed: Oct. 2025.

[112] D. Kronkalns, L. Zemite, L. Jansons, and A. Backurs, "Pursuing Opportunity: A Multi-Dimensional Analysis of Green Hydrogen Production Technologies," Latvian Journal of Physics and Technical Sciences, vol. 62, no. 5, pp. 87–108, 2025.

[113] F. Rosner et al., "Green steel: design and cost analysis of hydrogen-based direct iron reduction," Energy & Environmental Science, vol. 16, no. 10, pp. 4121–4134, 2023.

[114] Ö. Özgün, I. Dirba, O. Gutfleisch, Y. Ma, and D. Raabe, "Green ironmaking at higher H_2 pressure: reduction kinetics and microstructure formation during hydrogen-based direct reduction of hematite pellets," Journal of Sustainable Metallurgy, vol. 10, no. 3, pp. 1127–1140, 2024.

[115] G. He, D. S. Mallapragada, A. Bose, C. F. Heuberger, and E. Gençer, "Hydrogen supply chain planning with flexible transmission and storage scheduling," IEEE Transactions on Sustainable Energy, vol. 12, no. 3, pp. 1730–1740, 2021.

[116] A. Król, M. Gajec, J. Holewa-Rataj, E. Kukulska-Zając, and M. Rataj, "Hydrogen purification technologies in the context of its utilization," Energies, vol. 17, no. 15, Art. no. 3794, 2024.

[117] S. R. Naqvi, S. A. A. Taqvi, W. H. Chen, and D. Juchelková, "Techno economic analysis for advanced methods of green hydrogen production," Current Opinion in Green and Sustainable Chemistry, vol. 48, Art. no. 100939, 2024.

[118] Q. He et al., "Supercapacitor-isolated water electrolysis for renewable energy storage," Chemical Engineering Journal, vol. 495, Art. no. 153461, 2024.

[119] M. Holst, S. Aschbrenner, T. Smolinka, C. Voglstätter, and G. Grimm, "Cost forecast for low-temperature electrolysis – Technology driven bottom-up prognosis for PEM and alkaline water electrolysis systems," Fraunhofer Institute for Solar Energy Systems ISE: Freiburg, Germany, 2021, p. 79.

[120] A. Buttler and H. Spliethoff, "Current status of water electrolysis for energy storage, grid balancing and sector coupling via power-to-gas and power-to-liquids: A review," Renewable and Sustainable Energy Reviews, vol. 82, pp. 2440–2454, 2018.

[121] N. Saravanan and G. Nagarajan, "An experimental investigation of hydrogen-enriched air induction in a diesel engine system," International Journal of Hydrogen Energy, vol. 33, no. 6, pp. 1769–1775, 2008.

[122] N. Saravanan and G. Nagarajan, "Performance and emission studies on port injection of hydrogen with varied flow rates with diesel as an ignition source," Applied Energy, vol. 87, no. 7, pp. 2218–2229, 2010.

[123] ISO, ISO 8178-1: Reciprocating internal combustion engines — Exhaust emission measurement — Part 1: Test-bed measurement systems of gaseous and particulate emissions, 2017.

[124] Q. Hassan, A. Z. Sameen, H. M. Salman, and M. Jaszczur, "Large-scale green hydrogen production via alkaline water electrolysis using solar and wind energy," International Journal of Hydrogen Energy, vol. 48, no. 88, pp. 34299–34315, 2023.

[125] Y. Xia, H. Cheng, H. He, and W. Wei, "Efficiency and consistency enhancement for alkaline electrolyzers driven by renewable energy sources," Communications Engineering, vol. 2, no. 1, Art. no. 22, 2023.

[126] O. Aguirre, M. David, O. Camacho, and C. Ocampo-Martinez, "Hydrogen production through electrolyzers as a key player in multi-energy systems," in Energy Systems Integration for Multi-Energy Systems: From Operation to Planning in the Green Energy Context, Cham: Springer Nature Switzerland, 2025, pp.343–360.

[127] C. Huang, Y. Zong, S. You, and C. Træholt, "Economic model predictive control for multi-energy system considering hydrogen-thermal-electric dynamics and waste heat recovery of MW-level alkaline electrolyzer," Energy Conversion and Management, vol. 265, Art. no. 115697, 2022.

[128] C. Huang, Y. Zong, S. You, and C. Træholt, "Optimal operation of multi-energy system integrated with an alkaline electrolyzer dynamic power-to-hydrogen & heat (P2H2) model," EnerarXiv, vol. 19, pp. 1–6, 2022.

[129] J. Wang, J. Wen, J. Wang, B. Yang, and L. Jiang, "Water electrolyzer operation scheduling for green hydrogen production: A review," Renewable and Sustainable Energy Reviews, vol. 203, Art. no. 114779, 2024.

[130] J. Gu et al., "Experimental studies on dynamic performance of 250-kW alkaline electrolytic system," Journal of Power Sources, vol. 592, Art. no. 233920, 2024.

[131] R. Cozzolino and G. Bella, "A review of electrolyzer-based systems providing grid ancillary services: current status, market, challenges and future directions," Frontiers in Energy Research, vol. 12, Art. no. 1358333, 2024.

[132] R. Jain, K. Nagasawa, S. Veda, and S. Sprik, "Grid ancillary services using electrolyzer-based power-to-gas systems with increasing renewable penetration," e-Prime – Advances in Electrical Engineering, Electronics and Energy, vol. 6, Art. no. 100308, 2023.

[133] S. Shanian and O. Savadogo, "Techno economic analysis of electrolytic hydrogen production by alkaline and PEM electrolyzers using MCDM methods," Discover Energy, vol. 4, no. 1, Art. no. 23, 2024.

[134] H. Song, Y. Kim, and H. Yang, "Design and optimization of an alkaline electrolysis system for small-scale hydropower integration," Energies, vol. 17, no. 1,Art.no.20,2023.

[135] U.S. Energy Information Administration. [Online]. Available: https://www.eia.gov/outlooks/aeo/electricity_generation/pdf/AEO2023_LCOE_report.pdf, Accessed: Oct. 2025.

[136] B. Hurtubia and E. Sauma, "Economic and environmental analysis of hydrogen production when complementing renewable energy generation with grid electricity," Applied Energy, vol. 304, Art. no. 117739, 2021.

[137] IMARC Group, Potassium Hydroxide (KOH) Pricing Trends, Forecast and Market Analysis. [Online]. Available: https://www.imarcgroup.com/potassium-hydroxide-pricing-report, Accessed: Oct. 2025.

[138] S. Krishnan et al., "Present and future cost of alkaline and PEM electrolyser stacks," International Journal of Hydrogen Energy, vol. 48, no. 83, pp. 32313–32330, 2023.

[139] Y. M. Acevedo, J. H. Prosser, J. M. Huya-Kouadio, K. R. McNamara, and B. D. James, Hydrogen Production Cost with Alkaline Electrolysis (No. DOE-SA-09629-1). Strategic Analysis, Inc., Arlington, VA, USA, 2023, 24 p.

[140] International Energy Agency, The Future of Hydrogen: Seizing Today's Opportunities. Paris: IEA, 2022. [Online]. Available: https://www.iea.org/reports/the-future-of-hydrogen, Accessed: Oct. 2025.

[141] A. Mayyas and M. Mann, "Manufacturing competitiveness analysis for hydrogen refueling stations and electrolyzers," DOE Hydrogen Fuel Cells Program, 2018.

[142] J. Proost, "State-of-the-art CAPEX data for water electrolysers, and their impact on renewable hydrogen price settings," International Journal of Hydrogen Energy, vol. 44, no. 9, pp. 4406–4413, 2019.

[143] S. M. Saba, M. Müller, M. Robinius, and D. Stolten, "The investment costs of electrolysis – A comparison of cost studies from the past 30 years," International Journal of Hydrogen Energy, vol. 43, no. 3, pp. 1209–1223, 2018.

[144] Clean Hydrogen Partnership, Levelised Cost of Hydrogen (LCOH) Calculator Manual. European Hydrogen Observatory, 2024. [Online]. Available: https://observatory.clean-hydrogen.europa.eu/sites/default/files/2024-06/Manual%20-%20Levelised%20Cost%20of%20Hydrogen%20%28LCOH%29%20Calculator.pdf

[145] M. R. Shaner, H. A. Atwater, N. S. Lewis, and E. W. McFarland, "A comparative technoeconomic analysis of renewable hydrogen production using solar energy," Energy & Environmental Science, vol. 9, no. 7, pp. 2354–2371, 2016.

[146] M. Yu, K. Wang, and H. Vredenburg, "Insights into low-carbon hydrogen production methods: green, blue and aqua hydrogen," International Journal of Hydrogen Energy, vol. 46, no. 41, pp. 21261–21273, 2021.

[147] R. S. El-Emam and I. Khamis, "International collaboration in the IAEA nuclear hydrogen production program for benchmarking of HEEP," International Journal of Hydrogen Energy, vol. 42, no. 6, pp. 3566–3571, 2017.

[148] H. Ozcan, R. S. El-Emam, S. Celik, and B. A. Horri, "Recent advances, challenges, and prospects of electrochemical water-splitting technologies for net-zero transition," Cleaner Chemical Engineering, vol. 8, Art. no. 100115, 2023.

[149] P. Zhu, M. Mae, and R. Matsuhashi, "Techno-economic analysis of grid-connected hydrogen production via water electrolysis," Energies, vol. 17, no. 7, Art. no. 1653, 2024.

[150] A. Al-Sharafi, A. Z. Sahin, T. Ayar, and B. S. Yilbas, "Techno-economic analysis and optimization of solar and wind energy systems for power generation and hydrogen production in Saudi Arabia," Renewable and Sustainable Energy Reviews, vol. 69, pp. 33–49, 2017.

[151] D. Kumar, C. Zhang, E. Holubnyak, and S. Demirkesen, "Integrated assessment of levelized costs of hydrogen production: evaluating renewable and fossil pathways with emission costs and tax incentives," International Journal of Hydrogen Energy, vol. 95, pp. 389–401, 2024.

[152] R. M. Habour, K. Y. Benyounis, and J. G. Carton, "Green hydrogen production from renewable sources for export," International Journal of Hydrogen Energy, vol. 128, pp. 760–770, 2025.

[153] Y. Tang and Y. Li, "Comparative analysis of the levelized cost of hydrogen production from fossil energy and renewable energy in China," Energy for Sustainable Development, vol. 83, Art. no. 101588, 2024.

[154] F. Hönig, G. D. Rupakula, D. Duque-Gonzalez, M. Ebert, and U. Blum, "Enhancing the levelized cost of hydrogen with the usage of the byproduct oxygen in a wastewater treatment plant," Energies, vol. 16, no. 12, Art. no. 4829, 2023.

[155] E. Curcio, "Techno-economic analysis of hydrogen production: costs, policies, and scalability in the transition to net-zero," International Journal of Hydrogen Energy, vol. 128, pp. 473–487, 2025.

[156] H. V. Ghadim, R. Canessa, J. Haas, and R. Peer, "Electrolyzer cost projections compared to actual market costs: a critical analysis," in 2023 IEEE PES Innovative Smart Grid Technologies – Asia (ISGT Asia), Nov. 2023, pp. 1–5. IEEE.

[157] E. Vartiainen et al., "True cost of solar hydrogen – Levelised cost of hydrogen in Europe 2021–2050," in Proceedings of the 38th European Photovoltaic Solar Energy Conference and Exhibition, 2021, pp. 1601–1607, ISBN: 3-936338-78-7.

[158] K. Gandhi, H. Apostoleris, and S. Sgouridis, "Catching the hydrogen train: economics-driven green hydrogen adoption potential in the United Arab Emirates," International Journal of Hydrogen Energy, vol. 47, no. 53, pp. 22285–22301, 2022.

[159] N. Gerloff, "Comparative Life-Cycle-Assessment analysis of three major water electrolysis technologies while applying various energy scenarios for a greener hydrogen production," Journal of Energy Storage, vol. 43, Art. no. 102759, 2021.

[160] A. C. Hoppe and C. Minke, "Reducing environmental impacts of water electrolysis systems by reuse and recycling: Life cycle assessment of a 5 MW alkaline water electrolysis plant," Energies, vol. 18, no. 4, Art. no. 796, 2025.

[161] J. C. Koj, P. Zapp, C. Wieland, K. Görner, and W. Kuckshinrichs, "Life cycle environmental impacts and costs of water electrolysis technologies for green hydrogen production in the future," Energy, Sustainability and Society, vol. 14, no. 1, Art. no. 64, 2024.

[162] M. David, C. Ocampo-Martínez, and R. Sánchez-Peña, "Advances in alkaline water electrolyzers: a review," Journal of Energy Storage, vol. 23, pp. 392–403, 2019.

[163] W. Ajeeb, P. Baptista, and R. C. Neto, "Life cycle analysis of hydrogen production by different alkaline electrolyser technologies sourced with renewable energy," Energy Conversion and Management, vol. 316, Art. no. 118840, 2024.

[164] S. G. Simoes et al., "Water availability and water usage solutions for electrolysis in hydrogen production," Journal of Cleaner Production, vol. 315, Art. no. 128124, 2021.

[165] Y. Li et al., "Improving the efficiency of seawater desalination and hydrogen production: challenges, strategies, and the future of seawater electrolysis," Desalination, vol. 609, Art. no. 118882, 2025.

[166] International Energy Agency (IEA), Global Hydrogen Review 2021. Paris: IEA,2021. [Online]. Available: https://iea.blob.core.windows.net/assets/3a2ed84c-9ea0-458c-9421-d166a9510bc0/GlobalHydrogenReview2021.pdf1adad

International Journal of Energy Horizon 02 (2025) 61-69

International Journal of Energy Horizon

journal homepage: https://dergipark.org.tr/tr/pub/ijeh

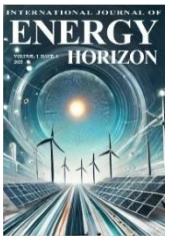

Research Article

Improvement of Haber–Bosch process for low carbon ammonia production through hybrid hydrogen recovery and energy recycling

Akın Doğan[1], Erhan Kayabasi[1,2,*]

[1] Karabuk University, Engineering Faculty, Mechanical Engineering Department 78050, Karabuk, Turkey
[2] Karabuk University, Iron and Steel Institute, Karabuk, Turkey
[1]ORCID No: 0009-0009-4564-9536
[2]ORCID No: 0000-0002-3603-6211

ARTICLE INFO

Article History:

Received:22 September 2025
Revised:7 October 2025
Accepted:2 November 2025
Available online:30 November 2025

Keywords:

Green ammonia
Haber–Bosch
Energy recovery
Hybrid hydrogen production

ABSTRACT

The energy-intensive nature of the Haber–Bosch process necessitates the development of self-sustaining synthesis systems. This study proposes a novel configuration integrating a hybrid hydrogen production method and a closed-loop energy recovery system to minimize external energy dependence and carbon emissions. Hydrogen is generated through the water–gas shift reaction using water molecules instead of natural gas, while the by-products carbon monoxide and carbon dioxide are reintegrated into the system to recover energy via turbine units. A detailed process simulation was conducted to evaluate the effects of temperature and pressure on ammonia yield and conversion rates. The results indicate that the optimal operating conditions (≈300°C, 30 bar) maximize both conversion efficiency and energy recovery, enabling the process to fully meet its energy demand internally. Compared to conventional systems, the proposed design reduces overall energy consumption and carbon footprint by transforming waste gases into usable electricity. The findings present a sustainable framework for green ammonia synthesis, emphasizing the significance of integrated hydrogen recovery and energy recycling.

1. INTRODUCTION

Global energy demand is projected to increase by approximately 80% by 2050, driven by rapid population growth and industrial expansion. This surge in energy consumption is directly linked to rising environmental pollution and the accelerated depletion of fossil fuel reserves. Consequently, the utilization of renewable energy sources has emerged as a critical factor in mitigating fossil fuel consumption and reducing environmental degradation [1]. As fossil fuel reserves continue to decline, the search for alternative and synthetic fuels has gained prominence, with ammonia emerging as a promising candidate. There are several key reasons why synthetically produced ammonia is considered a viable alternative fuel. Firstly, ammonia possesses a high energy density, making it an efficient energy storage and transportation medium [2]. Additionally, ammonia is one of the most widely used chemicals in the chemical industry, with its primary applications including agricultural fertilizers, refrigerants in cooling systems, cleaning products, and an alternative fuel for internal combustion engines [3].

Ammonia production has been predominantly based on the Haber-Bosch process, developed by Fritz Haber and Carl Bosch in the early 1900s, which marked the beginning of large-scale industrial ammonia synthesis. In terms of production volume, ammonia ranks as the second most-produced chemical worldwide, with an annual output of approximately 200 million tons. Notably, approximately 85% of ammonia production is allocated to the manufacturing of fertilizers such as urea, ammonium sulfate, and ammonium nitrate [4,5]. The Haber-Bosch process involves the reaction of gaseous nitrogen (N_2) and hydrogen (H_2) under high pressure (100–450 bar) and elevated temperatures (300–500°C) to synthesize ammonia [6]. Given these fundamental advantages, ammonia has recently garnered substantial international attention. The Haber-Bosch process involves the production of hydrogen through the utilization of hydrocarbons such as coal, natural gas, or naphtha, which is subsequently combined with nitrogen gas extracted from atmospheric air. Due to its high reactivity, ammonia serves as a fundamental building block in the synthesis of numerous nitrogen-containing

*Corresponding author
E-mail address: erhankayabasi@karabuk.edu.tr
journal homepage: https://dergipark.org.tr/tr/pub/ijeh

compounds [7]. However, current ammonia production processes result in the release of approximately 2.7 to 3.4 tons of carbon dioxide per ton of ammonia produced, primarily due to the use of natural gas or coal as carbon sources. Additionally, ammonia synthesis accounts for approximately 1–2% of global energy consumption [8]. In response to growing environmental concerns and the escalating effects of climate change, there has been an increasing interest in low-carbon ammonia production methods. One such approach, known as "green ammonia production," involves the electrolysis of water (H_2O) to obtain hydrogen, which is subsequently reacted with nitrogen using renewable energy sources [4]. Although green ammonia production is not a novel concept, it was historically employed in Norway from the late 1920s to the 1990s through the utilization of hydroelectric power for sustainable hydrogen production via the Atmospheric Electrolysis Cell (AEC) process [9]. Compared to conventional methods, this approach significantly reduces greenhouse gas emissions. In a study by Duncan A. Nowicki, a conceptual design was proposed for a small-scale green ammonia plant utilizing the Haber-Bosch cycle, in which hydrogen was produced via a solid oxide electrolyzer and nitrogen was purified from atmospheric air. The operational efficiency of the system was reported as 52.12%, yielding results comparable to those of the cryogenic air separation unit (ASU) reference system, which achieved an efficiency of 52.89%. The specific energy consumption for ammonia synthesis was documented as 9.94 kWh/kgNH_3. Despite these promising results, further improvements in system design remain necessary. For instance, optimizing heat integration by utilizing waste heat from oxygen pumps to supply the steam required for the electrolyzer could enhance overall system efficiency while simultaneously reducing energy consumption [10]. Another alternative, "blue ammonia," integrates fossil fuel-based ammonia production with carbon capture and storage (CCS) technologies. While this approach has the potential to significantly reduce carbon emissions, the process still involves components that contribute to considerable levels of emissions. Furthermore, both green and blue ammonia production methods present substantial technical and economic challenges, necessitating comprehensive evaluation and the development of alternative systems [7]. Blue ammonia has the potential to serve as a crucial tool in addressing the need to reduce carbon emissions. Most research on blue ammonia has primarily focused on advancing new reforming techniques aimed at minimizing CO_2 emissions [11]. One such example is the process designed by Martínez et al., which utilizes the oxidation properties of CaCu to enhance the efficiency of ammonia production while simultaneously reducing CO2 emissions through the formation of CaCO3 [12]. Gray ammonia production plays a significant role in wastewater management and the mitigation of environmental impacts. In this context, ammonia recovery and utilization can offer both economic and ecological benefits. However, due to its potential effects on air quality, ammonia must be carefully managed to align with environmental sustainability goals [13]. Research on gray ammonia primarily focuses on its environmental implications, as well as its industrial applications and possible recovery methods. Advancements in this field present significant opportunities for improving both energy efficiency and waste management [14]. Turquoise ammonia has emerged as a critical component in sustainable energy production and environmental management. Traditional ammonia production techniques, which rely on hydrogen derived from natural gas, result in significant carbon dioxide emissions. In contrast, turquoise ammonia is synthesized through the reaction of hydrogen with methane, a process designed to significantly reduce carbon emissions. This approach integrates carbon capture and storage (CCS), thereby minimizing its environmental footprint. Turquoise ammonia has various applications, including its use as a fertilizer in agriculture, as well as in transportation and energy storage. Additionally, wastewater treatment and bioenergy production represent essential aspects of this production method [15,16]. Given the limitations of green and blue ammonia production processes particularly regarding carbon emissions, electricity sources, and hydrogen supply, it is evident that several aspects require further development. This study investigates the potential for replacing these shortcomings with alternative resources and restructuring the production system accordingly. In this study, the mass and energy balance of an ammonia production process is analyzed, with the primary objectives of reducing the energy demand of the process, recovering mass flows within the system, and ultimately minimizing both energy losses and CO_2 emissions. By optimizing these parameters, the study aims to achieve the lowest possible energy and material consumption per unit of ammonia produced.

2. MATERIALS AND METHODS

The process simulation was developed in DWSIM. The water-gas shift reaction was modeled using an equilibrium reactor approach, based on the kinetics reported by [17], specifically utilizing the Langmuir-Hinshelwood type rate expression (Eq. 13). The ammonia synthesis reactor was modeled as a Plug-Flow Reactor (PFR) using the Temkin-Pyzhev kinetic model as implemented in DWSIM's built-in ammonia reactor module. The thermodynamic property package selected for the system was the Soave-Redlich-Kwong (SRK) equation of state, which is well-suited for high-pressure petrochemical and synthesis gas processes. The simulation convergence was achieved using the Boston-Britt inside-out method with a relative convergence tolerance of 1×10^{-6}.

The water-gas shift reaction is one of the most important methods used in the chemical industry for the production of pure hydrogen, particularly due to its efficiency and cost-effectiveness in large-scale applications such as ammonia synthesis. This process involves the reaction of carbon monoxide with steam, resulting in the formation of carbon dioxide and hydrogen.

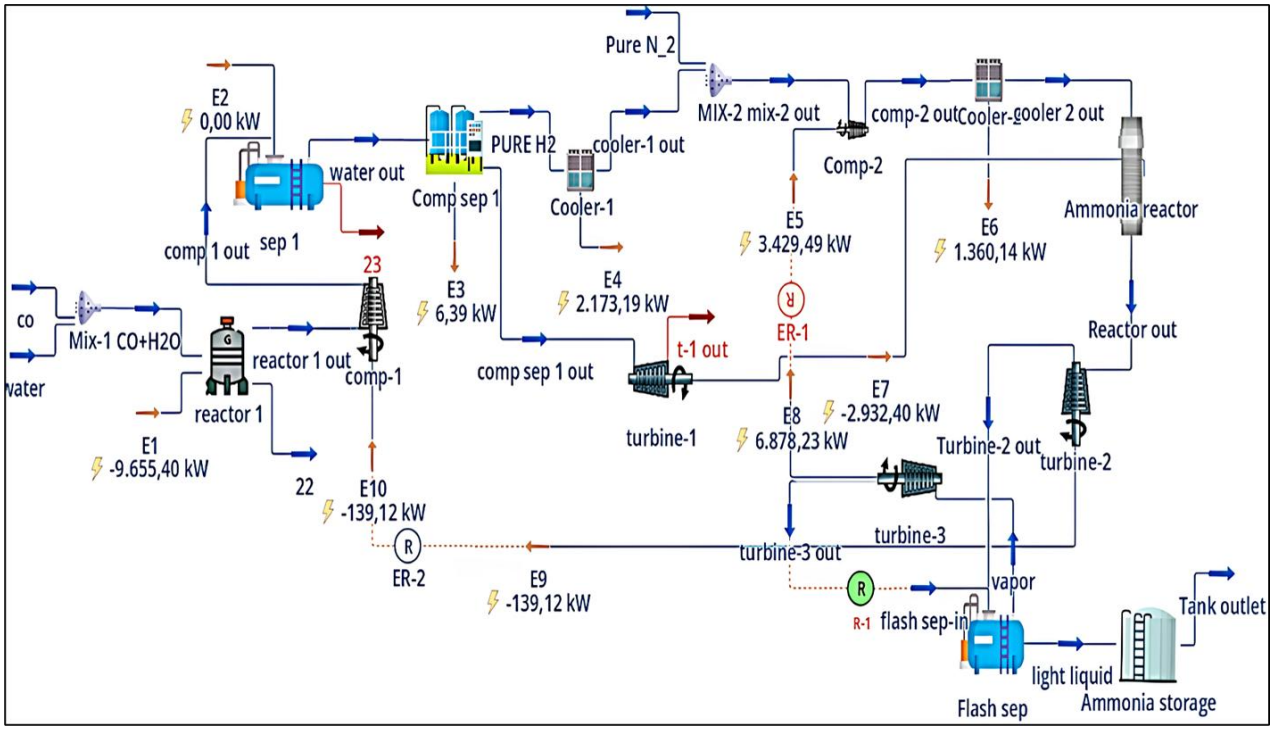

Figure 1. General layout of the proposed system.

The equilibrium reaction, with an equilibrium constant of 6.80 and a conversion rate of approximately 80%, plays a crucial role in hydrogen production. Initially, the steam and carbon monoxide flow rates are 100 mol/h and 25 mol/h, respectively. These reactants are mixed and sent to an equilibrium reactor, where they react in the vapor phase. Following the reaction, the vapor-phase products are directed to a compressor to reach the ideal operating pressure of 25 bar. The electrical energy required for the compressor is supplied by the system component named Turbine 3. The outlet stream is then directed to a separator, where 0.45 mol fraction of hydrogen is present in the vapor phase, while the liquid phase is discharged. The hydrogen stream is subsequently sent to a compound separation unit to obtain pure hydrogen, yielding approximately 1677 kmol/h of high-purity hydrogen. When the system component "Compound Separator 1" is utilized for hydrogen purification, it generates approximately 10.38 kWh of energy. The material stream discharged from the compound separation unit contains approximately 83% CO_2 and 16% CO at a pressure of 25 bar. Given its high pressure, this stream is utilized to generate the electrical energy required for the ammonia reactor. The outlet stream from the compound separator, referred to as "compound separator discharge," is directed to Turbine 2 to reduce its pressure from 25 bar to 0.05 bar. This pressure reduction process yields approximately 4.987 MW of energy. The water-gas shift reaction, which is employed for pure hydrogen production, demonstrates a high level of efficiency and effectiveness, with an approximately 80% conversion rate [17]. Composition of NG in this study is as follows: CH_4 90.3%, C_2H_6 6.6%, C_3H_8 2.2%, C_4H_{10} 0.9%. Steam reforming reactions of CH_4 and the other C_nH_m hydrocarbons are represented by Eq.'s (1) and (2), respectively[18].

$$CH_4 + H_2O \leftrightarrow CO + 3H_2, \qquad \Delta H^0 = 206 \times 10^3 \frac{kJ}{kMol} \tag{1}$$

$$C_nH_m + nH_2O \leftrightarrow nCO + \left(n + \frac{m}{2}\right)H_2 \tag{2}$$

The development of a compact fuel reformer through process simulation and optimization necessitates accurate modeling of WGS reaction kinetics, which serve as a critical component. Numerous kinetic rate expressions have been proposed and examined to assess the water–gas shift reaction rate across different catalysts, as illustrated in Eq. (3)[18].

$$CO + H_2O \leftrightarrow CO_2 + H_2, \qquad \Delta H^0 = -41 \times 10^3\ kJ/kMol \tag{3}$$

The equilibrium relationship of reaction (1) and the corresponding temperature dependence of the equilibrium constant, K_{MSR} are expressed in Eqs. (4) and (5), respectively[18].

$$K_{msR} = \frac{y_{CO}y_{H_2}^3}{y_{cH_4}y_{H_{2O}}}P_t^2 \tag{4}$$

$$= 10^{\frac{-11650}{T(k)}+13.076} \tag{5}$$

Here, y denotes the mole fraction of a gaseous component, while P_t (bar) represents the total pressure of the reforming reaction. The equilibrium relationship for the WGS reaction (3) and the temperature dependence of the corresponding equilibrium constant, K_{WGS}, are defined as follows[18]:

$$K_{WGS} = \frac{y_{Co_2}y_{H_2}}{y_{CO}y_{H_2O}} \tag{6}$$

$$= 10^{\frac{1910}{T(K)}-1.784} \tag{7}$$

For a given temperature and pressure, the equilibrium conversion of CH_4 in the reaction (1) and the equilibrium reaction extent of the reaction (3) can be obtained by simultaneously solving the Eqs. (4) and (7) after replacing all the mole fraction terms with CH_4 conversion and WGS reaction extent according to each reaction stoichiometry. On the other hand, steam reforming conversions of the other C_2 hydrocarbons in the NGR are assumed as 100%. þ Heat of reaction in the reactions (1)e(3) including heats of combustion of NGB at temperature T(K) can be obtained as follows [18]:

$$\Delta H_r(T) = \Delta H_r^0 + \int_{298}^{T} \Delta C_p\, dT \tag{8}$$

where, ΔC_p can be calculated using the heat capacities of the species. As an instance, when 1 mole of C_nH_m is steam-reformed by reaction (2), ΔC_p is given by

$$\Delta C_p = \frac{n+m/2}{1}C_{p,H_2}\frac{n}{1}Cpc_0 - \frac{n}{1}c_{p,H_2O(g)} - C_{p,CnH_m} \tag{9}$$

Likewise, the difference of the standard enthalpy of formation, ΔH_r^0 can also be obtained using Eq. (9) by replacing Cp with ΔH^o. Stoichiometric amount of air needed for the combustion of NGB is calculated assuming complete combustion of NGB supplied to the burner. Actual feeding rate of combustion air is 1.1 times the stoichiometric amount. The flow rate and composition of CFG are also calculated using the stoichiometry. Combustion temperature (TBN) of NGB in the burner was assumed 300 C higher than the temperature (TSR) of steam reforming reaction in the catalyst bed. Most heat exchangers in Fig. 1 are installed to heat up NGR and WR using such hot gases as RFG and CFG. Particularly, HEX1 and HEX2 have a function to keep the temperatures of RFG entering HTS and LTS at 350 and 200 C, respectively. When hot and cold fluids flow counter-currently in a heat exchanger, the required heat transfer area, AHX, is calculated by [18]

$$A_{HX} = \frac{Q_{Hx}}{U\Delta T_{lm}} \tag{10}$$

where, Q_{HX} is a heat transfer rate (kJ/s), U is an overall heat transfer coefficient ($kJ/m^2/K/s$), and ΔT_{lm} is a logarithmic mean temperature difference (K):

$$\Delta T_{lm} = \frac{(T_{h,i}-T_{c,o})-(T_{h,o}-T_{c,i})}{\log\frac{T_{h,i}-T_{c,o}}{T_{h,o}-T_{c,i}}} \tag{11}$$

where, subscripts h and c indicate hot and cold fluids, respectively, and i and o indicate inlet and outlet positions of fluids in a heat exchanger. The process efficiency of hydrogen production was calculated using the low heating values (HLHV) of H_2 produced and NG consumed as follows[18]:

$$\eta = \frac{N_{H_2}H_{LHV,H_2}}{(N_{NGR}+N_{NGB})H_{LHV,NG}} \tag{12}$$

From the adsorptive mechanism, Langmuir–Hinshelwood type rate expressions can be derived. The following rate expression is derived from Yang–Hougen table when the surface reaction is assumed rate controlling [17]:

$$r_{CO} = k\frac{P_{H_2O}P_{CO}-P_{H_2}P_{CO_2}/K_P}{(1+K_1P_{CO}+K_2P_{H_2O}+K_3P_{CO_2}+K_4P_{H_2})^2} \tag{13}$$

For the redox mechanism an equation derived as following rate expression and confirmed its validity using Cu-Zn-Cr catalysts [17]:

$$r_{CO} = k\frac{P_{H_2O}P_{CO}-P_{H_2}P_{CO_2}/K_P}{AP_{H_2O}+P_{CO}} \tag{14}$$

Using a CuO/ZnO catalyst, another rate expression can be derived from the redox mechanism when a single path reaction model is assumed [17]:

$$r_{CO} = \frac{k_1k_2(P_{H_2O}P_{CO}-P_{H_2}P_{CO_2}/K_P)}{k_1P_{H_2O}+k_2P_{CO}+(k_{1\_}+k_{2\_})P_{CO_2}} \tag{15}$$

In contrast to those rate expressions from detailed reactions, mechanisms and rate determining steps, there are simple empirical rate expressions which do not consider any mechanism a simple reversible rate expression for CO conversion [17]:

$$r_{co} = k\left(P_{CO}P_{H_2O} - \frac{P_{CO_2}P_{H_2}}{K_P}\right) = kP_{CO}P_{H_2O}(1-\beta) \tag{16}$$

where

$$\beta = \frac{P_{CO_2}P_{H_2}}{P_{CO}P_{H_2O}K_{eq}} \tag{17}$$

Other research groups have reported that the water gas shift reaction is not a simple order reaction, especially at steam/CO ratios, and have tried to find proper exponent parameters in a power-law type equation [17]:

$$r_{CO} = kP_{co}^nP_{H_2O}^m(1-\beta) \tag{18}$$

From thermodynamic properties and relations, the equilibrium constant for the water gas shift reaction can be derived in a conventional way as shown in the following equation [17]:

$$\ln(K_{eq}) = \frac{5693.5}{T} + 1.077\ln T + 5.44\times10^{-4}T - 1.125\times10^{-7}T^2 - \frac{49170}{T^2} - 13.148 \tag{19}$$

where

$$K_{eq} \cong \frac{P_{CO_2}P_{H_2}}{P_{H_2O}P_{CO}} \tag{20}$$

a simpler equation for Keq is given as in Eq. (21):

$$K_{eq} = \exp\left(\frac{4577.8}{T} - 4.33\right) \tag{21}$$

Although the exothermic nature of the reaction suggests that lower temperatures would be advantageous, the specified temperature range provides an acceptable balance between ammonia yield and reaction kinetics. Even under these conditions, the conversion rate remains approximately 15–35% [10].

The pure hydrogen stream from the water-gas shift reactor is cooled to approximately 200°C in a heat exchanger (Cooler 1). The recovered thermal energy from this cooling process is integrated into the system's internal heat exchange network, reducing the overall heating demand. The hydrogen exiting Cooler 1 is then sent to Mixer 3, where it is combined with pure nitrogen sourced from the atmosphere. At the outlet of Mixer 3, the molar fractions of the gas stream are 0.77 for hydrogen and 0.23 for nitrogen. This gas stream is then fed into Compressor 2 to increase its pressure to the optimal level of 200 bar. The electrical power required for Compressor 2 is supplied by Turbine 3, which generates energy by reducing the pressure of high-pressure steam to the ideal operating pressure of 25 bar. The hydrogen-rich stream, after being pressurized in Compressor 2, is then sent to Cooler 1 to be adjusted to the appropriate reaction temperature (425°C). Due to the temperature difference, Cooler 1 also generates electrical energy. The cooled hydrogen is subsequently fed into the Ammonia Reactor, where the chemical reaction takes place to synthesize ammonia. The Ammonia Reactor's energy requirements are met through the electricity generated by expanding the high-pressure (25 bar) stream composed of 0.83 molar fraction CO_2 and 0.16 molar fraction CO from the Compound Separator to a lower pressure of 0.05 bar. The chemical reactions occurring within the ammonia reactor can be represented by the following formulas: The kinetic reactions are employed in Plug-Flow Reactors (PFRs) and Continuous-Stirred Tank Reactors (CSTRs). In these reactors, the relationship between molar concentration and reaction rate is expressed as follows:

$$\mathrm{FA} = \mathrm{FA}_0 + \int_0^V r_A dV \tag{23}$$

where FA is the molar flow of the A component and V is the reactor volume which forms a system of equations that must be solved using an ODE solver for each dV, since r_i depends on Ni. The reaction rate in the ammonia reactor is 0.004019 kmol/m³h, with conversion rates of 43.47% for hydrogen and 47.44% for nitrogen. At the reactor outlet, the material stream contains 55% hydrogen, 15% nitrogen, and 28% ammonia. To reach the optimal pressure level, this stream undergoes an expansion process in Turbine 2, where the pressure is reduced to 150 bar. This expansion generates electricity, which is subsequently utilized by the Energy Recycle Block to power Compressor 1, thereby reducing the overall energy costs of the system. The effluent from Turbine 2, still containing 55% hydrogen, 15% nitrogen, and 28% ammonia, is directed to the Flash Separator for separation of pure ammonia. At the Flash Separator outlet, a vapor-phase stream with a molar fraction of 0.95 is obtained. Given its high pressure, this vapor is sent to Turbine 3, where the pressure is lowered to 25 bar to facilitate energy recovery. The pressure drop in Turbine 3 generates electricity, which is reintegrated into the system to meet its power demands. To enhance ammonia production efficiency, the Turbine 3 outlet stream, containing residual hydrogen and ammonia, is recirculated back into the Flash Separator via the Recycle Block. This recycling process is essential for maximizing ammonia yield. Finally, the separated ammonia stream, free from hydrogen, nitrogen, methane, carbon dioxide, and carbon monoxide, is transferred to the Ammonia Storage Unit for further processing and utilization.

3. RESULT AND DISCUSSION

This graph illustrates the change in mass flow rate of pure nitrogen material stream with respect to pressure variation at different temperatures. For all temperature values, the mass flow rate increases as the pressure rises. However, beyond a pressure value of 30 bar, the slope of the curves decreases, indicating a reduced rate of increase. When examining different temperature values, it is observed that the mass flow rate increases as the temperature rises at a constant pressure. In other words, higher temperatures have an enhancing effect on mass flow rate. Between the pressure values of 30–35 bar, the mass flow rate reaches its maximum value, and the rate of increase diminishes after the 35 bar point. These findings suggest that temperature increase positively affects the mass flow rate, while pressure increase has a limiting effect beyond a certain threshold. The molar mass flow of ammonia according to the pressure increase was depicted in Fig. 2.

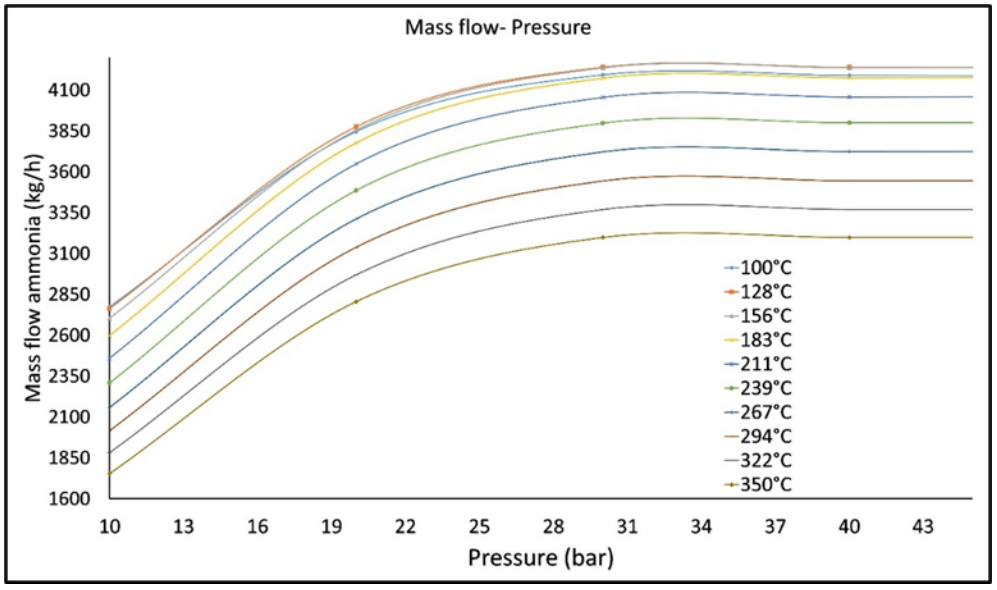

Figure 2. Molar mass flow of ammonia according to the pressure increase.

This graph presents a parametric study conducted to show the effect of increasing pressure values on the ammonia production efficiency of the system at different temperatures for pure nitrogen material flow. In all temperature values, the increase in pressure has a positive effect, boosting the efficiency; however, a pressure value of 30 bar represents the maximum point for most temperature curves. At pressure levels of 40-45 bar, the ammonia production efficiency stabilizes, showing a plateau across all temperature curves. Additionally, it is observed that as the temperature increases, the ammonia production efficiency also rises at the same pressure values. According to the parametric study, the system reaches its maximum efficiency at 322°C and 30 bar pressure. When examining all temperature values, it is evident that the 30 bar pressure ensures the maximum efficiency across all temperatures. In summary, efficiency improvement can be achieved with both temperature and pressure increases, but at higher pressures (above 30 bar), this effect becomes limited.

Figure 3 shows the mole fraction of ammonia (NH_3) formation as a function of pressure at different temperatures for pure nitrogen. It is generally observed that the ammonia mole fraction increases with the pressure value for each temperature. However, at a pressure value of 30 bar, it can be seen that the curves reach the maximum mole fraction value for most of the temperature conditions. Between 40-45 bar, all the curves flatten, indicating that the ammonia mole fraction stabilizes. Another result of the parametric study shows that, The observed decrease in ammonia mole fraction with increasing temperature, at a constant pressure, is a direct consequence of the exothermic nature of the ammonia synthesis reaction ($N_2 + 3H_2 \rightleftharpoons 2NH_3$, $\Delta H° = -92.4$ kJ/mol). According to Le Chatelier's principle, increasing the temperature shifts the equilibrium position towards the reactants, thereby lowering the equilibrium conversion and the resulting ammonia concentration. When examining the system at different temperature values, it is observed that the saturation value occurs at 30 bar. In conclusion, for optimum ammonia formation efficiency, lower temperatures should be preferred, and the pressure should not be increased beyond a certain level (approximately 30 bar).

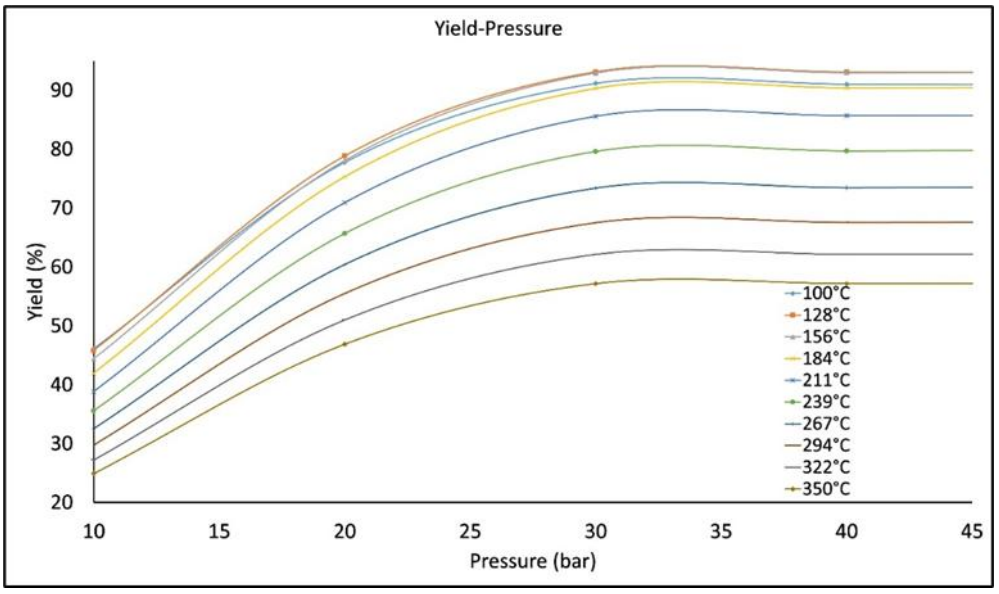

Figure 3. Yield versus reactor pressure under different reaction temperatures.

Figure 4 examines the relationship between temperature and ammonia mole fraction under different pressures (50, 90, and 100 bar). The data obtained shows a decreasing trend in the ammonia mole fraction as temperature increases. Especially at low temperature ranges (90°C-150°C), the mole fraction increases, and this trend continues up to approximately 150°C, after which it begins to decrease. As pressure increases, particularly at higher temperatures, it is observed that the rate of decrease in the ammonia mole fraction is relatively lower. This indicates the positive effect of pressure on the ammonia production reaction. Furthermore, for each pressure value in the graph, the maximum point of the ammonia mole fraction is observed to be between 130°C-150°C.

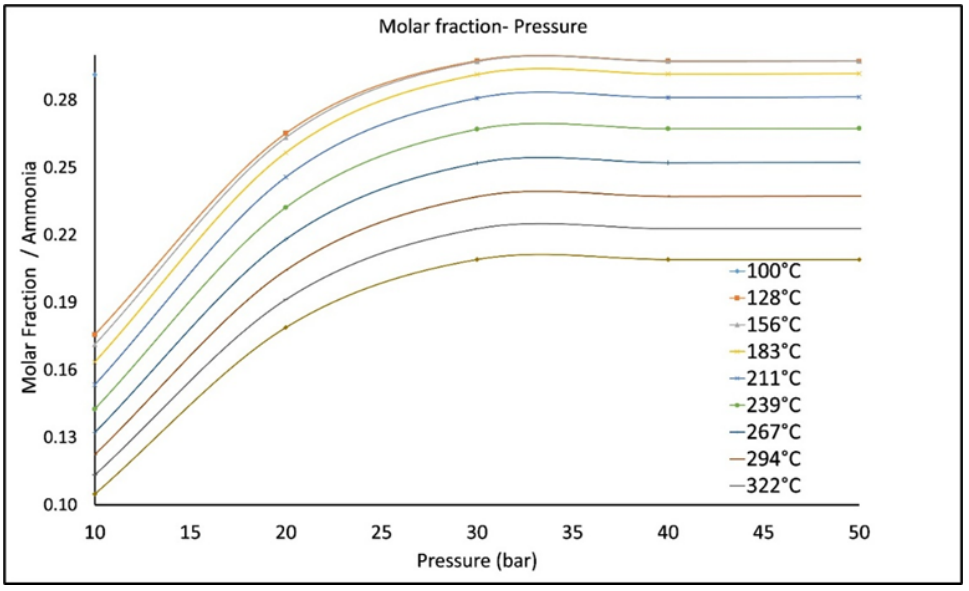

Figure 4. Molar fraction of ammonia under different reaction temperatures.

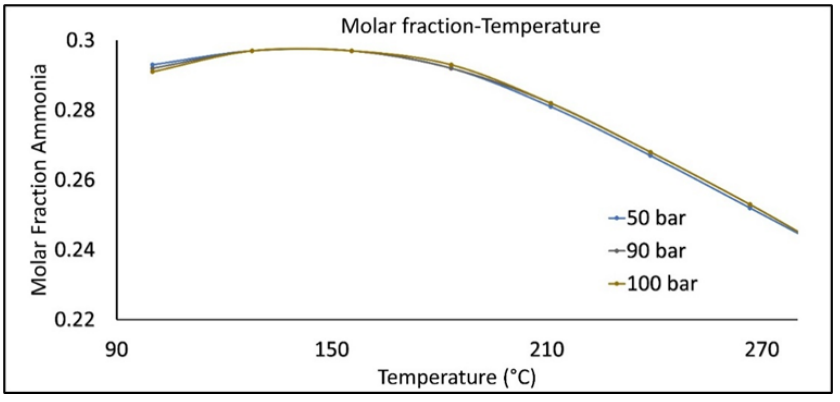

Figure 5. Molar fraction of ammonia for 50, 90 and 100 bar versus temperature increase.

In the Haber-Bosch process, the curves in Fig. 6 showing the effect of temperature changes on the hydrogen and nitrogen conversion rates during ammonia production indicates that temperature increases initially enhance the conversion rates of both gases. However, after a certain temperature, the conversion rates begin to decrease. As the temperature rises from 100°C to 300°C, the conversion rates for hydrogen and nitrogen reach 45% and 47.8%, respectively. The increase in conversion rates within this temperature range is due to the more favorable reaction kinetics under these conditions. However, when the temperature exceeds 200°C, a noticeable decrease in both hydrogen and nitrogen conversion rates is observed. This decline is attributed to the exothermic nature of the ammonia synthesis reaction, and according to Le Chatelier's Principle, the temperature increase shifts the system's equilibrium in the opposite direction, inhibiting ammonia formation. While higher temperatures accelerate the reaction kinetics, the thermodynamic equilibrium moves unfavorably towards ammonia decomposition, resulting in a decrease in conversion rates. The optimum temperature in the graph is identified around 300°C; however, in industrial applications, higher temperatures and pressures are preferred to increase reaction rates and efficiency. This situation highlights the complex interplay between kinetic and thermodynamic factors on ammonia production. Therefore, while ammonia formation is thermodynamically favored at lower temperatures, higher temperatures lead to the dominance of the reverse reaction, reducing the conversion rates of the gases.

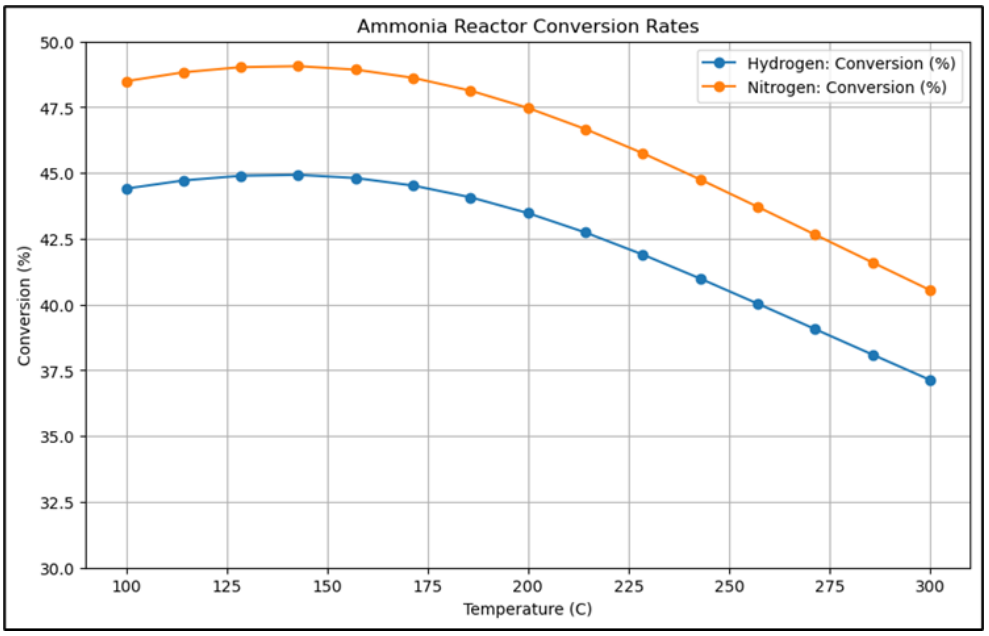

Figure 6. Ammonia conversion rates versus temperature

Fig. 7 examines the effect of pressure on hydrogen and nitrogen conversion rates during ammonia production in the Haber-Bosch process. Experimental data were obtained by measuring hydrogen and nitrogen conversion rates in the range of 0-50 bar. The conversion rate of hydrogen increases with pressure, starting at 10% and reaching 50% at 50 bar. The increase in hydrogen and nitrogen conversion rates with pressure is attributed to the decrease in the number of moles during the ammonia synthesis reaction. According to Le Chatelier's principle and the reaction equilibrium, higher pressures favor the forward reaction, leading to higher equilibrium conversions. Similarly, the conversion rate of nitrogen also increases with pressure, starting at 29% and reaching 45% at 50 bar. The conversion rate of nitrogen increases more rapidly at lower pressures, but the rate of increase slows down at higher pressures. The variation of hydrogen and nitrogen conversion rates with pressure emphasizes the importance of pressure control in the ammonia production process and highlights its role as a factor to consider in terms of energy efficiency. These findings suggest that pressure optimization in the ammonia production process could increase energy efficiency and reduce production costs. The data obtained can be used to improve energy efficiency and determine optimal operating conditions in industrial applications.

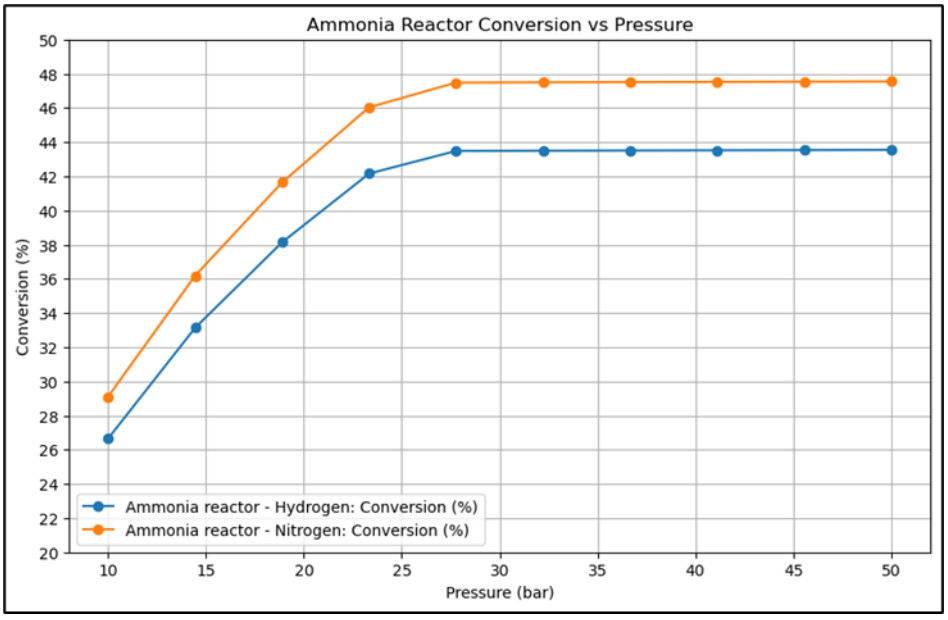

Figure 7. Ammonia reactor conversion versus pressure increase.

In Fig. 8, the relationship between temperature and ammonia yield (%) has been examined under various pressure values (40, 60, 80, and 100 bar). The data show that as temperature increases, the ammonia yield also increases, reaching a maximum at a specific temperature (145°C), after which the yield decreases as the temperature continues to rise. This behavior indicates that the highest yield values in the ammonia production process occur between 130°C and 150°C, marking the optimum temperature range. As pressure increases, relatively higher values of yield are observed, reflecting the positive effect of pressure on ammonia yield. However, even at high pressures, a decline in yield is observed when the temperature exceeds 150°C, indicating that excessive temperatures disrupt the reaction equilibrium. These results emphasize the importance of carefully selecting appropriate temperature and pressure conditions to achieve optimal ammonia yield and highlight the critical role of process parameters in production efficiency.

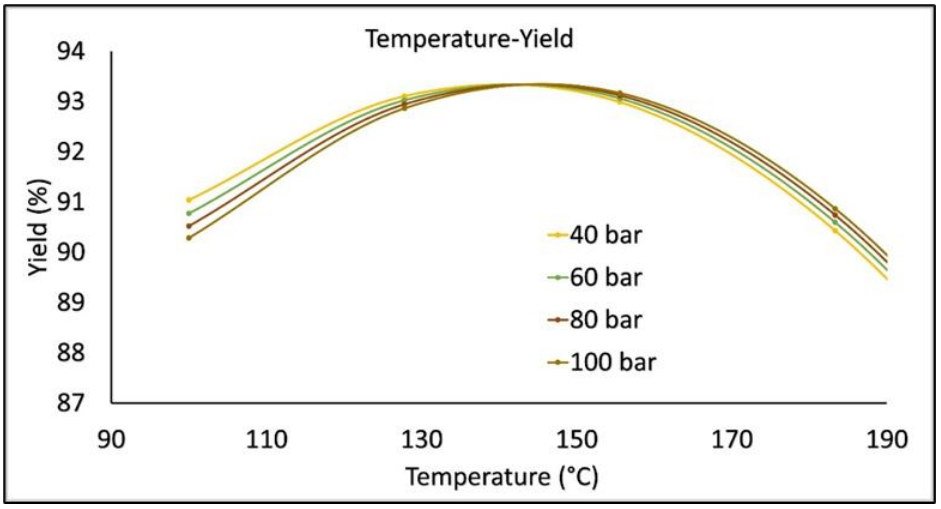

Figure 8. Yield of ammonia reactor under increasing temperatures with increasing pressures.

Upon examining the material flows in the table, it is observed that the output flow of the turbine named Turbine-3 contains hydrogen with a molar fraction of 99.8% in the vapor phase. Consequently, electrical energy is generated using the content values of the material flow named Turbine-3 Out, and this energy is recovered into the system to reduce the system's electrical energy requirement through a recovery method. Table 1 exhibits the mass temperature mass flow pressures and energy flow of the components in the whole system. T-1 Out, the output flow of the turbine named Turbine-1. This flow contains carbon monoxide with a molar fraction of 16.6% and carbon dioxide with a molar fraction of 83.3% in the vapor phase. To minimize environmental hazard, the pressure of this flow is reduced from 25 bar to 0.05 bar, and electrical energy is generated during the discharge process. This recovered energy is used to meet the electrical energy requirements of the element named PFRs (Ammonia Reactor).

Table 1. The parameters table of the simulation for each station.

Station	Mass Flow (kg/h)	Temperature (°C)	Pressure (bar)	Energy Flow (kW)
turbine-3 out	358,835	49.585	25	-161,064
flash sep-in	354,149	49.652	25	-159,658
vapor	358,835	85.586	87.5	-154,275
t-1 out	41,295.9	38.7701	0.05	-96,728.5
reactor 1 out	42,973.3	350	1.01	-95,707.2
comp sep 1 out	41,295.9	408.431	25	-91,741.9
water out	42,973.3	408.431	25	-89,127.4
comp 1 out	42,973.3	408.431	25	-89,127.4
CO+H2O	43,000	80.4529	1.01	-86,051.8
water	15,000	100	1.01	-55,357.6
co	28,000	25	1.01	-30,694.1
light liquid	4,107.08	172.09	87.5	-5,696.32
Tank outlet	4,107.08	172.09	87.5	-5,696.32
Turbine-2 out	8,792.73	250.518	150	313.146
Reactor out	87,92.73	425	200	20.4087
23	0	128.391	25	0
22	0	50	1.01	0
Pure N_2	7,115.4	200	25	357.892
cooler-1 out	1,677.33	200	25	1,180.95
mix-2 out	8,792.73	199.813	25	1,538.84
PURE H2	1,677.33	408.431	25	2,604.1
cooler 2 out	8,792.73	425	200	3,608.2
comp-2 out	8,792.73	573.718	200	4,968.34

Upon examining the energy consumption of the equipment within the system, in Table 2 it is notable that the element named Reactor 1 has a high energy consumption level (-9655.4 kW). However, this consumption is offset by the system's recovery methods, similar to how the energy needs of other equipment in the system are met. The energy requirements of system elements with high energy consumption, as discussed in the table, are addressed by using turbine elements within the system to expand material flows to the desired pressure. This expansion process also generates electrical energy, which is recovered to meet the system's energy needs.

Table 2. Energy balance of the system equipment.

Equipment	Type	Energy Consumption (-) / Generation (+) (kW)	MBR (kg/h)	EBR (kW)
Comp-2	Compressor	-6,788.81	0	-3,359.32
Comp-1	Compressor	-292.737	0	6,286.99

Flash Sep	Gas-Liquid Separator	-0.0291138	0.0207957	0.0291138
Ammonia storage	Tank	-4.28E-07	0	4.28E-07
Mix-2	Stream Mixer	4.86E-05	-3.20E-12	-4.86E-05
Mix-1	Stream Mixer	0.000699813	1.79E-10	-0.0006998
Compound Sep. 1	Compound Separator	10.3828	2.17E-10	4.00E-10
Turbine-2	Expander (Turbine)	292.737	0	-3.65E-07
Cooler-2	Cooler	1,360.14	0	1.28E-09
Cooler-1	Cooler	1,423.15	0	-8.54E-10
Ammonia reactor	Plug-Flow Reactor (PFR)	3,628.61	-5.72E-09	4.00E-08
Turbine-1	Expander (Turbine)	4,986.61	0	-8,615.22
Turbine-3	Expander (Turbine)	6,788.81	0	-0.0006232
Reactor 1	Gibbs Reactor	9,655.4	26,7317	-5.91E-08
Total Generation		11,775.42		
Total Consumption		-7,080.766		
NET BALANCE		4,694.654		

The reliability of the developed simulation model was verified by comparing the ammonia synthesis reactor performance with experimental data from the literature [10]. Figure 9 shows the comparison between simulated ammonia yields and experimental values across a temperature range of 250-400°C at constant pressure of 200 bar.

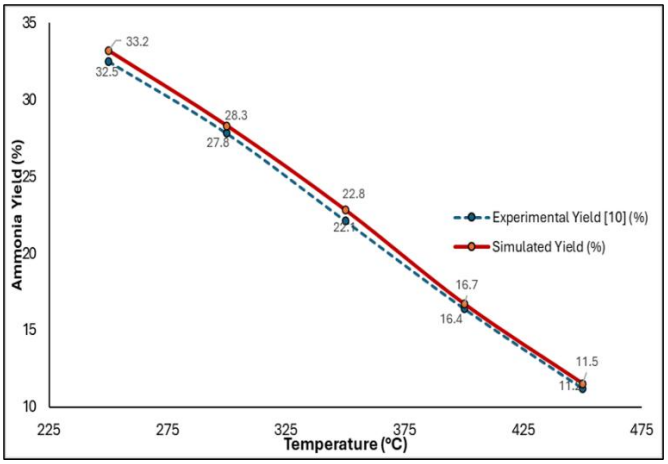

Figure 9. Model Validation: Ammonia Yield vs. Temperature

The close agreement between simulation results and experimental data, with an average relative error of 2.1%, demonstrates the accuracy of the Temkin-Pyzhev kinetic model implemented in DWSIM for ammonia synthesis. The maximum deviation observed was 3.4% at 350°C, which falls within acceptable limits for industrial process simulation.

4. CONCLUSION

In this study, the energy requirements of the Haber-Bosch process were met with an innovative energy recovery system, eliminating the need for an external energy source. Unlike traditional methods, the water-gas shift reaction was used to produce hydrogen from water molecules instead of natural gas. Carbon monoxide and carbon dioxide, which would otherwise be expelled as waste, were reintegrated into the process for recovery. The mass flow rates of unusable molecules were converted into electrical energy via turbines, enhancing the system's efficiency. Parametric studies were conducted to analyze the effects of temperature and pressure on yield and conversion rates in the ammonia reactor. These studies, illustrated with detailed graphs, highlighted the significant impact of temperature and mass flow on yield. The system was designed as a self-sustaining configuration that minimizes the environmental impact of harmful molecules by converting them into usable electrical energy. Compared to other systems, this design meets its energy needs through internal recovery and reduces the environmental carbon footprint by converting waste gases into electricity. In conclusion, this study introduces a sustainable and efficient framework for ammonia production, underscoring the critical role of integrated energy recovery and environmental stewardship in advancing green industrial processes.

REFERENCES

[1] M. Alsunousi and E. Kayabasi, "The role of hydrogen in synthetic fuel production strategies," Int. J. Hydrogen Energy, vol. 54, pp. 1169–1178, 2024. doi: 10.1016/j.ijhydene.2023.11.359.

[2] M. Klawitter, S. Wüthrich, P. Cartier, P. Albrecht, K. Herrmann, C. Gößnitzer et al., "Ammonia as a fuel: Optical investigation of turbulent flame propagation of NH_3/Air and $NH_3/H_2/N_2$/Air flames at engine conditions," Fuel, 2024. doi: 10.1016/j.fuel.2024.132616.

[3] N. Bora, A. Kumar Singh, P. Pal, U. Kumar Sahoo, D. Seth, D. Rathore et al., "Green ammonia production: Process technologies and challenges," Fuel, vol. 369, 2024. doi: 10.1016/j.fuel.2024.131808.

[4] A. G. Olabi, M. A. Abdelkareem, M. Al-Murisi, N. Shehata, A. H. Alami, A. Radwan et al., "Recent progress in Green Ammonia: Production, applications, assessment; barriers, and its role in achieving the sustainable development goals," Energy Convers. Manag., vol. 277, 2023. doi: 10.1016/j.enconman.2022.116594.

[5] M. J. Palys, H. Wang, Q. Zhang, and P. Daoutidis, "Renewable ammonia for sustainable energy and agriculture: vision and systems engineering opportunities," Curr. Opin. Chem. Eng., vol. 31, 2021. doi: 10.1016/j.coche.2020.100667.

[6] F. R. Bianchi and B. Bosio, "Modelling of green ammonia production based on solid oxide cells as electrolyser and oxygen separator for Haber-Bosch loop decarbonization," Int. J. Hydrogen Energy, 2024. doi: 10.1016/j.ijhydene.2024.07.047.

[7] P. Mayer, A. Ramirez, G. Pezzella, B. Winter, S. M. Sarathy, J. Gascon et al., "Blue and green ammonia production: A techno-economic and life cycle assessment perspective," iScience, vol. 26, 2023. doi: 10.1016/j.isci.2023.107389.

[8] M. Martín and A. Sánchez, "Biomass pathways to produce green ammonia and urea," Curr. Opin. Green Sustain. Chem., vol. 47, 2024. doi: 10.1016/j.cogsc.2024.100933.

[9] H. Nami, P. V. Hendriksen, and H. L. Frandsen, "Green ammonia production using current and emerging electrolysis technologies," Renew. Sustain. Energy Rev., vol. 199, p. 114517, 2024. doi: 10.1016/j.rser.2024.114517.

[10] D. A. Nowicki, G. D. Agnew, and J. T. S. Irvine, "Green ammonia production via the integration of a solid oxide electrolyser and a Haber-Bosch loop with a series of solid electrolyte oxygen pumps," Energy Convers. Manag., vol. 280, 2023. doi: 10.1016/j.enconman.2023.116816.

[11] A. F. Santos, "Natural Gas Production in the Brazilian Pre-Salt and Sustainable Development with the Generation of Blue Hydrogen and Blue Ammonia," presented at Day 3, Thu, October 26, 2023.

[12] I. Martínez, D. Armaroli, M. Gazzani, and M. C. Romano, "Integration of the Ca–Cu Process in Ammonia Production Plants," Ind. Eng. Chem. Res., vol. 56, pp. 2526–2539, 2017. doi: 10.1021/acs.iecr.6b04615.

[13] Z. Meng, X. Xu, W. Lin, B. Ge, Y. Xie, B. Song et al., "Role of ambient ammonia in particulate ammonium formation at a rural site in the North China Plain," Atmos. Chem. Phys., vol. 18, pp. 167–184, 2017.

[14] P. Li, Z. Jin, Z. Fang, and G. Yu, "A single-site iron catalyst with preoccupied active centers that achieves selective ammonia electrosynthesis from nitrate," Energy Environ. Sci., 2021.

[15] R. Lan, J. T. S. Irvine, and S. Tao, "Ammonia and related chemicals as potential indirect hydrogen storage materials," Int. J. Hydrogen Energy, vol. 37, pp. 1482–1494, 2012. doi: 10.1016/j.ijhydene.2011.10.004.

[16] V. Medina, H. Xiao, M. Owen-Jones, W. I. F. David, and P. J. Bowen, "Ammonia for power," Prog. Energy Combust. Sci., vol. 69, pp. 63–102, 2018. doi: 10.1016/j.pecs.2018.07.001.

[17] Y. Choi and H. G. Stenger, "Water gas shift reaction kinetics and reactor modeling for fuel cell grade hydrogen," J. Power Sources, vol. 124, pp. 432–439, 2003. doi: 10.1016/S0378-7753(03)00614-1.

[18] D. K. Lee, K. Y. Koo, D. J. Seo, and W. L. Yoon, "Analysis of design variables for an efficient natural gas steam reforming process comprised in a small scale hydrogen fueling station," Renew. Energy, vol. 42, pp. 234–242, 2012. doi: 10.1016/j.renene.2011.07.040.

International Journal of Energy Horizon 02 (2025) 70-79

International Journal of Energy Horizon

journal homepage: https://dergipark.org.tr/tr/pub/ijeh

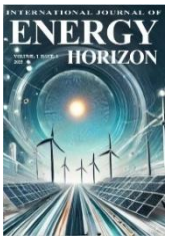

Research Article

Exergoeconomic evaluation of an S-CO_2 cycle coupled with a gas engine in a solid waste power plant

Alperen Tozlu[1,2,*], Marta Trninic[3], Emrah Özahi[4]

[1] Bayburt University, Vocational School of Technical Sciences, Electricity and Energy, Bayburt, Türkiye
[2] Toraighyrov University, Faculty of Energetics, Heat and Power Engineering Department, Pavlodar, Kazakhstan
[3] The Academy of Applied Studies Polytechnic, Serbia
[4] Gaziantep University, Mechanical Engineering Department, Gaziantep, Türkiye
[1]ORCID No: 0000-0002-2610-5279
[3]ORCID No: 0000-0001-6916-6162
[4]ORCID No: 0000-0003-3940-9500

ARTICLE INFO

Article History:

Received:10 October 2025
Revised:6 November 2025
Accepted:15 November 2025
Available online:30 November 2025

Keywords:

S-CO_2
Thermo-economy
Optimization
Genetic Algorithm
Waste-to-energy

ABSTRACT

In this study, the exhaust waste heat recovery from a gas engine of a municipal solid waste power plant (MSWPP) in Bayburt city, Turkey, through the application of a supercritical carbon dioxide (S-CO_2) cycle was investigated. The plant with an installed power capacity of 1450 kW, can be possible to generate an additional 108.65 kW of power by integrating the S-CO_2 system, corresponding to approximately 7.5% extra power production. A thermodynamic model was developed using actual data of the plant, enabling accurate assessment of system performance. The energetic and exergetic efficiencies of the developed cycle were determined in terms of energy transfer and exergy destruction values. Exergoeconomic analyses were also carried out using the Specific Exergy Costing (SPECO) method, providing cost allocation and investment insights for the plant components. The results reveal that the coupling of S-CO_2 cycle increases both the energy and exergy efficiencies, while also improving the overall economic performance. Consequently, the proposed system offers a sustainable and effective solution for the recovery of waste heat in solid waste-based power generation stations.

1. INTRODUCTION

Gas turbine power plants present considerable potential as a complementary technology to conventional power generation facilities and internal combustion (IC) gas engine power plants. Although gas turbines gained prominence during the 1950s and 1970s, they were subsequently eclipsed by open-cycle gas turbines due to their superior efficiency and higher firing temperatures. However, recent advancements in working fluid technologies have renewed interest in closed-cycle gas turbines, which are now being investigated as alternatives for power conversion systems [1]. Fundamentally, a gas turbine system operates on Brayton cycle to generate mechanical power. Gas turbines are categorized into open cycle (air), closed cycle (air or another medium), and also semi-open cycle configurations. Additionally, closed-cycle gas turbines are distinguished by the type of thermal source and working fluid employed. In the literature, fossil fuels, nuclear, solar, and biomass have been considered as heat sources, while air is a working fluid, supercritical CO_2 (S-CO_2), helium, nitrogen and other noble gases. Exhaust gases released from gas turbines and diesel engines represent low-temperature waste heat sources that, when treated as renewable-type energy inputs, offer substantial potential for meeting global energy demand [1–7]. Power cycles utilizing S-CO_2 have been identified and developed as effective methods due to conversion of low grade heat into useful energy potential. Notably, a waste heat recovery unit coupled with an S-CO_2 power cycle (capable of generating 8 MW) entered the electricity market for the first time in 2014, marking a milestone in this field [8]. Moreover, S-CO_2 power cycle applications are found in systems where closed-cycle gas turbines are integrated at the back end and in high-temperature fuel cell systems (e.g., sodium and helium reactors) [1, 9–11]. For instance, Ahmadi et al. [12] developed an S-CO_2 power cycle utilizing a typical geothermal heat reservior and designed a natural-gas liquefaction system powered by the waste heat of this cycle. In their study, the exergy efficiency of 20.5% and an annual electricity cost of USD 263,592 were found. Similarly, Akbari and

*Corresponding author
E-mail address: alperentozlu@bayburt.edu.tr
journal homepage: https://dergipark.org.tr/tr/pub/ijeh

Mahmoudi [13] proposed an S-CO_2 power cycle in which the thermal difference of the intercooler was harnessed as the evaporator of an organic Rankine cycle (ORC), thereby improving thermodynamic efficiency in the overall system. In another study, Kim et al. [14] analyzed nine different closed gas turbine cycles coupled to S-CO_2 in another landfill-gas-fired gas turbine plant. Their findings revealed that the recuperator played a more decisive role than the intercooler in enhancing thermal efficiency and total power generation. Nami et al. [15] proposed combining the waste heat of an open gas turbine cycle with an S-CO_2 closed gas turbine cycle, and subsequently using the remaining waste heat in an ORC system. Wang and Dai [16] designed two separate gas turbines employing transcritical CO_2 (T-CO_2) as the working fluid and dual heat exchangers to assess waste heat from a helium reactor. There are also many other studies that were carried out in this respect [17-21].

In the related study, an effective model is proposed to utilize the waste heat from a municipal solid waste into energy power plant located in Bayburt, Turkey, an operational facility generating electricity, to recover energy based on actual plant operating data. The proposed model underwent thermodynamic and thermoeconomic analyses [22]. Within the developed framework, waste heat was utilized as a thermal source in an S-CO_2 gas turbine cycle, thereby augmenting the power output of the existing facility. The primary novelty of this work lies in its status as the first study to evaluate waste heat recovery from an operational municipal solid waste-to-energy plant in Bayburt, with the objective of enhancing the plant's electricity generation capacity. Consequently, thermodynamic and thermoeconomic analyses were conducted to derive technical and economic performance indicators that could serve as benchmarks for system improvements. Cost assessments were performed using the well-known specific exergy cost (SPECO) method, which is grounded in 2nd law of thermodynamics. The exergetic costs of streams, subsystem exergy-destruction costs, and investment and operation-maintenance expenses were determined using cost-balance equations developed for each subsystem. Compared to conventional economic analyses that overlook system irreversibilities, the proposed exergy-based cost analysis offers a more rational approach by accounting for exergy destruction costs. Therefore, the proposed model and its associated thermodynamic and thermoeconomic evaluations are anticipated to be highly beneficial and practical for waste-heat recovery utilization and for enhancing the management of existing systems.

2. MATERIAL AND METHODOLOGY

2.1. Description of the Proposed System

The Bayburt Municipal Solid Waste Power Plant (BMSWPP) has been established in order to manage the solid-waste generated by Bayburt and its neighboring municipalities. This facility possesses a power capacity of 1.45 MW, which is produced using a gas engine. In the related study, a recompression supercritical carbon dioxide (S-CO2) gas turbine cycle was utilized and integrated as a model to augment the electrical output of the existing system by utilizing the plant's exhaust gas. Exhaust gas from the plant exhibited the temperature of 431 °C, the pressure of 1 bar and the mass flow rate of 2.181 kg/s. The newly developed system comprises gas-turbine (GT), a gas-turbine heat-exchanger (GTHE), low-pressure compressor (LPC), high-pressure compressor (HPC), precooler (PRE), recuperator (REC) and intercooler (INT).” should be changed as ‘’The newly developed system comprises a gas-turbine (GT), a gas-turbine heat-exchanger (GTHE), a low-pressure compressor (LPC), a high-pressure compressor (HPC), a precooler (PRE), a recuperator (REC), and an intercooler (INT). The main reason for naming it the ‘gas turbine heat exchanger’ is that the overall system is integrated with a gas turbine, and the heat exchanger’s primary role is to utilize the gas turbine’s exhaust gas as the main thermal input to drive the S-CO_2 cycle. Figure 1 presents a schematic layout of the system. The re-compression S-CO2 gas turbine cycle has been based on definition of the inlet conditions for the system's low-pressure compressor. At the inlet state of the low-pressure compressor, the temperature and pressure of S-CO2 (Pcrit= 73.8 bar and Tcrit=30.98 °C) were set at 40 °C and 85 bar, respectively, which exceed the critical values. To establish a feasible power cycle model, the CO2 pressure was constrained to 85–229.5 bar [15]. The pressure ratio (PR) between the compressors was determined to be 2.5 based on the CO2 pressure. The heat exchangers’ effectiveness (εf_{HE}) and the compressors’ and gas turbine’s isentropic efficiencies (η_C, η_{GT} , respectively, , respectively) have been assumed to be 0.85, 0.85, and 0.92, respectively, as is commonly reported in the literature [21-22]. Furthermore, the study was carried out under the general assumptions of a steady state operation, neglecting kinetic and potential energy changes, disregarding pressure losses in pipes and heat exchangers and being saturated liquid of the working fluid at the exit of the precooler and intercooler.

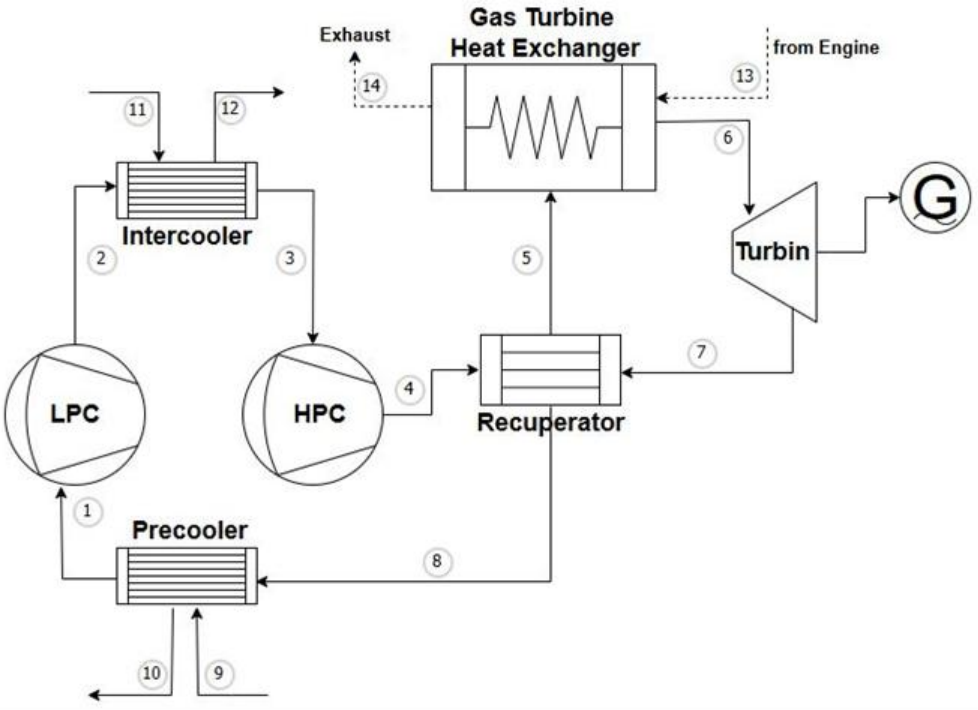

Figure 1. Schematic representation of the cycle

2.1. Thermodynamic And Thermoeconomic Analyses

By applying the related governing equations listed in Table 1, the heat transfer, work interaction, exergy destruction values, and exergy efficiencies of the subsystems were determined. In addition, the specific exergy of the flow and the corresponding exergy rate were found using the following relations [21-22];

$$\psi = (h - h_0) - T_0(s - s_0) \quad (1)$$

$$\dot{E}x = \dot{m}\psi \quad (2)$$

The energetic and exergetic efficiencies were determined using the following equations [21-22];

$$\eta = (\dot{W}_{GT} - (\dot{W}_{LPcomp} + \dot{W}_{HPcomp}))/\dot{m}_{exh}(h_{13} - h_{14}) \quad (3)$$

$$\varepsilon = (\dot{W}_{GT} - (\dot{W}_{LPcomp} + \dot{W}_{HPcomp}))/\dot{m}_{exh}(\psi_{13} - \psi_{14}) \quad (4)$$

Table 1. Schematic representation of the cycle

Gas Turbine Heat Exchanger	**Gas Turbine**
$\dot{m}_{13} = \dot{m}_{14} = \dot{m}_{exh}, \dot{m}_5 = \dot{m}_6 = \dot{m}_{CO_2}$	$\dot{m}_6 = \dot{m}_7 = \dot{m}_{CO_2}$
$\dot{m}_{exh}(h_{13} - h_{14}) = \dot{m}_{CO_2}(h_6 - h_5)$	$\dot{W}_{GT,a} = \dot{m}_{CO_2}(h_6 - h_7)$
$\dot{E}x_{D,GTHE} = \dot{m}_{exh}(\psi_{13} - \psi_{14}) - \dot{m}_{CO_2}(\psi_6 - \psi_5)$	$\dot{W}_{GT,s} = \dot{m}_{CO_2}(\psi_6 - \psi_7)$
$\varepsilon_{GTHE} = \frac{\dot{m}_{exh}(\psi_{13} - \psi_{14})}{\dot{m}_{CO_2}(\psi_6 - \psi_5)}$	$\dot{E}x_{D,GT} = \dot{W}_{GT,s} - \dot{W}_{GT,a}, \varepsilon_{GT} = \frac{\dot{W}_{GT,a}}{\dot{W}_{GT,s}}$
Recuperator	**Precooler**
$\dot{m}_4 = \dot{m}_5 = \dot{m}_7 = \dot{m}_8 = \dot{m}_{CO_2}$	$\dot{m}_9 = \dot{m}_{10} = \dot{m}_{wat}, \dot{m}_1 = \dot{m}_8 = \dot{m}_{CO_2}$
$(h_4 - h_5) = (h_8 - h_7)$	$\dot{m}_{CO_2}(h_8 - h_1) = \dot{m}_{wat}(h_{10} - h_9)$
$\dot{E}x_{D,REC} = \dot{m}_{CO_2}((\psi_4 - \psi_5) - (\psi_8 - \psi_7))$	$\dot{E}x_{D,PRE} = \dot{m}_{CO_2}(\psi_8 - \psi_1) - \dot{m}_{wat}(\psi_{10} - \psi_9)$
$\varepsilon_{REC} = \frac{(\psi_4 - \psi_5)}{(\psi_8 - \psi_7)}$	$\varepsilon_{PRE} = \frac{\dot{m}_{CO_2}(\psi_8 - \psi_1)}{\dot{m}_{wat}(\psi_{10} - \psi_9)}$
Low Pressure Compressor	**High Pressure Compressor**
$\dot{m}_1 = \dot{m}_2 = \dot{m}_{CO_2}$	$\dot{m}_3 = \dot{m}_4 = \dot{m}_{CO_2}$
$\dot{W}_{LPcomp,a} = \dot{m}_{CO_2}(h_2 - h_1)$	$\dot{W}_{HPcomp,a} = \dot{m}_{CO_2}(h_4 - h_3)$
$\dot{W}_{LPcomp,s} = \dot{m}_{CO_2}(\psi_2 - \psi_1)$	$\dot{W}_{HPcomp,s} = \dot{m}_{CO_2}(\psi_4 - \psi_3)$
$\dot{E}x_{D,LPcomp} = \dot{W}_{LPcomp,a} - \dot{W}_{LPcomp,s}, \varepsilon_{LPcomp} = \frac{\dot{W}_{LPcomp,s}}{\dot{W}_{LPcomp,a}}$	$\dot{E}x_{D,HPcomp} = \dot{W}_{HPcomp,a} - \dot{W}_{HPcomp,s}, \varepsilon_{HPcomp} = \frac{\dot{W}_{HPcomp,s}}{\dot{W}_{HPcomp,a}}$
Intercooler	
$\dot{m}_{11} = \dot{m}_{12} = \dot{m}_{wat}, \dot{m}_1 = \dot{m}_8 = \dot{m}_{CO_2}$	
$\dot{m}_{CO_2}(h_2 - h_3) = \dot{m}_{wat}(h_{12} - h_{11})$	
$\dot{E}x_{D,INT} = \dot{m}_{CO_2}(\psi_2 - \psi_3) - \dot{m}_{wat}(\psi_{12} - \psi_{11})$	
$\varepsilon_{INT} = \frac{\dot{m}_{CO_2}(\psi_2 - \psi_3)}{\dot{m}_{wat}(\psi_{11} - \psi_{12})}$	

Thermoeconomics refers to the integration of exergetic analyses in the frame of economical aspect, providing engineers and operators with insights into efficiency that cannot be satisfied with traditional energy analyses and standard economical assessments. In this study, the well-known SPECO method was utilized for analyses. Initially, all energy and exergy streams throughout the system were identified. Subsequently, each subsystem was characterized in terms of the fuel–product concept. In this framework, all exergy inputs into each relevant component were treated as fuel, while the corresponding exergy outputs were regarded as the product. Following the steps of the SPECO methodology, cost balance equations together with auxiliary relations were derived for every subsystem. These formulations are summarized and presented in Table 2.

Table 2. Thermoeconomic equations-of the cycle

Gas Turbine Heat Exchanger	**Gas Turbine**
$c_{13}\dot{E}x_{13} + c_5\dot{E}x_5 + \dot{Z}_{GTHE} = c_{14}\dot{E}x_{14} + c_6\dot{E}x_6$ $c_{13} = known, \frac{\dot{C}_{13}}{\dot{E}x_{13}} = \frac{\dot{C}_{14}}{\dot{E}x_{14}}$	$c_6\dot{E}x_6 + \dot{Z}_{GT} = c_{GT}\dot{W}_{GT} + c_7\dot{E}x_7$ $\frac{\dot{C}_6}{\dot{E}x_6} = \frac{\dot{C}_7}{\dot{E}x_7}$
Recuperator	**Precooler**
$c_4\dot{E}x_4 + c_7\dot{E}x_7 + \dot{Z}_{REC} = c_5\dot{E}x_5 + c_8\dot{E}x_8$ $\frac{\dot{C}_7}{\dot{E}x_7} = \frac{\dot{C}_8}{\dot{E}x_8}$	$c_8\dot{E}x_8 + c_9\dot{E}x_9 + \dot{Z}_{PRE} = c_1\dot{E}x_1 + c_{10}\dot{E}x_{10}$ $c_9 = 0, \frac{\dot{C}_1}{\dot{E}x_1} = \frac{\dot{C}_8}{\dot{E}x_8}$
Low Pressure Compressor	**High Pressure Compressor**
$c_{LPComp}\dot{W}_{LPcomp} + \dot{Z}_{LPcomp} = c_2\dot{E}x_2 - c_1\dot{E}x_1$ $\frac{\dot{C}_1}{\dot{E}x_1} = \frac{\dot{C}_2}{\dot{E}x_2}$	$c_{HPComp}\dot{W}_{HPcomp} + \dot{Z}_{HPcomp} = c_4\dot{E}x_4 - c_3\dot{E}x_3$
Intercooler	
$c_2\dot{E}x_2 + c_{11}\dot{E}x_{11} + \dot{Z}_{INT} = c_3\dot{E}x_3 + c_{12}\dot{E}x_{12}$ $c_{11} = 0, \frac{\dot{C}_2}{\dot{E}x_2} = \frac{\dot{C}_3}{\dot{E}x_3}$	

For each system component, indicates the total cost-rate, which covers capital investment (CI), operation and maintenance (OM) contributions. The corresponding capital cost rate is calculated using the expression below [21-22]:

$$\dot{Z} = (PEC * CRF * \phi)/(3600 * N) \quad (5)$$

Table 3 represents the economic constants.

Table 3. Economic constants

Total life time(n)	*30 years*
Annual operation time (N)	*8040 hours*
Interest rate (i)	*15%*
Maintenance factor (ψ)	*1.06*
Capital recovery factor (CRF)	$RF = \frac{i(1+i)^n}{(1+i)^n - 1}$

Exergoeconomic assessments require the formulation of cost relations for individual sub-components with respect to the system's investment costs. The investment expenditures of each unit were derived from their thermodynamic parameters. Table 4 [22] provides the mathematical functions corresponding to the capital investment costs of each component.

Table 4. Purchased equipment cost functions of the cycle

Gas Turbine Heat Exchanger	$PEC_{GTHE} = 2681(A_{GTHE})^{0.59}$
Gas Turbine	$PEC_{GT} = 4405(\dot{W}_{GT})^{0.7}$
Recuperator	$PEC_{REC} = 2681(A_{REC})^{0.59}$
Precooler	$PEC_{PRE} = 2143(A_{PRE})^{0.514}$
LP and HP Compressor	$PEC_{comp} = 71.1\left[\frac{\dot{m}_{CO_2}}{0.92 - \eta_c}\right](PR)(ln(PR)$
Intercooler	$PEC_{INT} = 2143(A_{INT})^{0.514}$

All heat exchangers within the GT cycle were taken as a shell-and-tube type, and their performance was modeled using Equation (6). For this purpose, the coefficients of overall heat transfer have been taken as 1.1, 0.7, and 2 for the gas-turbine heat-exchanger, the recuperator, and both the precooler and intercooler, respectively [22].

$$\dot{Q}_k = U_k A_k LMTD$$

Furthermore, Chemical Engineering Plant Cost Index, CEPCI was employed as a vital parameter for updating the plant costs. CEPCI is evaluated as the ratio of the cost index of the reference year to that of the original year [23-25]. Since the facility commenced operation in 2011, this year was selected as the reference point. The CEPCI values for 2011 and 2025 were considered as 585.7 and 800.2, respectively, resulting in a correction factor of 0.732. Accordingly, the component costs were updated using this factor.

The performance evaluation of each subsystem was further conducted through the SPECO method. Within this framework, the exergoeconomic factor was evaluated to assess the relation between the cost flow rates and the exergy destruction associated with a component.

For a sub-component *k*, the exergoeconomic factor is expressed by Equation (7) [21].

$$f_k = \frac{\dot{Z}_k}{\dot{Z}_k + c_{f,k} \cdot \dot{E}x_{D,k}}$$

Another key indicator in thermo-economic evaluation is the relative cost difference that reflects the relative increase in an average cost per unit exergy between fuel and product of a component defining for a sub-component *k* in Equation (8) [21-22].

$$r_k = \frac{c_{p,k} - c_{f,k}}{c_{f,k}}$$

Finally, the cost-rate associated with exergy-destruction is expressed in Equation (9) [21-22].

$$\dot{D}_{D,k} = c_{f,k}\dot{E}x_{D,k}$$

3. RESULTS AND DISCUSSION

3.1. Thermodynamic and Thermoeconomic Analyses

A thermoeconomic analysis was utilized on a re-compression S-CO_2 gas-turbine cycle powered by the BSWPP exhaust gas. The thermodynamic properties of the conducted system are detailed in Table 5. T–s diagram illustrating the gas-turbine cycle is presented in Figure 3.

The thermodynamic analyses of the GT-cycle were carried out using the equations provided in Table 1, with component-specific results summarized in Table 6. The analysis revealed a net power output of 108.65 kW, energy and exergetic efficiencies of 28.02% and 53.41%, respectively. These efficiency values are consistent with those reported for other S-CO_2 gas turbine cycles in the related literature [3–15]. Nonetheless, further improvements in both energetic and exergetic efficiencies are performed by minimizing exergy destruction within the system. As indicated in Table 6, the highest and lowest exergy-destruction occurred in the gas turbine heat-exchanger and high-pressure compressor, respectively. Significant exergy-destruction in the GTHE is attributed to the use of different working fluids in heat exchangers. Conversely, the recuperator and gas turbine exhibited the highest exergy efficiencies with the relatively low exergy-destruction in the recuperator explained by the use of fluids with similar properties and phases. However, the intercooler and precooler demonstrated the lowest exergy efficiencies, which can be associated with the cooling fluids employed. Notable inefficiencies were observed because water, which differs in both phase and properties from CO_2, was selected as the working fluid for these components.

A detailed assessment of the component-level irreversibilities reveals that the intercooler, precooler, and gas turbine heat exchanger dominate the overall exergy losses of the system. To mitigate these losses within the constraints of the present model, several practical strategies can be considered. For the intercooler and precooler, the use of alternative cooling fluids—such as glycol-based mixtures, nanofluid-enhanced media, or air-cooled configurations—may improve thermal matching and reduce entropy generation. Additionally, heat transfer enhancement techniques, including corrugated plates, finned geometries, or surface augmentation, could further increase heat transfer coefficients and lower required temperature differences. For the gas turbine heat exchanger, improved flow distribution, advanced compact heat exchanger designs, or enhanced recuperative configurations may substantially decrease the large exergy destruction linked to high temperature gradients and differing fluid properties. Literature-based performance data suggest that such improvements may reduce exergy destruction in these components by approximately 10–25%, depending on the adopted enhancement method. Therefore, focusing optimization efforts on these heat exchangers is expected to yield the highest potential gains in overall system thermoeconomic performance.

Table 5. Thermodynamic properties of the related cycle

State	Fluid	T $(°C)$	P (bar)	$\dot{m}$ (kg/s)	h (kJ/kg)	s $(kJ/kg.K)$	ψ (kJ/kg)	$\dot{E}x$ (kW)
0	CO_2	20	1.0	-	-5.168	-0.01403	-	-
0'	Water	20	1.0	-	83.93	0.2962	-	-
0"	Air	20	1.0	-	293.6	5.682	-	-
1	CO_2	40	85	1.49	-128.2	-1.164	214.1	315.6
2	CO_2	70.37	139.7	1.49	-114.8	-1.164	227.8	335.8
3	CO_2	40	139.7	1.49	-218.5	-1.48	216.3	318.9
4	CO_2	52.69	229.5	1.49	-207	-1.48	228	336
5	CO_2	252.1	229.5	1.49	153.3	-0.5909	327.5	482.8
6	CO_2	411	229.5	1.49	353.7	-0.257	430.1	634.1
7	CO_2	302.1	85	1.49	237.9	-0.257	318.8	470
8	CO_2	72.69	85	1.49	-32.06	-0.8684	223.6	329.5
9	Water	20	1	2.05	84.01	0.2965	0	0
10	Water	34	1	2.05	142.5	0.4915	1.354	2.788
11	Water	20	1	5.20	84.01	0.2965	0	0
12	Water	26	1	5.20	109.1	0.3812	0.2533	1.341
13	Exhaust	431	1.9	2.18	718.1	6.398	214.7	468.2
14	Exhaust	253.2	1.9	2.18	530.5	6.092	117	255.2

Table 6. Thermodynamic results of the cycle

Component	$\dot{\boldsymbol{Q}}$ $(\boldsymbol{kW})$	$\dot{\boldsymbol{W}}$ $(\boldsymbol{kW})$	$\dot{\boldsymbol{E}}\boldsymbol{x}_{\boldsymbol{F}}$ $(\boldsymbol{kW})$	$\dot{\boldsymbol{E}}\boldsymbol{x}_{\boldsymbol{P}}$ $(\boldsymbol{kW})$	$\dot{\boldsymbol{E}}\boldsymbol{x}_{\boldsymbol{D}}$ $(\boldsymbol{kW})$	$\boldsymbol{\varepsilon}$ (%)
GTHE	347.7	-	203.5	144.5	59.02	71
GT	-	147.8	154.3	147.8	6.501	95.79
REC	531.1	-	155.2	149.4	5.759	96.29
PRE	141.8	-	13.73	2.768	10.97	20.16
LP Comp	-	21.45	21.45	18.68	2.768	87.1
HP Comp	-	17.7	17.7	15.3	2.399	86.45
INT	132.8	-	16.14	1.317	14.82	8.163
GT System	Energy efficiency (%)			28.02		
	Exergy efficiency (%)			53.41		

The related thermoeconomic performance of the GT-cycle was evaluated using SPECO method. The capital investment requirements were found using the expressions provided in Table 4, while the operating and maintenance expenses were estimated based on the CEPCI in conjunction with the expressions given in Table 3. The corresponding exergy flow rates, cost flow rates, and unit exergy costs of the GT cycle are listed in Table 7. Although the GT exhibited relatively low exergy destruction, it possessed the highest exergoeconomic factor and relative cost difference among the system components shown in Table 8. This outcome is primarily attributed to the high capital cost rate. Similarly, the GTHE is characterized by a high relative cost difference and low exergoeconomic factor because of its significant exergy destruction. Moreover, heat exchangers generally present lower exergoeconomic factor values, which result from their comparatively high exergy-destruction costs, indicating that these components require particular attention to enhance the overall system performance. In contrast, both the low- and high-pressure compressors demonstrate higher exergoeconomic factor values similar to the GT, which can be explained by their relatively low exergy destruction costs.

Table 7. Exergy flow rates, cost flow rates and unit exergy costs of the cycle

State	$\dot{E}x$ (kW)	c $(\$/GJ)$	$\dot{C}$ $(\$/h)$
1	319.3	5.008	5.757
2	338	5.008	6.094
3	321.8	5.008	5.803
4	337.1	5.02	6.093
5	492.3	5.174	9.17
6	636.8	5.008	11.48
7	482.4	5.008	8.699
8	333	5.008	6.004
9	0	0	0
10	2.768	35.22	0.351
11	0	0	0
12	1.317	82.26	0.3901
13	350.4	2.538	3.202
14	146.9	2.538	1.343

Table 8. Thermoeconomic results of the cycle

Component	$\dot{E}x_D$ (kW)	c_f $(\$/GJ)$	c_p $(\$/GJ)$	$\dot{D}_D$ $(\$/h)$	$\dot{Z}$ $(\$/h)$	r (%)	f (%)
GTHE	59.02	2.538	5.035	0.5392	0.4662	98.39	46.37
GT	6.501	5,035	8.596	0.1178	2.9210	70.72	96.12
REC	5.759	5.035	5.201	0.7202	0.3833	3.286	34.74
PRE	10.97	5.035	5.035	0.1988	0.1033	1.18 x10^{-7}	34.20
LP Comp	2.768	3.483	5.035	0.0347	0.0697	44.55	66.75
HP Comp	2.399	3.483	5.047	0.0301	0.0697	44.89	69.84
INT	14.82	5.035	5.035	0.2686	0.0991	1.22 x10^{-9}	26.96

The relationship between PEC-based capital cost functions and the exergoeconomic performance becomes particularly evident in the gas turbine. As the turbine inlet pressure increases, the PEC-based cost shows only a modest rise according to the correlations in Table 4, while the accompanying thermodynamic improvement leads to a noticeable reduction in exergy destruction. Since the GT's total cost rate combines both capital and exergy destruction costs, the net effect is a decrease in the total cost rate at higher pressures. Conversely, heat exchangers exhibit significantly higher exergy destruction, and therefore their total cost rates are primarily driven by irreversibilities rather than PEC terms, leading to low exergoeconomic factors.

3.2. Parametric Studies

The parametric studies are carried out with regarding to pressure ratio, inlet pressure of gas turbine, dead-state temperature and logarithmic mean temperature difference. Energetic and exergetic efficiencies, total net power output and total cost rate of the GT are considered with respect to limits of the variable parameters.

3.2.1. Impact of Pressure Ratio on Cycle Performance

The pressure ratio is a vital parameter for power generation systems. Consequently, in the analysis of such systems, it is customary to investigate how variations in the pressure ratio influence system outputs. As pressure ratio raises, net power output shows a consistent upward trend as shown in Figure 2. However, the energy efficiency curve demonstrates a parabolic behaviour, reaching its peak around a pressure ratio of approximately 2.4, after which efficiency slightly decreases. This indicates that there exists an optimal pressure ratio for maximizing efficiency, although higher pressure ratios continue to enhance the absolute power generation. In Figure 3, both exergy efficiency and net power output increase with higher pressure ratios, though the rate of increase in exergy efficiency diminishes beyond a PR of about 2.5. This suggests that while improvements in power generation are significant at higher pressure ratios, gains in exergy efficiency gradually saturate, indicating diminishing returns from a thermodynamic performance perspective. The total cost rate exhibits a nearly linear increasing trend as the pressure ratio rises which is given in Figure 4. This implies that operating the system at higher pressure ratios, although beneficial in terms of power generation, results in increased economic costs. Thus, a techno-economic trade-off must be considered between higher performance and elevated operating expenses.

Figure 2. Influence of PR on energetic efficiency and net power output of the cycle

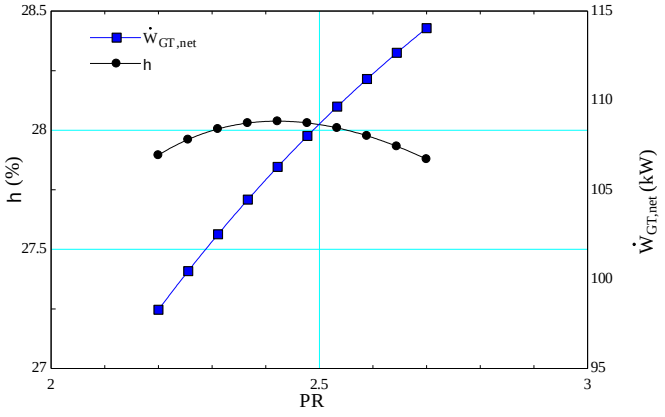

Figure 3. Influence of PR on exergetic efficiency and net power output of the cycle

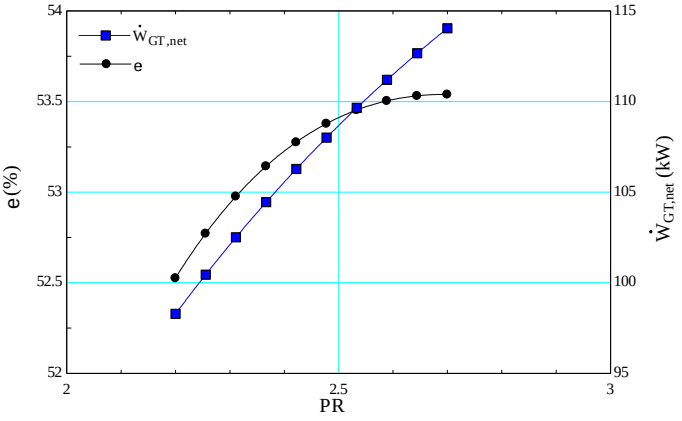

Figure 4. Influence of PR on total cost rate of the cycle

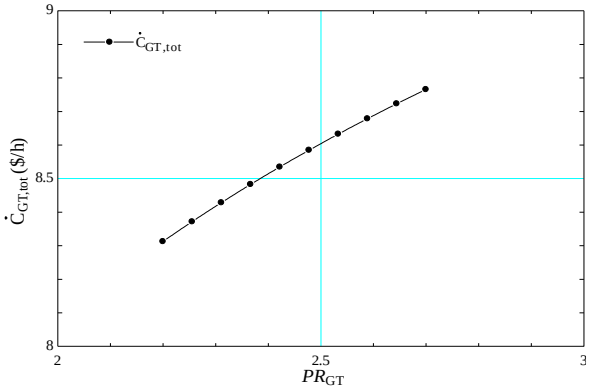

The design point selection was based on a thermo-economic compromise rather than solely maximizing net power or efficiency. Although the parametric analysis shows that net power output continues to rise with increasing pressure ratio, the cycle efficiency reaches its peak near PR = 2.5, while the total cost rate increases at higher PR values. Therefore, PR = 2.5 represents the most cost-effective operating point within the SPECO framework. Likewise, the turbine inlet pressure of approximately 229.5 bar was selected because it lies within the maximum-efficiency interval (225–230 bar) observed in the parametric analysis and ensures stable operation close to the critical region. These considerations guided the determination of the final design parameters.

3.2.2. Impact of Inlet Pressure of Gas Turbine on Cycle Performance

The effects of gas turbine inlet-pressure on power generation, energy and exergy efficiencies and total cost rate were evaluated. Figure 5 illustrates the change in energetic efficiency and net power output with respect to gas turbine inlet pressure. As the pressure rises from 185 bar to about 225 bar, both energetic efficiency and net power output rise steadily. The efficiency reaches a maximum value of approximately 28.7% near 225 bar, after which it slightly decreases, while the power output continues to increase but eventually stabilizes beyond 230 bar. This behaviour indicates that although higher inlet pressures enhance performance, there is an optimal range where efficiency gains are maximized, beyond which diminishing returns occur. The relationship between exergetic efficiency and also net power output across different turbine inlet pressures is given in Figure 6. Exergy efficiency increases gradually from around 52% to nearly 55% as pressure rises, reaching its peak in the range of 225–230 bar. The net power output follows a similar pattern, demonstrating a strong correlation with exergy efficiency. However, beyond the optimum pressure region, both parameters exhibit stabilization, and in the case of efficiency, a slight decline is observed. These results suggest that exergy utilization improves significantly with increasing pressure, but further increases beyond the optimum do not yield substantial improvements. The effect of turbine inlet pressure on the total cost-rate of the system is given in Figure 7. Unlike the efficiency trends, the total cost rate decreases consistently with increasing pressure, dropping from about 8.65 $/h at 185 bar to approximately 8.55 $/h at 235 bar. This steady reduction suggests that operating at higher inlet pressures provides a clear economic advantage, as improved thermodynamic performance translates into lower specific costs. Therefore, the results emphasize that higher gas turbine inlet pressures not only enhance technical performance but also contribute to improved economic feasibility.

Figure 5. Influence of P6 on energetic efficiency and net power output of the cycle

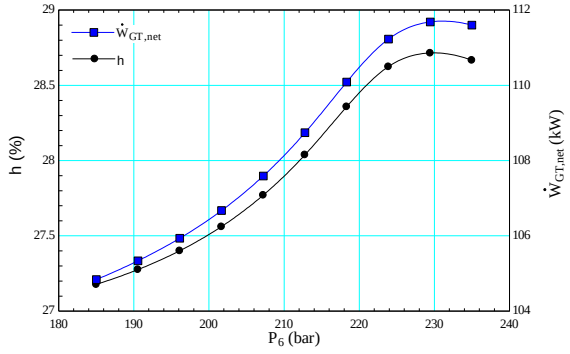

Figure 6. Influence of P6 on exergetic efficiency and net power output of the cycle

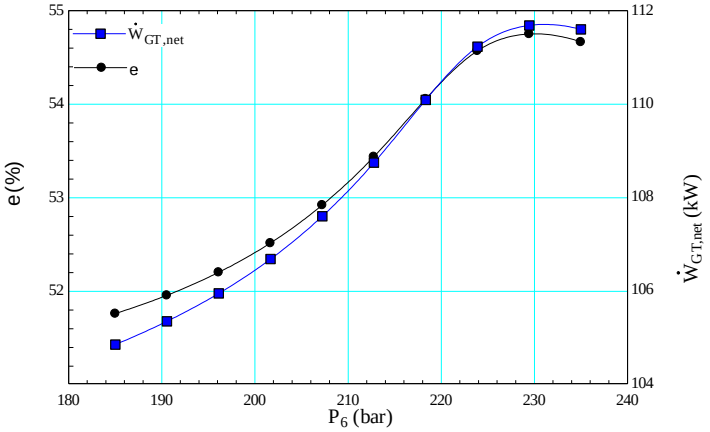

Figure 7. Influence of P6 on total cost rate of the cycle

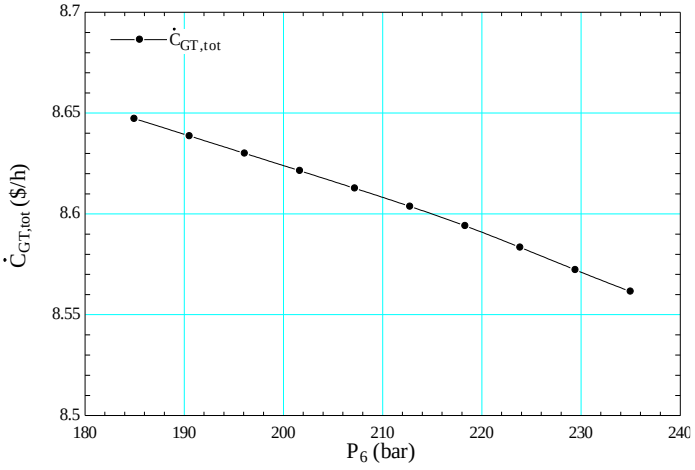

3.2.3. Impact of Dead-State Temperature on Cycle Performance

The dead-state temperature effects on thermoeconomic performance of the system were considered as another parameter. Figure 8 illustrates the change in both energetic efficiency and net power output with respect to dead-state temperature. Both parameters exhibit a clear downward trend as the temperature increases from 16 °C to 23 °C. Energetic efficiency decreases from nearly 30% to nearly 27%, while net power output drops from around 116 kW to nearly 104 kW. This indicates that higher dead state temperatures negatively affect system performance by reducing the ability of the cycle to convert available energy into useful work. Thus, operating at lower dead state temperatures enhances both efficiency and power generation. In Figure 9, the influence of dead-state temperature on both exergetic efficiency and net power output. Similar to the energy efficiency trend, both exergy efficiency and power output decline as the dead-state temperature rises. Exergy efficiency decreases from approximately 56.5% at 16 °C to about 52% at 23 °C, demonstrating the sensitivity of exergy performance to environmental reference temperature. The net power output follows the same decreasing pattern, emphasizing that increasing dead state temperature reduces the work potential and also consequently the system's effective performance. The relationship between total cost rate and dead state temperature shown in Figure 10. In contrast to efficiency trends, the total cost rate decreases steadily with increasing temperature, dropping from nearly 8.68 $/h at 16 °C to about 8.55 $/h at 23 °C. This behaviour implies that while thermodynamic performance deteriorates at higher dead state temperatures, the system's cost per unit time shows a slight economic improvement. However, considering the simultaneous drop in efficiency and power output, this economic advantage may not outweigh the performance losses, highlighting the trade-off between cost and efficiency under varying environmental conditions.

Figure 8. Influence of T0 on energetic efficiency and net power output of the cycle

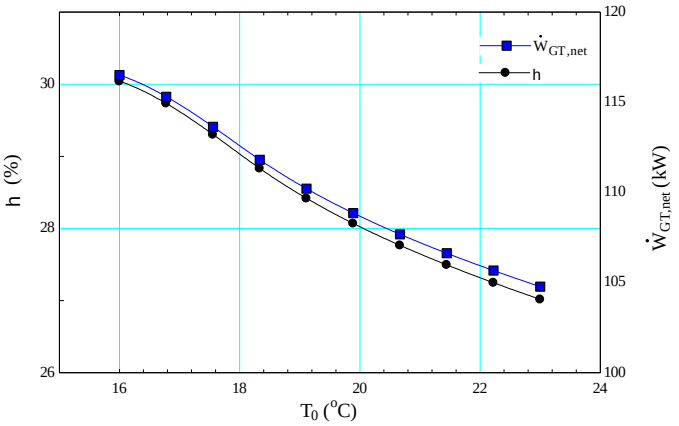

Figure 9. Influence of T0 on exergetic efficiency and net power output of the cycle

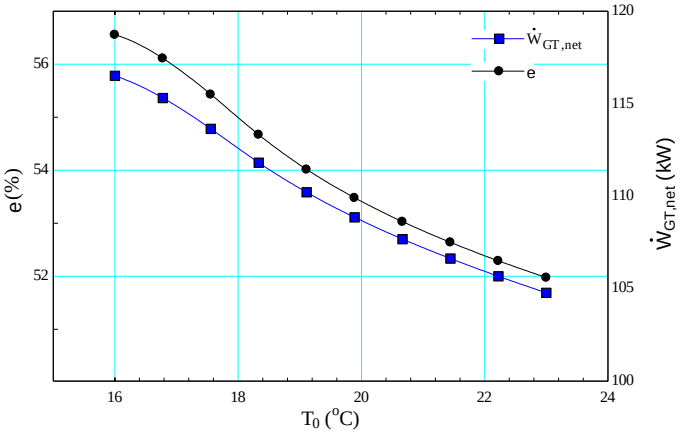

Figure 10. Influence of T0 on total cost rate of the cycle

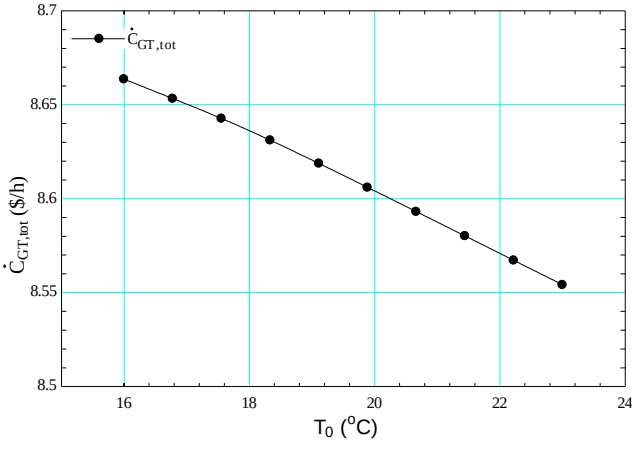

The reduction in total cost rate at higher dead-state temperatures results from the reference-state dependence of exergy. As T_0 increases, the exergy of heat and work interactions decreases, reducing exergy destruction across all components. Because exergy destruction cost dominates the SPECO cost rate while capital cost remains unchanged, the overall cost rate declines despite reductions in thermal efficiency and net power output.

3.2.4. Impact of Logarithmic Mean Temperature Difference (LMTD) on Cycle Performance

The influence of the LMTD on power generation systems is considered as another parameter to be taken into consideration. The influence of the LMTD on energetic efficiency and net power output is given in Figure 11. As LMTD increases from about 6 to 10, both efficiency and power output steadily decline. Energy efficiency drops from nearly 30% to around 26.5%, while net power output falls from nearly 112 kW to nearly 101 kW. This trend suggests that higher LMTD values reduce the thermodynamic driving force in heat exchangers, which in turn diminishes the system's energy conversion effectiveness and overall power generation. Figure 12 illustrates the variation of exergetic efficiency and also net power output with LMTD. Both parameters show a clear downward trend as LMTD increases. Exergy efficiency decreases from approximately 57% to about 50%, while net power output decreases from around 112 kW to 101 kW. The decline in exergy efficiency reflects increasing irreversibilities within the system as the temperature difference grows, leading to less effective utilization of available energy. Therefore, maintaining a lower LMTD enhances exergy performance and power output simultaneously. The relationship between total cost rate and LMTD shown in Figure 13. In contrast to efficiency trends, the total cost rate decreases only slightly as LMTD increases, dropping from about 8.62 $/h to 8.57 $/h. This indicates that the economic cost per unit time is only marginally affected by LMTD, even though efficiency and power generation are significantly reduced. Consequently, while higher LMTD values might appear economically favourable, they are not advantageous from a thermodynamic performance perspective.

Figure 11. Influence of LMTD on energetic efficiency and net power output of the cycle

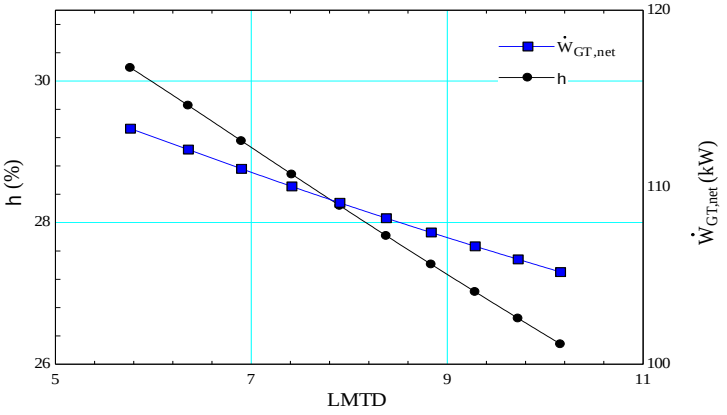

Figure 12. Influence of LMTD on exergetic efficiency and net power output of the cycle

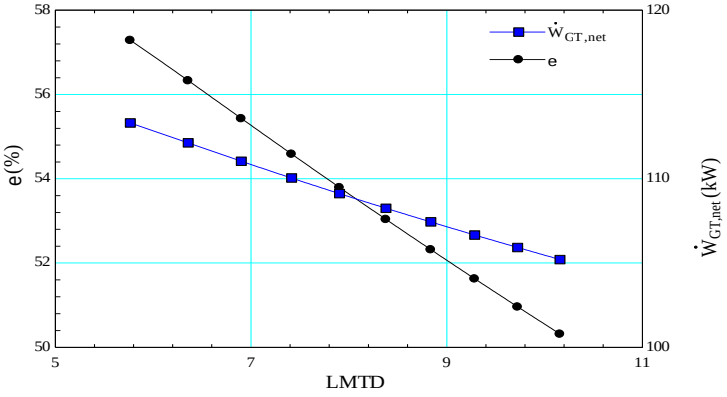

Figure 13. Influence of LMTD on total cost rate of the cycle

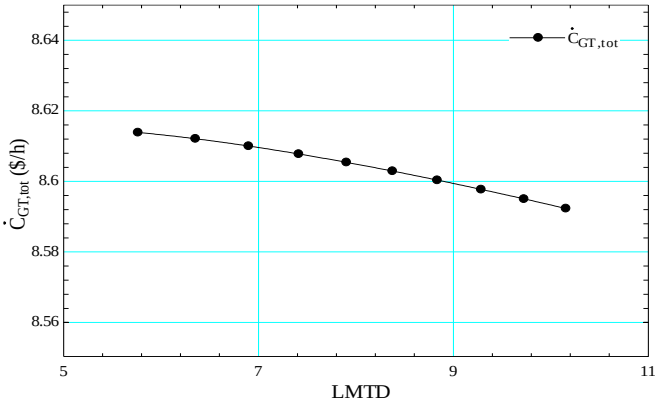

4. CONCLUSION

The thermodynamic analyses of the gas turbine (GT) system revealed that the overall energy efficiency was calculated as 28.02%, while the exergy efficiency reached 53.41%. Among the individual components, the gas turbine itself (GT) and the recuperator (REC) showed the highest exergy efficiencies, with values of 95.79% and 96.29%, respectively. In contrast, components such as the precooler (PRE) and intercooler (INT) exhibited significantly lower exergy efficiencies of 20.16% and 8.16%, which indicates substantial irreversibilities in heat exchange processes. The largest exergy-destruction occurred in the gas turbine heat exchanger (GTHE), with 59.02 kW, followed by the intercooler with 14.82 kW, highlighting the main sources of performance losses in the cycle. Herein, the highest exergy destruction amount of GTHE can be related to the difference of the temperature of the fluids and the different type phases of fluid. Besides, the high exergetic efficiencies of power producing/consuming equipments can be acceptable for all thermal power systems. It is indicated that the gas turbine heat exchanger (GTHE) and the intercooler (INT) exhibit the highest exergy-destruction values, which in turn lead to the largest cost rates of exergy-destruction within the system. The recuperator (REC), despite having relatively high thermodynamic performance, shows a considerable share of capital cost rate, making it a critical component from an investment perspective. Conversely, the compressors (LP and HP) demonstrate low unit exergy costs of fuel and product, coupled with favorable exergoeconomic factors, confirming their cost-effectiveness in the cycle. The relative cost difference (r) is most pronounced in the heat exchangers, suggesting mismatches between fuel and product costs that reduce overall system cost-effectiveness. Overall, the exergoeconomic analysis reveals that while the turbine and compressors operate efficiently in the frame of both thermodynamics and economical aspects, optimization efforts should primarily focus on the heat exchangers, especially the GTHE and INT, to minimize cost-based irreversibilities and enhance the economic sustainability of the cycle. This outcome is consistent with the expected behaviour of heat exchangers. Based on these results, future studies should focus on developing the thermodynamic and economic performance of heat exchangers, particularly the gas turbine heat-exchanger and the intercooler, as they contribute most to exergy destruction and cost irreversibilities. Advanced heat transfer enhancement techniques, alternative working fluids, or novel exchanger configurations may be investigated to reduce losses and improve exergoeconomic factors. In addition, system-level optimization approaches, such as multi objective optimization considering both efficiency and cost, could be applied to identify more sustainable operating conditions. Finally, integrating the cycle with other heat recovery systems or renewable energy sources may further enhance overall system efficiency and economical viability, making the configuration more attractive for real-world applications.

Nomenclature

A	heat transfer area, m^2
$\dot{C}$	cost rate, \$/h
c	cost per exergy unit, \$/GJ
c_f	unit exergy cost of fuel, \$/GJ
c_p	unit exergy cost of fuel, \$/GJ
$\dot{D}$	cost rate of exergy destruction, \$/h
$\dot{E}x$	exergy rate, kW
f	exergoeconomic factor
h	specific enthalpy, kJ/kg
i	interest rate
$\dot{m}$	mass flow rate, kg/s
n	total life time
N	annual operation time
P	pressure, bar
PR	pressure ratio
$\dot{Q}$	heat addition, kW
r	relative cost difference
s	specific entropy, kJ/kg-K
T	temperature, ^oC
U	heat transfer coefficient, kW/m^2-K
$\dot{W}$	work flow rate-power, kW
$\dot{Z}$	capital cost rate, \$/h

Greek symbols

ε	exergy efficiency
εf	effectiveness
η	energy efficiency
η_C	compressor isentropic efficiency
η_{GT}	turbine isentropic efficiency
ϕ	maintenance factor
ψ	specific flow exergy, kJ/kg

Subscripts

0	dead state
a	actual
crit	critical point
D	destruction
exh	exhaust
k	component
s	isentropic
tot	total
wat	water

Abbreviations

CEPCI	chemical engineering plant cost index
CRF	capital recovery factor
EMO	evolutionary multi-objective optimization
GMSWPP	Gaziantep Municipal Solid Waste Power Plant
GT	gas turbine
GTHE	gas turbine heat exchanger
HE	heat exchanger
HP Comp	high pressure compressor
INT	intercooler
LMTD	logarithmic mean temperature difference
LP Comp	low pressure compressor
NSGA-II	non-dominated sorting genetic algorithm
PEC	purchased equipment cost
PRE	precooler
REC	recuperator
S-CO_2	supercritical carbon dioxide
SPECO	specific exergy costing
T-CO_2	transcritical carbon dioxide

Acknowledgements

This study is supported by TUBİTAK (the Scientific and Technological Research Council of Turkey) with the project under the grant number of 114M142. The authors would like to thank TUBİTAK and CEV (Clean Energy & Vehicles) energy.

REFERENCES

[1] O. Olumayegun, M. Wang, and G. Kelsall, "Closed-cycle gas turbine for power generation: A state-of-the-art review," *Fuel*, vol. 180, pp. 694–717, 2016.

[2] Reuters Echogen Power Systems, "Waste heat recovery system available as turnkey solution 1," 2014–2015.

[3] Y. Ahn, S. Bae, M. Kim, S. Cho, S. Baik, J. Lee, and J. E. Cha, "Review of supercritical CO2 power cycle technology and current status of research and development," *Nucl. Eng. Technol.*, vol. 47, pp. 647–661, 2015.

[4] A. D. Akbari and S. M. S. Mahmoudi, "Thermoeconomic analysis & optimization of the combined supercritical CO2 recompression Brayton/organic Rankine cycle," *Energy*, vol. 78, pp. 501–512, 2014.

[5] J. Cha, T. Lee, J. Eoh, S. Seong, S. Kim, D. Kim, M. H. Kim, T.-W. Kim, and K.-Y. Suh, "Development of a supercritical CO2 Brayton energy conversion system coupled with a sodium cooled fast reactor," *Nucl. Eng. Technol.*, vol. 41, pp. 1025–1044, 2009.

[6] S. Ishiyama, Y. Muto, Y. Kato, S. Nishio, T. Hayashi, and Y. Nomoto, "Study of steam, helium and supercritical CO2 turbine power generations in prototype fusion power reactor," *Prog. Nucl. Energy*, vol. 50, pp. 325–332, 2008.

[7] F. Mohammadkhani, N. Shokati, S. M. S. Mahmoudi, M. Yari, and M. A. Rosen, "Exergoeconomic assessment and parametric study of a gas turbine-modular helium reactor combined with two organic Rankine cycles," *Energy*, vol. 65, pp. 533–543, 2014.

[8] X. Wang and Y. Dai, "An exergoeconomic assessment of waste heat recovery from a Gas Turbine-Modular Helium Reactor using two transcritical CO2 cycles," *Energy Convers. Manage.*, vol. 126, pp. 561–572, 2016.

[9] J. Wang, Z. Yan, M. Wang, M. Li, and Y. Dai, "Multi-objective optimization of an organic Rankine cycle (ORC) for low grade waste heat recovery using evolutionary algorithm," *Energy Convers. Manage.*, vol. 71, pp. 146–158, 2013.

[10] J. Wang, Z. Sun, Y. Dai, and S. Ma, "Parametric optimization design for supercritical CO2 power cycle using genetic algorithm and artificial neural network," *Appl. Energy*, vol. 87, pp. 1317–1324, 2010.

[11] A. Kouta, A. F. Al-Sulaiman, and M. Atif, "Energy analysis of a solar driven cogeneration system using supercritical CO2 power cycle and MEE-TVC desalination system," *Energy*, vol. 119, pp. 996–1009, 2017.

[12] D. Milani, M. Tri Luu, R. McNaughton, and A. Abbas, "A comparative study of solar heliostat assisted supercritical CO2 recompression Brayton cycles: dynamic modelling and control strategies," *J. Supercrit. Fluids*, vol. 120, pp. 113–124, 2017.

[13] H. Nami, S. M. S. Mahmoudi, and A. Nemati, "Exergy, economic and environmental impact assessment and optimization of a novel cogeneration system including a gas turbine, a supercritical CO2 and an organic Rankine cycle (GT-HRSG/SCO2)," *Appl. Therm. Eng.*, vol. 110, pp. 1315–1330, 2017.

[14] M. H. Ahmadi, M. Mehrpooya, and F. Pourfayaz, "Exergoeconomic analysis and multi objective optimization of performance of a Carbon dioxide power cycle driven by geothermal energy with liquefied natural gas as its heat sink," *Energy Convers. Manage.*, vol. 119, pp. 422–434, 2016.

[15] M. S. Kim, Y. Ahn, B. Kim, and J. I. Lee, "Study on the supercritical CO2 power cycles for landfill gas firing gas turbine bottoming cycle," *Energy*, vol. 111, pp. 893–909, 2016.

[16] F. A. Boyaghchi and H. Safari, "Parametric study and multi-criteria optimization of total exergetic and cost rates improvement potentials of a new geothermal based quadruple energy system," *Energy Convers. Manage.*, vol. 137, pp. 130–141, 2017.

[17] Y. Feng, Y. Zhang, B. Li, J. Yang, and Y. Shi, "Comparison between regenerative organic Rankine cycle (RORC) and basic organic Rankine cycle (BORC) based on thermoeconomic multi-objective optimization considering exergy efficiency and levelized energy cost (LEC)," *Energy Convers. Manage.*, vol. 96, pp. 58–71, 2015.

[18] Z. Hajabdollahi and P. F. Fu, "Multi-objective-based configuration optimization of SOFC-GT cogeneration plant," *Appl. Therm. Eng.*, vol. 112, pp. 549–559, 2017.

[19] V. Jain, G. Sachdeva, S. S. Kachhwaha, and B. Patel, "Thermo-economic and environmental analyses based multi-objective optimization of vapor compression absorption cascaded refrigeration system using NSGA-II technique," *Energy Convers. Manage.*, vol. 113, pp. 230–242, 2016.

[20] Y. Li, S. Liao, and G. Liu, "Thermo-economic multi-objective optimization for a solardish Brayton system using NSGA-II and decision making," *Electr. Power Energy Syst.*, vol. 64, pp. 167–175, 2015.

[21] O. Güngör, A. Tozlu, C. Arslantürk, and E. Özahi, "District heating based on exhaust gas produced from end-of-life tires in Erzincan: Thermoeconomic analysis and optimization," *Energy*, vol. 294, p. 130755, 2024.

[22] A. Tozlu, E. Özahi, and A. Abuşoğlu, "Waste to Energy Technologies for Municipal Solid Waste Management in Gaziantep," *Renew. Sustain. Energy Rev.*, vol. 54, pp. 809–815, 2016.

[23] A. Tozlu, E. Özahi, and A. Abuşoğlu, "Energetic and Exergetic Analyses of a Solid Waste Power Plant using Aspen Plus," *Int. J. Energy*, vol. 10, pp. 44–47, 2016.

[24] V. Zare, S. M. S. Mahmoudi, and M. Yari, "An exergoeconomic investigation of waste heat recovery from the Gas Turbine-Modular Helium Reactor (GT-MHR) employing an ammonia-water power/cooling cycle," *Energy*, vol. 61, pp. 397–409, 2013.

[25] H. Ozcan and I. Dincer, "Exergoeconomic optimization of a new four-step magnesium chlorine cycle," *Int. J. Hydrogen Energy*, vol. 42, pp. 2435–2445, 2017.

International Journal of Energy Horizon 02 (2025) 80-89

International Journal of Energy Horizon

journal homepage: https://dergipark.org.tr/tr/pub/ijeh

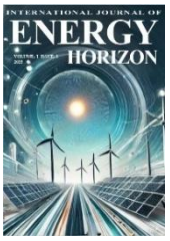

Research Article

Development of a UA-independent effectiveness-thermal length method for heat exchanger performance prediction

Hakan İbrahim Tol[1,*]

[1] DR TOL Mühendislik Danışmanlık Ticaret ve Sanayi Limited Şirketi | Hamidiye Neighbourhood, Silifke Street, No: 147/7, 33010, Mersin, Türkiye
[1]ORCID No: 0000-0002-2752-8038

ARTICLE INFO

Article History:

Received:27 October 2025
Revised:19 November 2025
Accepted:22 November 2025
Available online:30 November 2025

Keywords:

Heat Exchanger
Thermal Length
Effectiveness–Thermal Length
Effectiveness–NTU
Thermal Modelling
District Heating

ABSTRACT

This paper proposes and validates a UA-independent Effectiveness–Thermal Length (ε–θ) framework, where ε denotes heat exchanger effectiveness and θ an identified thermal length, for steady-state prediction of Plate Heat Exchanger (PHE) performance in single-phase water applications, with emphasis on district heating substations and return-temperature control. Instead of requiring an overall conductance, the method expresses effectiveness as a compact function of a UA-free thermal-length proxy r=A/Cmin (heat-transfer area divided by the minimum heat-capacity rate) and capacity-rate ratio C*, modulated by identified coefficient functions α(C*) and β(C*). We implement ε–θ alongside classical ε–NTU and LMTD models and evaluate three aspects: (i) baseline behaviour against canonical trends, (ii) validation using manufacturer-grade catalogue data, and (iii) parametric analysis spanning Reynolds number, thermal length, and C*. When all methods share the same conductance assumption, ε–θ recovers ε–NTU/LMTD predictions with negligible outlet-temperature error (on the order of hundredths of a kelvin), confirming thermodynamic coherence for single-pass counter-current service. Differences emerge where design decisions are most sensitive (low NTU and high C*) in which ε–θ provides practical, UA-free return-temperature predictions suitable for early sizing and scenario studies. Across typical PHE operating envelopes (NTU ≳ 3), ε saturates rapidly with r, rendering predictions robust to realistic flow-driven Reynolds-number variation. The framework is computationally lean and readily embeddable in selection tools, system simulators, and digital twins, offering a transparent bridge between sizing (via r), flow imbalance (via C*), and effectiveness without reliance on proprietary UA data. Across the validation dataset, the ε–θ framework reproduces manufacturer-grade plate heat exchanger performance with a mean absolute error of [MAE] K and a root-mean-square error of [RMSE] K in cold-side outlet temperature, comparable to ε–NTU/LMTD benchmarks.

1. INTRODUCTION

As a fundamental component of thermal engineering science, heat exchangers enable the controlled transfer of energy between fluid streams at different grade levels of energy. This function is critical for achieving higher energy efficiency, ensuring precise process control, and delivering associated environmental benefits through reduced fuel consumption and emissions. Typical applications include waste heat recovery, where otherwise unused thermal energy is reclaimed; optimization of industrial processes by maintaining prescribed temperature levels; and provision of essential heating and cooling across diverse domains, ranging from air conditioning and refrigeration to cryogenics and power generation. The breadth of heat exchanger applications is extensive, encompassing industrial, transportation, commercial, and residential sectors. In each case, system performance is closely coupled to the efficiency, operational stability, and economic viability of the installed heat exchange units [1,2].

1.1 Background

With the growing complexity of modern applications (including integration of renewable energy sources, multi-grade energy recovery, and dynamic operating environments) there is an increasing demand for robust, rapid, and accurate methods for predicting heat exchanger performance. Such methods are indispensable not only for design and sizing tasks, but also for performance (rating) evaluation, real-time simulation, and system-level optimization. The development of generalized yet computationally efficient predictive frameworks therefore represents both a scientific challenge and an engineering necessity.

*Corresponding author
E-mail address: hakantol@gmail.com
journal homepage: https://dergipark.org.tr/tr/pub/ijeh

1.2 Problem Statement

Despite their longstanding use and pedagogical importance, the two classical approaches for heat exchanger analysis (the Logarithmic Mean Temperature Difference (LMTD) method and the Effectiveness–Number of Transfer Units (ε–NTU) method) exhibit inherent limitations when applied to contemporary engineering problems. The LMTD method, while suitable for rating calculations, requires knowledge of outlet temperatures, making it impractical for predictive tasks where only inlet states and heat duties are specified. Conversely, the ε–NTU method provides predictive capability by linking effectiveness to the number of transfer units and capacity rate ratios, yet it presupposes knowledge of the overall conductance *UA* and relies on idealized assumptions regarding flow configurations, uniform thermophysical properties, and invariant geometry[1,2].

These restrictions become pronounced in real-world applications where operating conditions are variable, geometries deviate from textbook configurations, and fluids experience property variations along the flow path. In district heating substations, for instance, accurate determination of primary return temperature is central to network, pumping energy, and integration of low-temperature heat sources [3–7]. However, in many practical design and retrofit studies, engineers have access only to manufacturer or catalogue data (inlet/outlet temperatures, flow rates, and heat duties) rather than detailed geometric information or reliable *UA* estimates [3–5].

Compact plate heat exchangers illustrate this difficulty. Their performance depends strongly on corrugation pattern, plate spacing, and flow distribution. Advanced modelling approaches based on detailed thermal–hydraulic correlations and discretized formulations have been proposed for brazed plate heat exchangers [6,7], and dynamic effectiveness methods have been introduced to capture transient behaviour [8]. While these contributions are valuable, they typically remain UA-dependent and require geometry, correlation parameters, or extensive calibration data that are not readily available in early-stage district heating design or when only catalogue-grade information is provided.

Consequently, there is a methodological gap between, on the one hand, classical LMTD/ε–NTU formulations that demand an explicit *UA*, and, on the other hand, high-fidelity discretized or dynamic models that are too data-intensive or computationally heavy for routine use in system studies. What is missing is a compact, thermodynamically consistent framework that;

(i) operates directly on the types of data commonly supplied in manufacturer catalogues and district heating studies,

(ii) avoids explicit dependence on *UA*, and

(iii) remains sufficiently lightweight for integration into selection tools, network simulators, and digital twins.

1.3 Aim, Objectives and Scope

The primary aim of this study is to develop and validate a new UA-independent Effectiveness–Thermal Length (ε–θ) framework for heat exchanger performance prediction. The framework is conceived as a generalized formulation that links exchanger effectiveness to a thermal-length measure derived from observable operating data, rather than from explicit conductance or geometric information. In doing so, it extends and complements the capabilities of the conventional LMTD and ε–NTU methods by providing a predictive tool that remains usable when *UA* and detailed plate-level correlations are unknown, as is often the case in district heating substations and catalogue-based design contexts.

To achieve this aim, the study pursues the following Research Objectives (RO):

RO1: Formulation of the ε–θ Method: Derive the theoretical basis of the framework, including the definition of thermal length, its integration with effectiveness, and the establishment of generalized governing relations.

RO2: Comparative Evaluation: Assess the performance of the ε–θ method against classical approaches (LMTD and ε–NTU), highlighting similarities, differences, and improvements in predictive capability.

RO3: Validation and Application: Demonstrate the accuracy and robustness of the ε–θ framework by applying it to representative case studies, with particular focus on predicting outlet and return temperatures in plate heat exchangers.

The scope of the present work is deliberately defined to ensure clarity and rigour in the development of the framework. The analysis is restricted to single-phase heat transfer applications with water as the working fluid, in line with district heating and general heating applications. Nevertheless, the theoretical formulation is structured to be extendable to other working fluids and heat exchanger types, thereby enabling future applications to two-phase processes, compact geometries, and transient operating conditions. This balance between focus and generality ensures that the contribution is both scientifically robust and practically relevant.

1.4 Significance

The development of robust and generalized methods for heat exchanger performance prediction holds considerable significance for both thermal sciences and applied energy engineering. From an applied perspective, accurate yet computationally efficient prediction of outlet and, in particular, return temperatures is essential for system-level performance. In district heating networks, the primary return temperature governs network exergy losses, pumping power, and the feasibility of integrating low-temperature and renewable heat sources [9,10]. Similar considerations arise in industrial processes and refrigeration systems, where compact plate heat exchangers play a critical role in achieving high efficiency and stable operation [1].

In many of these applications, however, detailed geometric data and reliable *UA* estimates are not available at the stage where strategic decisions are taken. Engineers frequently rely on manufacturer catalogues or limited test data, which provide inlet/outlet temperatures and flow rates but not the full information required by classical LMTD/ε–NTU formulations or correlation-based discretized models [6,7]. This misalignment between available data and model requirements constrains early-stage sizing, retrofit screening, and system-level scenario analysis.

By introducing a UA-independent ε–θ framework that identifies an exchanger-specific thermal length from performance data and parameterizes effectiveness through a UA-free thermal-length proxy $r=A/C_{min}$ and capacity-rate ratio C^*, the present work directly addresses this gap. The formulation is deliberately lightweight, permitting rapid evaluation of outlet and return temperatures while preserving thermodynamic consistency with classical methods when conductance assumptions coincide. This makes the ε–θ framework well suited for integration into simulation platforms, selection software, and digital twin environments, where speed and robustness are as important as physical fidelity. At the same time, the underlying structure is sufficiently general to support future extensions to other working fluids, flow arrangements, and dynamic operating conditions [6–8].

1.5 Literature Review

The modelling of heat exchanger performance has received extensive attention in the scientific literature, with approaches ranging from empirical correlations to advanced discretized and transient methods. For compact heat exchangers, early research established the limitations of lumped parameter formulations, prompting the development of generalized methods capable of addressing variable operating conditions and complex geometries.

In the context of compact brazed plate heat exchangers, Gullapalli [6] proposed a computationally efficient discretized rating scheme integrated with empirical thermal–hydraulic correlations, aiming to provide robust performance prediction for single-phase, condensation, and evaporation applications. This work highlighted the importance of computationally light yet generalizable frameworks that could be embedded into design and selection software. Similarly, Gusew [7] investigated heat transfer in plate heat exchangers in the transitional flow regime, proposing empirical correlations that capture the variation of heat transfer exponents with Reynolds number and geometry. These contributions underline the necessity of models that can bridge laminar, transitional, and turbulent regimes in practical operating envelopes.

Dynamic modelling has also been pursued to account for transient behaviour. Gao et al. [8] introduced a transient effectiveness method for cross-flow heat exchangers, incorporating finite wall capacitance to predict outlet temperatures under step, ramp, and exponential variations of inlet conditions. Such approaches provide insight into the time-dependent response of heat exchangers, yet their complexity often precludes direct use in lightweight performance prediction frameworks.

Further contributions have emphasized the integration of ε–NTU relationships into generalized modelling schemes. For example, Fernández Torrijos et al. [11] developed ε–NTU formulations for series–parallel arrangements, facilitating the prediction of outlet conditions for non-ideal flow configurations commonly found in plate and tubular exchangers. Their work demonstrated the utility of effectiveness-based relations in capturing complex flow arrangements without resorting to fully discretized models.

Taken together, these studies demonstrate that high-fidelity, correlation-based and discretized models, as well as advanced ε–NTU formulations for complex flow arrangements, can achieve accurate prediction of heat exchanger performance when detailed geometric and conductance information is available. Nevertheless, they remain fundamentally UA-dependent and are not designed to operate directly

on sparse catalogue data or the limited measurement sets that are typical in early-stage district heating and system-integration studies. To the best of the authors' knowledge, the literature does not yet offer a thermodynamically consistent, UA-independent effectiveness formulation that can be identified from manufacturer-grade data and then used as a compact surrogate in system-level analyses. The ε–θ framework proposed in this work is intended to fill this niche by providing such a reduced-order, data-driven yet physics-consistent mapping.

From a methodological standpoint, heat exchanger performance prediction has traditionally relied on two main classes of models. The first comprises analytical methods such as LMTD and ε–NTU, which provide closed-form relations between effectiveness, terminal temperatures and capacity-rate ratio and are widely used in rating and design calculations [12]. These approaches, however, remain explicitly dependent on the overall conductance *UA* and are typically formulated for idealised flow arrangements. The second class comprises correlation-based and discretised models, particularly for compact plate heat exchangers, where local heat transfer and pressure drop are described via empirical correlations as functions of Reynolds and Prandtl numbers, plate geometry and chevron pattern [13]. While such models can predict performance accurately when detailed geometric information is available, they require more input data and calibration than are usually accessible in early-stage district heating or catalogue-based studies. The UA-independent Effectiveness–Thermal Length (ε–θ) framework developed in this work is intended to bridge this gap by offering a compact, physics-consistent performance-prediction relation that operates directly on observable performance data and remains compatible with the qualitative behaviour of ε–NTU formulations.

1.6 Novelty

The novelty of the present study lies in the introduction and validation of a new UA-independent ε–θ framework for heat exchanger performance prediction, tailored to situations where only limited performance data are available. While the classical LMTD and ε–NTU methods have long served as the foundation for thermal design and analysis [2,12], both approaches remain constrained by specific boundary requirements and by their explicit dependence on *UA* and detailed geometry. The LMTD method is inherently a rating tool that requires all terminal temperatures, thereby limiting its utility in predictive tasks. Conversely, the ε–NTU method provides predictive capability but is strongly coupled to predefined flow arrangements and relies on assumptions that reduce its applicability under variable operating conditions.

The ε–θ framework advances the state of the art in three distinctive ways:

- Instead of relating effectiveness exclusively to the number of transfer units and capacity rate ratios, the ε–θ approach introduces a dimensionless thermal length parameter that encapsulates both geometric and operating characteristics. This parameterization enables a more generalized representation of exchanger behaviour, providing a continuous and flexible predictive tool that is not restricted to classical flow arrangements.
- By establishing an analytical structure that unifies elements of the LMTD and ε–NTU approaches, the ε–θ framework effectively bridges the gap between rating-oriented and prediction-oriented methods. This dual capability allows for both design verification (rating) and operational forecasting (prediction), which are typically treated separately in conventional analyses.
- Unlike high-resolution discretized models, which can provide accuracy at the expense of computational burden [7,8], the ε–θ framework is designed as a reduced-order formulation. Its lightweight mathematical structure ensures robustness, quickness, and accuracy, making it suitable not only for design environments but also for real-time applications such as system simulation, control, and digital twins.

This study represents the first systematic effort to formulate, implement, and validate the ε–θ approach that is;

(i) calibrated directly on manufacturer-grade plate heat exchanger data,

(ii) benchmarked against ε–NTU and LMTD under identical conditions, and

(iii) exploited for UA-free parametric analysis relevant to district heating and building-level applications.

To the best of the authors' knowledge, no prior work has established such a generalized effectiveness relation based explicitly on thermal length and designed for operation without explicit *UA*. By addressing this methodological gap, the ε–θ framework provides both a theoretical advance in thermal sciences and a practical tool for energy system applications where predictive reliability, data frugality, and computational efficiency are indispensable.

2. METHOHDS

The methodological approach adopted in this study is designed to develop, formalize, and validate a new ε–θ framework for heat exchanger performance prediction. Unlike classical approaches that depend on explicit knowledge of the overall heat transfer coefficient U [W/m^{2}K] and effective area A [m^2], the proposed method introduces an identifiable, exchanger-specific thermal length parameter (θ^*), obtained directly from measured or manufacturer performance data. In this formulation, θ^* serves as a dimensionless invariant that encapsulates the combined thermal and geometric characteristics of the exchanger, thereby eliminating the need to estimate U and A. This redefinition makes the framework operationally independent of geometric inputs, enabling accurate and computationally efficient prediction of outlet and return temperatures even when manufacturer information is incomplete, a common limitation in practical applications.

In line with classical ε–NTU analyses and plate heat exchanger studies [12,14,15], the model assumes steady-state, one-dimensional heat transfer with negligible heat losses to the surroundings and negligible axial conduction. The working fluid is single-phase water, with thermophysical properties taken as constant and evaluated at the mean bulk temperature in each stream, which is a common approximation in single-phase heat exchanger design [12,14,16]. The flow distribution in each pass is assumed uniform, and the overall heat transfer coefficient is treated as constant along the flow direction in the baseline analytical comparison, as is customary in ideal counter-flow ε–NTU formulations [12].

The methods are structured in three stages: (i) theoretical formulation of the ε–θ framework, (ii) implementation strategy, including identification and prediction procedures, and (iii) validation against reference data and benchmark methods.

2.1 Effectiveness–Thermal Length (ε–θ) Method

The classical thermal length is defined as $\theta=UA/C_{ref}$, and in the UA-independent formulation we work with an identified thermal length θ^* (obtained from calibration) and a UA-free thermal-length proxy $r=A/C_{min}$ for parametric studies.

In classical ε–NTU analysis, the thermal length θ is defined as $\theta=UA/C_{ref}$, where U is the overall heat transfer coefficient, A the effective heat transfer area, and C_{ref} a chosen heat-capacity rate. It can therefore be interpreted as a dimensionless measure of how much "heat transfer potential" the exchanger provides relative to the heat capacity of the streams. In the present UA-independent formulation, θ^* plays an analogous role but is identified directly from performance data rather than computed from an explicit UA. Physically, θ^* represents an exchanger-specific thermal length that lumps together geometry, correlations and operating conditions into a single effective conductance measure: larger values of θ^* correspond to a higher effective ability of the exchanger to approach the maximum possible heat transfer for the given flow arrangement.

The validity of θ^* is, however, limited to the regime in which it is identified. In this study, θ^* is calibrated for single-pass, counter-current, single-phase water operation within a given Reynolds-number and temperature range and for a specific plate pattern. Extrapolating θ^* far beyond these conditions (e.g. to different flow configurations, markedly different Reynolds numbers or fluids) may lead to loss of accuracy, and additional calibration or validation would be required in such cases.

2.1.1 Theoretical Framework and Rationale

The starting point is the classical definition of heat exchanger effectiveness:

$$\varepsilon = \frac{Q}{Q_{max}} \tag{1}$$

Where Q is the actual heat transfer [W] while the subscript *max* is referring to the maximum possible heat transfer rate, defined as:

$$Q_{max} = C_{min}\left(T_{h,in} - T_{c,in}\right) \tag{2}$$

Where T is the temperature [K] with subscripts *h,in* and *c,in* referring to hot- and cold-stream in, respectively and the minimum heat capacity rate C_{min} obtained as the smallest from:

$$C_{min} = min\left(\dot{m}_h c_{p,h}, \dot{m}_c c_{p,c}\right) \tag{3}$$

Where $\dot{m}$ is the mass flow rate [kg/s] while c_p is the specific heat at constant pressure [J/kgK] with subscripts h and c being for hot- and cold-stream respectively.

In the classical ε–NTU method, effectiveness is expressed as a function of the number of transfer units ($NTU = UA/C_{min}$ [–]) and the capacity rate ratio ($C_r = C_{min} / C_{max}$ [-]). While widely used, this approach presupposes knowledge of the overall heat transfer coefficient U [W/m^{2}K] and the effective heat transfer area A [m^2],

which are rarely available in manufacturer data. This reliance represents a critical limitation for performance prediction in practical settings such as district heating substations or industrial plate heat exchangers.

To overcome this limitation, we reformulate the effectiveness relation in terms of a thermal length parameter (θ), as defined in Equation 4 :

$$\varepsilon(\theta, C_r) = \frac{1-exp[-\theta(1-C_r)]}{1-C_r exp[-\theta(1-C_r)]} \quad (4)$$

Where the thermal length θ (Equation 5) is classically defined by basing on the reference heat capacity rate C_{ref}[W/K];

$$\theta = UA/C_{ref} \quad (5)$$

Instead of computing θ from geometric and thermal design parameters, this study introduces an identification procedure in which θ is inferred directly from a calibration data point (i.e., from known inlet/outlet states and flow rates).

This modification is both the strength and the limitation of the proposed approach. By identifying θ directly, the model eliminates the need for elusive U and A values, making it directly usable with manufacturer data. However, it also transforms θ into a grey-box parameter that absorbs the combined effects of geometry, surface enhancement, and flow distribution. This means that, unlike *NTU*, θ is no longer strictly tied to physical exchanger design but is instead an operationally identifiable signature.

The rationale behind this reframing is twofold:

(i) This approach aligns with real-world availability of data, enabling predictive use where classical approaches fail.

(ii) Once θ is identified for a given exchanger, it can be applied across a range of operating conditions to predict outlet temperatures and return temperatures, particularly on the primary side of district heating exchangers.

Nevertheless, the method is not without risks. If fluid properties or operating regimes change substantially (e.g., transitional to turbulent flow), a single θ identified from one calibration point may not remain invariant.

2.1.2 Implementation Strategy

The implementation of the proposed Effectiveness–Thermal Length (ε–θ^*) framework follows a systematic workflow that couples data-driven identification with first-principles thermal relations. The approach transforms incomplete manufacturer or experimental datasets into a predictive tool capable of estimating outlet and return temperatures without requiring explicit knowledge of the overall heat-transfer coefficient U [W/m²K] or effective area A [m²]. Each stage of the workflow (data acquisition, parameter identification, prediction, and validation) is described below:

2.1.2.1 Data Acquisition and Preprocessing

For each exchanger, a single operating point is used for model calibration. The required inputs are:

- Hot- and cold-stream inlet temperatures $T_{h,in}$, $T_{c,in}$[K];
- Hot- and cold-stream mass-flow rates $\dot{m}_h$, $\dot{m}_c$ [kg/s];
- At least one measured outlet temperature (typically $T_{h,out}$[K]);
- Fluid properties: density ρ [kg/m³] and specific heat c_p [J/kgK].

All quantities are converted to SI base units and verified for physical consistency. The hot-side heat-transfer rate is first computed as with Equation 6 .

$$Q_{meas} = \dot{m}_h c_{p,h}\left(T_{h,in} - T_{h,out}\right) \quad (6)$$

and the corresponding measured effectiveness is determined from Equation 7.

$$\varepsilon_{meas} = \frac{Q_{meas}}{C_{min}(T_{h,in}-T_{c,in})} \quad (7)$$

where C_{min} is obtained via Equation 3.

2.1.2.2 Identification of the Heat Exchanger Signature (θ^*)

The effectiveness relation for counter-flow configuration is expressed with Equation 4.

Instead of calculating $\theta = UA/C_{ref}$ from available geometric or design data, the thermal length signature θ^* is identified by numerically inverting the above equation so that:

$$\varepsilon(\theta^*, C_r) = \varepsilon_{meas} \quad (8)$$

The resulting θ^*[-] is a dimensionless invariant representing the integrated thermo-hydraulic behaviour of the exchanger under reference conditions. It encapsulates geometry, flow arrangement, and surface enhancement effects, thereby serving as a data-derived exchanger fingerprint. This calibration step is intentionally minimalistic: a single measurement point suffices, ensuring that the framework remains applicable even to limited manufacturer datasets.

2.1.2.3 Prediction of New Operational Conditions

For any new operating condition j, the following sequence is applied:

1. Recomputing the capacity parameters via Equation 9.

$$C_{min}{}^{(j)} = min\left(\dot{m}_h{}^{(j)} c_{p,h}, \dot{m}_c{}^{(j)} c_{p,c}\right) \quad (9)$$
$$C_r{}^{(j)} = C_{min}{}^{(j)} / C_{max}{}^{(j)}$$

2. Evaluating the predicted effectiveness by use of Equation 10.

$$\varepsilon^{(j)} = \varepsilon\left(\theta^*, C_r{}^{(j)}\right) \quad (10)$$

3. Computing the total heat transfer rate with Equation 11 .

$$Q^{(j)} = \varepsilon^{(j)} C_{min}{}^{(j)}\left(T_{h,in}{}^{(j)} - T_{c,in}{}^{(j)}\right) \quad (11)$$

4. Prediction of the outlet temperatures by use of the energy conversions Equation 12.

$$T_{h,out}{}^{(j)} = T_{h,in}{}^{(j)} - \frac{Q^{(j)}}{\dot{m}_h{}^{(j)} c_{p,h}} \quad (12)$$
$$T_{c,out}{}^{(j)} = T_{c,in}{}^{(j)} - \frac{Q^{(j)}}{\dot{m}_c{}^{(j)} c_{p,c}}$$

The primary return temperature, a key metric for district-heating performance assessment, is, by this way, determined directly from the predicted $T_{h,out}$ at each condition j. Because the same invariant parameter θ^* is employed for all operating conditions, the approach provides a computationally lightweight yet general predictive model, suitable for iterative simulations or digital-twin applications.

2.1.2 Model Verification

The predictive accuracy of the formulation was quantified using the measured outlet temperatures as reference values. The Mean Absolute Error (MAE) and Root-Mean-Square Error (RMSE) were computed as:

$$MAE = \frac{1}{N}\sum_{i=1}^{N}\left|T_{out,i}^{pred} - T_{out,i}^{meas}\right| \quad (13)$$

$$RMSE = \sqrt{\frac{1}{N}\sum_{i=1}^{N}\left(T_{out,i}^{pred} - T_{out,i}^{meas}\right)^2}$$

2.2 Log Mean temperature Difference (LMTD) Method

The Log Mean Temperature Difference (LMTD) method represents the classical analytical framework for steady-state performance prediction of single-phase heat exchangers. It establishes the thermodynamic relationship between the overall heat-transfer rate, the mean driving temperature difference across the exchanger surface, and the overall conductance of the system. Despite its conceptual simplicity, the LMTD formulation provides a rigorous benchmark for evaluating more advanced approaches such as the ε–NTU and ε–θ methods.

2.2.1 Governing Energy Balance

For a differential element of area dA along the heat-transfer surface, the local heat-flux balance between the hot and cold fluid streams is expressed as:

$$d\dot{Q} = UdA(T_h - T_c) \quad (14)$$

where U [W/m²K] is the overall heat-transfer coefficient, T_h and T_c [K] denote the local bulk temperatures of the hot and cold fluids, respectively, and $\dot{Q}$ [W] is the total heat-transfer rate. Integration over the total heat-transfer area A yields:

$$\dot{Q} = UA\Delta T_m \quad (15)$$

where ΔT_m [K] is the appropriate mean temperature difference between the two fluids.

For finite inlet and outlet temperatures, the rate of heat transfer must simultaneously satisfy the energy balances of both fluids:

$$\dot{Q} = \dot{m}_h c_{p,h}\left(T_{h,in} - T_{h,out}\right) = \dot{m}_c c_{p,c}\left(T_{c,out} - T_{c,in}\right) \quad (16)$$

with $\dot{m}$ [kg/s] denoting the mass-flow rate and c_p [J/kgK] the specific heat capacity at constant pressure.

2.2.2 Derivation of the Log-Mean Temperature Difference

For steady-state, single-phase flow with constant U and negligible axial conduction, the temperature difference between the two fluid streams varies exponentially along the flow path. Considering an infinitesimal area element and dividing Equation 14 by Equation 16 yields:

$$\frac{dT}{\Delta T} = -\frac{U\, dA}{C} \quad (17)$$

where $C = \dot{m}\, c_p$ is the heat-capacity rate of the fluid.

Integrating Equation 17 from inlet to outlet temperatures results in:

$$\Delta T_m = \frac{\Delta T_1 - \Delta T_2}{ln\left(\frac{\Delta T_1}{\Delta T_2}\right)} \quad (18)$$

which defines the logarithmic mean temperature difference, LMTD.

To account for flow deviations from ideal counter- or parallel-flow (e.g., multi-pass or cross-flow PHEs), a geometric correction factor F ($0 < F \leq 1$) is introduced:

$$\dot{Q} = UAF\Delta T_{lm} \quad (19)$$

2.2.3 Determination of the Overall Conductance (UA)

The global conductance UA [W/K] quantifies the total heat-transfer capability of the exchanger and is computed for each operating point from measured data as:

$$UA = \frac{\dot{Q}}{F\Delta T_{lm}} \quad (20)$$

where $\dot{Q}$ is obtained from Equation 16.

This formulation enables an empirical determination of UA_i for every recorded condition, thereby capturing variations due to flow rate, temperature level, and fluid-property changes. The resulting UA_i distribution defines the "thermal signature" of the exchanger, which is subsequently used to predict outlet temperatures under unseen operating scenarios.

2.2.4 Prediction of Outlet Temperatures

Given U, A, F, and the inlet conditions, the LMTD model is solved iteratively to determine the outlet temperatures that simultaneously satisfy Equation 15 and Equation 16 . For each data point i:

1. Initialize by guessing $T_{h,out}$ and $T_{c,out}$.
2. Evaluate $\Delta T_{lm,i}$ using Equation 18 with counter- or parallel-flow definitions.
3. Compute the total heat-transfer rate via Equation 19.
4. Update outlet temperatures from the energy balances:

$$T_{h,out} = T_{h,in} - \frac{\dot{Q}_i}{\dot{m}_h c_{p,h}} \quad (21)$$
$$T_{c,out} = T_{c,in} + \frac{\dot{Q}_i}{\dot{m}_c c_{p,c}}$$

5. Iterate until convergence in $\dot{Q}$ and temperature differences, all satisfied.

The method yields the predicted outlet temperatures $T_{h,out}$ and $T_{c,out}$, along with the instantaneous heat-transfer rate $\dot{Q}$.

2.3 Effectiveness–NTU (ε–NTU) Method

The effectiveness–Number of Transfer Units (ε–NTU) method constitutes an alternative analytical framework to the classical LMTD formulation for determining the steady-state thermal performance of heat exchangers. Unlike the LMTD approach (which requires prior knowledge of all inlet and outlet temperatures) the ε–NTU method directly relates the exchanger's geometry and conductance to its thermal effectiveness. This property makes the method particularly suitable for predictive modelling, design optimization, and performance comparison when outlet temperatures are unknown.

2.3.1 Fundamental Relations

In the ε–NTU framework, the effectiveness ε of a heat exchanger is defined as the ratio of the actual heat transfer to the maximum possible heat transfer that would occur if one of the fluids were to reach the inlet temperature of the other:

$$\varepsilon = \frac{\dot{Q}}{\dot{Q}_{max}} = \frac{\dot{Q}}{C_{min}\left(T_{h,in} - T_{c,in}\right)} \quad (22)$$

Where C is the heat-capacity rate of each stream with;

$$C_{min} = min(C_h, C_c) \text{ and } C_{max} = max(C_h, C_c);\ C_r = C_{min}/C_{max} \quad (23)$$

The exchanger geometry and heat-transfer characteristics are embedded in the number of transfer units (NTU), which quantifies the relative size or heat-transfer potential of the exchanger:

$$NTU = \frac{UA_{eff}}{C_{min}},\ UA_{eff} = UAF \quad (24)$$

Here U [W/m²K] denotes the overall heat-transfer coefficient, A [m²] the total effective area, and F the flow-arrangement correction factor. For the present analysis, UA was determined empirically for each operating point as described in Section 2.2.3, ensuring consistency with the LMTD-based characterization.

2.3.2 Analytical Expressions for ε–NTU

Closed-form correlations exist between ε, NTU, and C_r for standard flow configurations [2]. For parallel-flow heat exchangers:

$$\varepsilon_{parallel} = \frac{1 - exp[-NTU(1+C_r)]}{1+C_r} \quad (25)$$

whereas for counter-flow arrangements:

$$\varepsilon_{counter} = \frac{1 - exp[-NTU(1-C_r)]}{1 - C_r exp[-NTU(1-C_r)]} \quad (26)$$

In the limiting case $C_r \rightarrow 1$, Equation 26 simplifies to:

$$\varepsilon = \frac{NTU}{1+NTU} \quad (27)$$

These relations describe the intrinsic thermodynamic effectiveness independent of the absolute temperature levels and are valid for single-phase, steady-state conditions with constant fluid properties.

2.3.3 Prediction of Outlet Temperatures

Once the effectiveness ε is evaluated from Equation 25, Equation 26, or Equation 27, the total heat transfer follows directly from Equation 22:

$$\dot{Q} = \varepsilon C_{min}\left(T_{h,in} - T_{c,in}\right) \quad (28)$$

The corresponding outlet temperatures are determined from the energy balances of each fluid:

$$T_{h,out} = T_{h,in} - \frac{\dot{Q}}{C_h} \text{ and } T_{c,out} = T_{c,in} + \frac{\dot{Q}}{C_c} \quad (29)$$

Equations Equation 24–Equation 29 form a compact predictive model in which the only required inputs are the inlet temperatures, mass-flow rates, and the global conductance UAF. The model can thus be applied at each recorded operating condition to estimate the outlet temperatures.

2.3.4 Numerical Implementation

Basing on the ε–NTU algorithm, for each observation i:

1. Compute C_h, C_c, C_{min}, C_{max}, C_r from mass-flow rates and specific heats.
2. Evaluate UA_i from measured data.
3. Determine NTU_i.
4. Calculate ε_i using the appropriate analytical expression (Equation 25 or Equation 26).
5. Compute the heat-transfer rate and outlet temperatures using Equation 28 and Equation 29.

3. RESULTS AND DISCUSSION

All code used in this study, including the UA-independent ε–θ (ETL-CF), ε–NTU, and LMTD implementations and example scripts, is openly available at the DH-HeatExchanger repository given at the reference [17].

3.1 Baseline Predictions

The baseline analysis was performed for a single-pass, counter-current plate heat exchanger using water as the working fluid under steady-state conditions. The inlet temperatures were fixed at 70 °C on the primary (hot) side and 20 °C on the secondary (cold) side, with nominal mass flow rates of 1.50 kg/s and 1.20 kg/s,

respectively. The specific heat capacity of water was assumed constant at 4180 J/kgK, and the total overall heat transfer conductance (UA) was taken as 8 kW/K (as a reference basis).

The relationship between thermal effectiveness (ε) and the number of transfer units (NTU) is illustrated in **Figure 1**. The solid curves correspond to the analytical ε–NTU formulation for an ideal counter-flow configuration, whereas the dashed curves represent the results obtained from the segment-wise ε–θ (Effectiveness–Thermal Length) formulation implemented in this study. Each color pair (solid and dashed of the same hue) denotes a constant heat-capacity-rate ratio (C^*), ranging from 0.25 to 1.0.

For all C^* levels, both formulations exhibit the expected monotonic increase of ε with NTU in the low-to-moderate transfer-unit regime (NTU $\lesssim$ 2). As NTU increases, the slope of ε gradually diminishes, approaching the asymptotic limit of unity for the perfectly balanced case ($C^* = 1$) and a finite plateau for smaller ratios. The ε–θ curves reproduce the characteristic behaviour of the analytical ε–NTU relation with excellent agreement up to intermediate NTU values, validating the consistency of the discretised thermal-length formulation for steady-state counter-current operation.

At higher NTU values (NTU > 3), the ε–θ predictions slightly diverge from the analytical solution, showing a marginal reduction in effectiveness, particularly for small capacity-rate ratios. This deviation originates from the discrete-segment representation of the exchanger and the finite-area correction implicitly included in the ε–θ framework, whereas the analytical ε–NTU curves assume an ideal, continuously distributed *UA*. In the parameter space shown, the difference in ε remains limited to a few percentage points and corresponds to outlet-temperature deviations on the order of hundredths of a kelvin for typical district-heating temperature spans. The figure also demonstrates the pronounced influence of the heat-capacity-rate ratio. As C^* decreases from 1.0 to 0.25, the attainable effectiveness at a given NTU declines due to the growing asymmetry between the two fluid streams. For instance, at NTU ≈ 2, ε falls from approximately 0.85 for $C^* = 1.0$ to ≈ 0.65 for $C^* = 0.25$, consistent with classical counter-flow theory. These baseline predictions therefore confirm that the implemented ε–θ approach reliably reproduces the canonical ε–NTU response over the entire range of practical design conditions and forms a valid foundation for the subsequent validation and parametric analyses presented in the following sections.

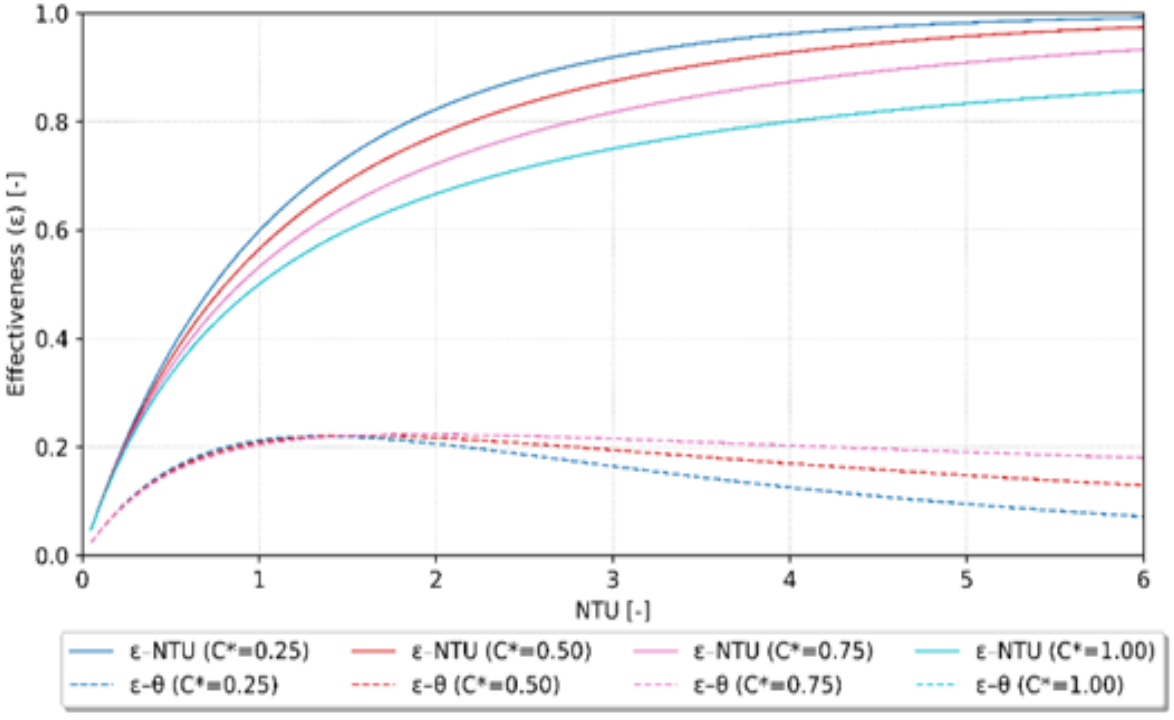

Figure 1. Thermal effectiveness (ε) versus number of transfer units (NTU) for counter-current, single-pass heat exchangers at different heat-capacity-rate ratios C*. Solid lines show the analytical ε–NTU relations, and dashed lines the ε–θ (Effectiveness–Thermal Length) predictions.

3.2 Validation Against Reference Data

The ε–θ (Effectiveness–Thermal Length) formulation was validated against manufacturer reference data obtained from the SWEP [18] online catalogue (for B8Tx20), encompassing more than 124,819 operational points across a wide range of flow and temperature conditions. The operating conditions span primary-side mass flow rates between 2.99×10^{-5} and 1.20×10^{-3} kg·s⁻¹ and secondary-side mass flow rates between 3.02×10^{-5} and 2.39×10^{-3} kg·s⁻¹. Primary inlet and outlet temperatures lie in the ranges 25–100 °C and 20–98 °C, respectively, while secondary inlet and outlet temperatures vary between 20–98 °C and 24–99 °C. The corresponding heat transfer rates cover approximately 0.01–40 kW, remaining within a strictly single-phase liquid regime without phase change.

Each data entry provided inlet and outlet temperatures, flow rates, and calculated heat duties for water–water plate heat exchangers. To ensure a consistent comparison, the overall heat transfer coefficient–area product (UA) was derived directly from the catalogue data using the LMTD method and subsequently applied to all three evaluation frameworks (ε–NTU, ε–θ, and LMTD) under identical thermophysical conditions.

Figure 2 presents the mean and standard deviation of the absolute prediction error in the cold-side outlet temperature ($T_{c,out}$) as a function of the number of transfer units (NTU). Across the entire NTU range (0–200), the mean deviation remains below 0.05 K, gradually decreasing with increasing NTU. The low dispersion reflects the high internal consistency of the catalogue data and the strong agreement among the three analytical formulations.

The three methods yield practically indistinguishable results: the ε–θ (red dashed) and ε–NTU (blue dotted) curves are fully superimposed on the LMTD (green solid) curve. This overlap demonstrates the mathematical equivalence of the ε–θ formulation to the conventional ε–NTU and LMTD relations when evaluated under steady-state, single-pass counter-current conditions using identical UA values. Minor deviations observed at very low NTU values (<10) originate from numerical sensitivity in the logarithmic mean temperature difference and the discrete-segment representation used in the ε–θ model. Overall, the validation confirms that the ε–θ framework reproduces the conventional thermal performance predictions with negligible error, establishing its reliability for steady-state applications and forming a solid foundation for subsequent parametric and dynamic analyses.

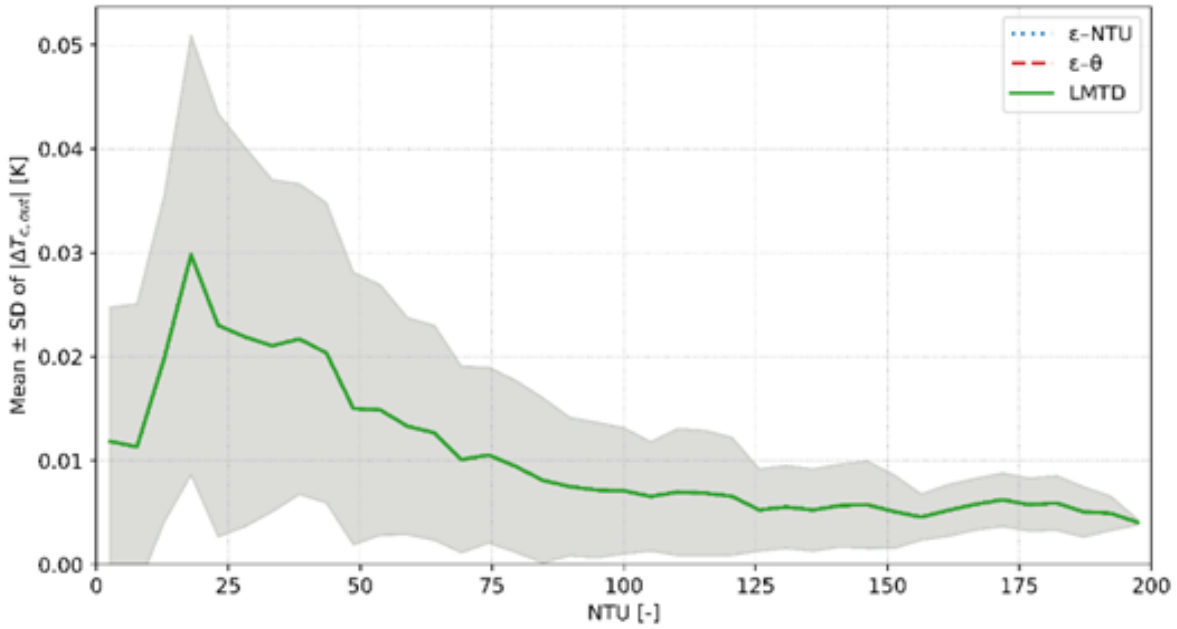

Figure 2. Mean and standard deviation of the absolute prediction error in the cold-side outlet temperature ($T_{c,out}$) as a function of NTU for ε–NTU (blue dotted), ε–θ (red dashed), and LMTD (green solid) formulations. The near-perfect overlap of all three curves indicates their equivalence under identical steady-state conditions with catalogue-based UA values. The shaded region denotes ±1 standard deviation around the LMTD mean

3.3 Methodological Contrast

This subsection compares the three rating paradigms (LMTD, ε–NTU, and the proposed ε–θ (ETL-CF)) under controlled operating envelopes without recourse to catalogue UA. To isolate model-form effects, overall conductance is generated from a standard single-phase chevron-plate correlation given in Equation 30.

$$Nu = C\,Re^{n}Pr^{1/3},\ h = \frac{Nu\,k}{D_h},\ \frac{1}{U} = \frac{1}{h_h} + \frac{\delta}{k_{wall}} + \frac{1}{h_c} \tag{30}$$

The hydraulic diameter is assumed to be $D_h \simeq 2b$. The ε–NTU and LMTD methods then base on Equation 30 while the ε–θ method remains UA-free and is driven by the thermal-length proxy $r = A / C_{min}$ with the previously identified $\alpha(C^*)$ and $\beta(C^*)$ coefficients obtained. Water properties are held constant (district-heating temperature range), and geometry/flow "knobs" (area A, gap b, number of parallel channels m, and the correlation constants C, n) are varied across three presets to span low-, mid-, and high-NTU regimes.

To make the regimes explicit, the NTU distribution within each preset is partitioned into three equal-count bands (tertiles): band 1 (lowest NTU), band 2 (middle), band 3 (highest NTU). Within each band, cases are further grouped by the capacity-rate ratio C^*, and we report the mean absolute deviation in cold-side outlet temperature, $|\Delta T_{c,out}|$, of each comparator against ε–NTU. In other words, each marker in Figure 3 represents the average behaviour of a cluster of simulations sharing the same NTU band and lying within a narrow C^* interval, which compresses the full parametric cloud into a small number of representative bands and highlights systematic trends.

Differences are concentrated in the low-NTU band, where ε is most sensitive to thermal length. There, $|\Delta T_{c,out}|$ for ETL-CF relative to ε-NTU increases monotonically with C^* and can reach several kelvin as C^* reaches to 1. In the mid-NTU band, discrepancies are an order of magnitude smaller but remain detectable near $C^* \geq 0.7$. In the high-NTU band, all methods converge as ε reaches to 1 and $|\Delta T_{c,out}|$ reaches to 0.

At fixed NTU band, the model spread grows with C^*. This is consistent with both the ε–NTU structure (which collapses to a single-stream limit as C^* reaches to 1) and the ε–θ mapping (whose $r = A / C_{min}$ dependence amplifies as C_{min} approaches C_{max}).

In district-heating plate heat exchangers that typically operate at NTU $\gtrsim$ 3, the proposed ε–θ framework tracks ε–NTU/LMTD closely for moderate C^*. The largest practical divergence arises for low-NTU designs with high C^* (e.g., highly balanced streams sized tightly on approach temperature). In such cases, the UA-free ε–θ prediction of return temperature may differ by up to a few kelvins; conversely, ε–NTU/LMTD require a reliable UA (or correlation) that may not be available during early-stage design. The banded representation therefore clarifies

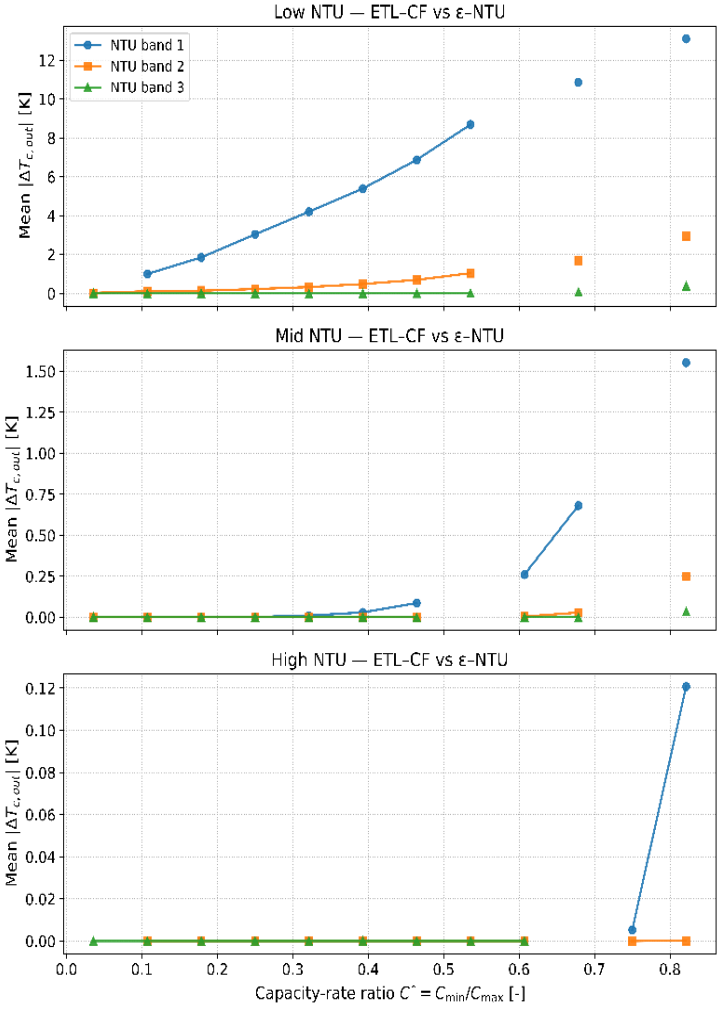

Figure 3. Methodological contrast: ETL-CF (ε–θ) vs ε–NTU across NTU regimes – within each regime the data are partitioned into NTU bands (markers): band 1 = lowest tertile of NTU (approach-limited), band 2 = middle tertile, band 3 = highest tertile (near-plateau).

where the UA-free approach is most/least interchangeable with UA-based methods and guides which model to trust for quick sizing versus detailed rating.

3.4 Parametric Analysis

Figure 4 and Figure 5, respectively, examine the sensitivity of the ε–θ (ETL-CF) model to (i) the per-channel Reynolds number of the C_{min} stream, at fixed thermal area, and (ii) the thermal length $r = A / C_{min}$, each evaluated for representative capacity-rate ratios $C^* \in \{0.25,0.50,0.75,0.90\}$. Water properties are treated as constant (district-heating range), the exchanger is single-pass counter-current, and the ETL-CF coefficients $\alpha(C^*)$ and $\beta(C^*)$ are those identified earlier. In Figure 4, Reynolds number is varied by scaling both stream mass flow rates simultaneously while holding area constant; in Figure 5, r is varied directly.

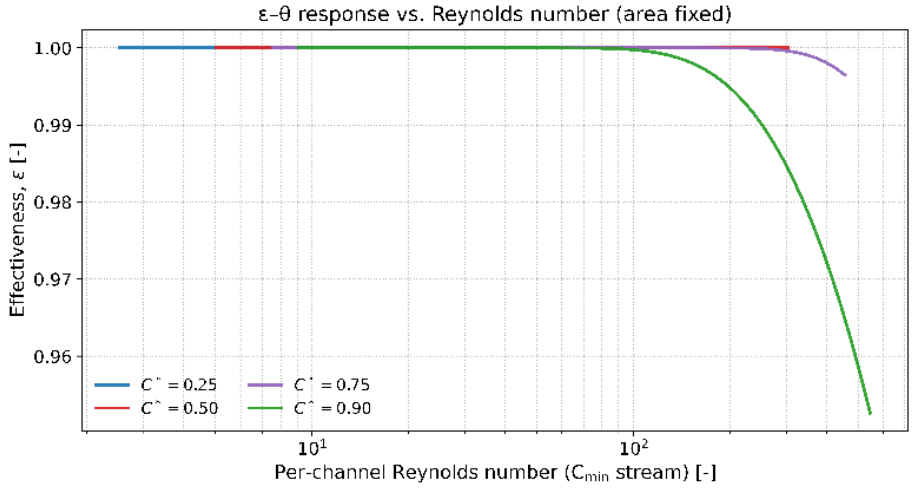

Figure 4. ε–θ response vs. Reynolds number (area fixed).

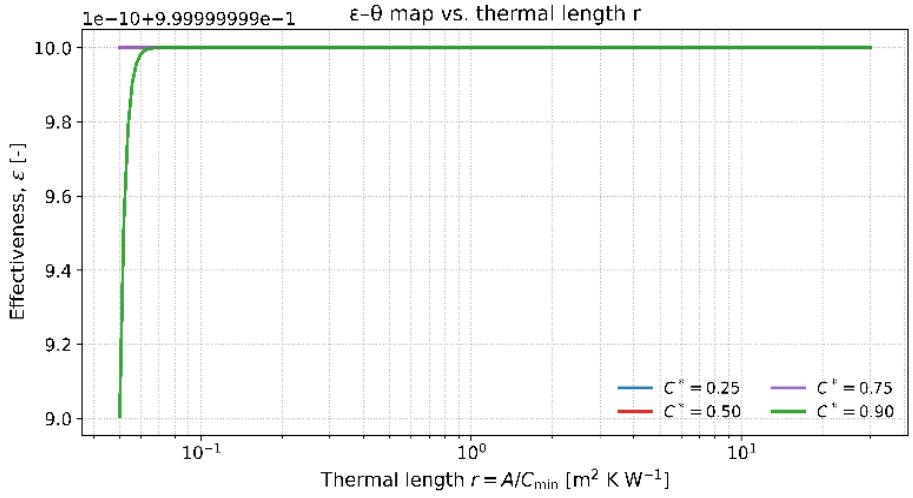

Figure 5. ε–θ map vs. thermal length r

Across all C^* levels in Figure 4, the effectiveness remains very high and varies only at the sub-percent level. As the Reynolds number increases, ε exhibits a mild decline, most evident for the balanced case $C^* = 0.90$ (green curve), where ε falls by only a few parts in 10^{-3} over more than an order of magnitude in Re. This trend is consistent with the inverse coupling between Re and thermal length under fixed area: increasing flow raises Re but also increases C_{min}, thereby reducing r, and marginally lowering ε. For more imbalanced conditions (e.g., $C^* = 0.25$), the sensitivity is even weaker because the approach to the ε plateau is governed primarily by the smaller stream and is less affected by symmetric flow escalation.

As can be seen in Figure 5, The ε–θ map versus r reveals the expected rapid approach to the effectiveness plateau. For all C^*, ε rises steeply at small r and quickly saturates, with ε essentially unity once r exceeds a modest threshold. At fixed r, higher C^* (more balanced streams) yields a slightly lower ε, reflecting the greater thermal duty required of the minimum-capacity stream as $C^* \to 1$; however, within the range examined the differences are again at the 10^{-3} level. Combining both panels, the model behaves consistently with the physical interpretation of r as a thermal-sizing parameter: any operating change that increases r (larger area or smaller C_{min}) moves the exchanger rapidly into the near-ideal regime, whereas changes that decrease r (higher flows at fixed area) produce only minor departures from unity ε for the present geometries. In the parameter envelope typical of building and district-heating plate heat exchangers, ε–θ predicts negligible effectiveness penalties over broad ranges of Reynolds number once a moderate thermal length is provided. The dominant design lever is therefore r (sizing relative to C_{min}), with C^* acting as a weak modulator. Practically, this means that for the studied configurations, return-temperature performance is robust to flow-rate variability when area is adequate; conversely, intentional reductions in area (or large increases in flow) impact ε only at the per-mille level unless r is driven into the small-r regime. These trends substantiate the ε–θ framework's ability to capture regime-dependent behaviour—linking operational (Re), sizing (r), and load-split (C^*) effects in a compact, predictive mapping.

4. SUMMARY

This study introduced and interrogated a U-independent Effectiveness–Thermal Length framework (ε–θ) for steady-state prediction of heat-exchanger performance with water in single-phase heating applications, using plate heat exchangers (PHEs) as the primary use case. The central innovation is to replace the explicit dependence on UA with a thermal-length mapping that links effectiveness to $r = A / C_{min}$, modulated by empirically identified, capacity-ratio–dependent coefficients $\alpha(C^*)$ and $\beta(C^*)$. The framework is deliberately lightweight—suitable for rapid rating/prediction, parametric exploration, and system-level studies—while remaining rooted in first-principles energy balances.

Three complementary strands of evidence were implemented:

1. Baseline predictions demonstrated that ε–θ reproduces the canonical ε–NTU behavior across $C^* \in [0.25,1]$, including the expected monotonic rise of ε with *NTU* and the diminishing sensitivity at large *NTU*.

2. Methodological contrast and parametric analysis decoupled model-form effects from data by generating *UA* via standard chevron-plate heat-transfer correlations and by exploring operating envelopes without borrowing *UA* directly from manufacturer data. Two robust patterns emerged:

    a. Regime dependence: differences among methods are largest at low *NTU* and high C^* (balanced streams), where ε is most sensitive to thermal length and approach temperature. As *NTU* grows, all methods converge rapidly ($\varepsilon \to 1$).

    b. Control levers: thermal length r is the dominant design variable; once r is moderate, ε becomes insensitive to Reynolds-number changes produced by flow scaling at fixed area. In the district-heating envelope examined, return-temperature predictions are therefore robust to realistic flow variability when sizing is adequate.

Together, these strands show that ε–θ offers a compact, predictive mapping that (i) collapses to the classical results when fed the same physics, (ii) remains usable when *UA* is unavailable, and (iii) exposes where UA-free prediction can meaningfully differ from UA-based methods in early-stage sizing or limited-data contexts.

5. CONCLUSION

This study evaluated a UA-independent Effectiveness–Thermal Length (ε–θ) framework for single-phase, water-based plate heat exchangers and benchmarked it against ε–NTU and LMTD. Across baseline, validation, and parametric analyses, ε–θ reproduced classical predictions when conductance assumptions matched, and meaningful departures appeared only in low-NTU, high-C^* regimes. The key takeaways and design implications are summarized below:

- By parameterizing exchanger performance through $r = A / C_{min}$ and calibrated $\alpha(C^*)$ and $\beta(C^*)$, the ε–θ framework removes the need for explicit *UA* without sacrificing physical interpretability. For steady-state, single-phase water service in counter-current PHEs, ε–θ delivers outlet and return temperatures that are indistinguishable from ε–NTU/LMTD when the underlying conductance assumptions coincide.

- Noticeable deviations among ε–θ and UA-based methods emerge only in regimes where the exchanger is approach-limited: low *NTU* (undersized area or high flow at fixed area) and high C^* (balanced streams). In these cases, ε–θ can deviate by up to a few kelvins in predicted return temperature relative to ε–NTU/LMTD. This is precisely the region in which designers most need quick, UA-free assessments to gauge the impact of sizing and load split before detailed conductance modelling is available.

- Considering the design guidance for district heating PHEs, one can note that;

    - Prioritize thermal length in sizing; once r is moderate, the marginal benefit of additional area is small and the prediction becomes insensitive to Reynolds number over wide operating ranges.

    - For networks that target low return temperatures with high C^* and tight approach constraints, apply ε–θ as a rapid screening tool and, where decisions are sensitive, cross-check with ε–NTU/LMTD using a defensible *UA* (e.g., correlation plus fouling/arrangement factors).

    - In mid- to high-NTU operation (typical of well-sized substations), all methods converge; ε–θ is adequate on its own for simulation, optimization, and control tasks.

- The ε–θ workflow is deterministic and lean: constant-property water, closed-form effectiveness relations, and minimal numerical inversion for calibration. This makes it suitable for embedded use (selection tools, design optimizers, digital twins) where speed and stability are paramount.

Compared with classical LMTD and ε–NTU formulations, the proposed ε–θ framework offers a distinct advantage in situations where the overall conductance UA and detailed plate geometry are unknown, but catalogue-grade performance data are available. In such cases, LMTD and ε–NTU still require an assumed *UA*, whereas ε–θ operates directly on observable data via an identified thermal length and a UA-free thermal-length proxy $r = A/C_{min}$. When a common conductance assumption is imposed, ε–θ recovers ε–NTU/LMTD predictions with negligible outlet-temperature differences, confirming thermodynamic consistency. At the same time, its compact parameterisation in terms of r and C^* enables fast parametric studies with substantially lower data requirements than detailed correlation-based plate models. The method is therefore particularly advantageous for early-stage district-heating design, retrofit screening, and system-level simulations, where data frugality and computational efficiency are crucial.

While our analysis is deliberately scoped to single-phase water, steady-state operation, and single-pass counter-current plate heat exchangers, it does not yet encompass two-phase duties, strong temperature-dependent property variation, multi-pass/maldistribution effects, or transient wall–fluid capacitance. Moreover, the identified ε–θ modifiers $\alpha(C^*)$ and $\beta(C^*)$ function as a gray-box signature of the operating/geometry envelope; substantial departures in corrugation pattern, channel hydraulics, or regime (e.g., deep transitional shifts) may warrant re-identification or piecewise coefficients.

Within these bounds, we proposed and benchmarked a UA-independent Effectiveness–Thermal Length (ε–θ) framework against ε–NTU and LMTD. Across baseline, validation, and parametric studies, ε–θ recovers classical predictions when conductance assumptions align and departs meaningfully only in low-NTU, high-C^* conditions that are most sensitive to sizing and approach temperature. The concise conclusions and design implications follow.

From a practical standpoint, the following recommendations can be drawn from this study. For single-pass counter-current plate heat exchangers in the investigated operating range, the ε–θ framework may be used as a UA-independent surrogate whenever only catalogue-grade performance data (inlet/outlet temperatures, flow rates, heat duties) are available, but overall conductance and detailed geometry are unknown. In such cases, ε–θ is recommended for early-stage design, retrofit screening, and district-heating scenario analysis, as it reproduces ε–NTU/LMTD outlet temperatures to within O(10−2) K when a common conductance assumption is imposed.

Conversely, in applications where detailed plate geometry, fouling behaviour, maldistribution effects or transient dynamics are critical, classical ε–NTU/LMTD formulations combined with correlation-based plate models should remain the primary tools, and the ε–θ method should be used as a complementary reduced-order representation. Users are therefore encouraged to select between ε–θ and conventional methods based on the available data and the required level of detail: ε–θ for fast, UA-independent performance prediction in data-limited settings, and ε–NTU/LMTD with detailed correlations for high-fidelity design and diagnostic studies.

6. FUTURE WORK

Future work should first extend the ε–θ framework beyond the present single-pass, counter-current scope. A natural progression is to cover multi-pass and cross-flow arrangements by incorporating established correction factors (i.e., $F<1$) and to test families of chevron angles and corrugation patterns to assess the portability of the identified $\alpha(C^*)$ and $\beta(C^*)$ coefficients. In parallel, the treatment of non-idealities should be made explicit: representative fouling resistances, wall conduction terms, and simple maldistribution penalties can be embedded as multiplicative or additive modifiers to the thermal length r or, where appropriate, absorbed into updated α, β maps. These additions would enable systematic sensitivity studies against controlled experiments and clarify robustness margins for design.

A second priority is a dynamic extension of ε–θ. Coupling the steady mapping with low-order lumped thermal capacitance models for fluids and plates would capture start-up and load-following transients (particularly primary-side return overshoots) and make the method suitable for real-time control, supervisory optimization, and digital-twin applications. This dynamic layer should be calibrated with transient tests or high-fidelity simulations while preserving the computational economy that motivates ε–θ.

In addition, future work should address operating regimes where transient wall–fluid capacitance effects become non-negligible. Examples include start-up from cold conditions, rapid load-following or setpoint changes in district-heating substations, and frequent on/off cycling of the exchanger. In such cases, the present steady-state ε–θ formulation would need to be embedded in a low-order dynamic model that explicitly represents wall and fluid heat capacities in order to capture the short-time evolution of outlet and return temperatures.

Finally, broadening the domain of application will increase the framework's practical value. Mixtures relevant to district heating and cooling (e.g., glycol–water and brines) can be accommodated by consistent thermophysical property models, while extensions to condensation or evaporation duties may be possible by defining a generalized, regime-aware "thermal length" across phase regions. To standardize evaluation, we advocate an open set of benchmark cases (geometry plus operating envelopes) and clear performance targets (for example, $|\Delta T_{return}| <$ 0.5 K at mid–high *NTU* and <2 K at low *NTU* with $C^* > 0.8$) so that ε–θ, ε–NTU/LMTD, and discretized models can be compared on common ground.

REFERENCES

[1] S. Kakaç, H. Liu, and A. Pramuanjaroenkij, Heat Exchangers: Selection, Rating, and Thermal Design, 3rd ed. Boca Raton, FL, USA: CRC Press, 2012.

[2] A. L. London, Compact Heat Exchangers. New York, NY, USA: Hemisphere Publishing Corporation, 1990.

[3] H. İ. Tol and S. Svendsen, "Improving the dimensioning of piping networks and network layouts in low-energy district heating systems connected to low-energy buildings: A case study in Roskilde, Denmark," Energy, vol. 38, pp. 1–10, 2012, doi: 10.1016/j.energy.2011.12.002.

[4] H. İ. Tol and S. Svendsen, "A comparative study on substation types and network layouts in connection with low-energy district heating systems," Energy Convers. Manag., vol. 64, pp. 1–10, 2012, doi: 10.1016/j.enconman.2012.04.022.

[5] H. Kinnunen, "Performance of a District Heating Substation in Low Temperature District Heating," Ph.D. dissertation, Lappeenranta Univ. of Technology, Lappeenranta, Finland, 2019.

[6] V. S. Gullapalli, "Estimation of Thermal and Hydraulic Characteristics of Compact Brazed Plate Heat Exchangers," Ph.D. dissertation, Lund Univ., Lund, Sweden, 2013.

[7] S. Gusew, "Heat transfer in plate heat exchangers in the transition flow regime," J. Enhanced Heat Transfer, vol. 22, pp. 441–455, 2015, doi: 10.1615/JEnhHeatTransf.2016015947.

[8] T. Gao, B. G. Sammakia, J. F. Geer, A. Ortega, and R. Schmidt, "Dynamic analysis of cross flow heat exchangers in data centers using transient effectiveness method," IEEE Trans. Compon. Packag. Manuf. Technol., vol. 4, pp. 1925–1935, 2014, doi: 10.1109/TCPMT.2014.2369256.

[9] H. Lund, S. Werner, R. Wiltshire, S. Svendsen, J. E. Thorsen, F. Hvelplund, and B. V. Mathiesen, "4th Generation District Heating (4GDH). Integrating smart thermal grids into future sustainable energy systems," Energy, vol. 68, pp. 1–11, 2014, doi: 10.1016/j.energy.2014.02.089.

[10] H. Averfalk and S. Werner, "Essential improvements in future district heating systems," in Proc. 15th Int. Symp. District Heating and Cooling, Seoul, South Korea, 2016, pp. 194–200. [Online]. Available: http://www.iea-dhc.org/...

[11] M. Fernández-Torrijos, J. A. Almendros-Ibáñez, C. Sobrino, and D. Santana, "ε-NTU relationships in parallel-series arrangements: Application to plate and tubular heat exchangers," Appl. Therm. Eng., vol. 99, pp. 1119–1132, 2016, doi: 10.1016/j.applthermaleng.2016.02.003.

[12] L. Wang, B. Sundén, and R. M. Manglik, Plate Heat Exchangers: Design, Applications and Performance. Southampton, UK; Boston, MA, USA: WIT Press, 2007.

[13] H. Sammeta, K. Ponnusamy, M. A. Majid, and K. Dheenathayalan, "Effectiveness charts for counter flow corrugated plate heat exchanger," Simul. Model. Pract. Theory, vol. 19, pp. 777–784, 2011, doi: 10.1016/j.simpat.2010.10.012.

[14] S. P. Grétarsson, P. Valdimarsson, and V. K. Jónsson, "Heat transfer modelling of a plate radiator for district heating applications," Int. J. Energy Res., vol. 15, pp. 301–315, 1991, doi: 10.1002/er.4440150406.

[15] A. D. Wright and P. J. Heggs, "Rating calculation for plate heat exchanger effectiveness and pressure drop using existing performance data," Chem. Eng. Res. Des., vol. 80, pp. 309–312, 2002, doi: 10.1205/026387602753582105.

[16] M. Fernández-Torrijos, J. A. Almendros-Ibáñez, C. Sobrino, and D. Santana, "ε-NTU relationships in parallel-series arrangements: Application to plate and tubular heat exchangers," Appl. Therm. Eng., vol. 99, pp. 1119–1132, 2016, doi: 10.1016/j.applthermaleng.2016.02.003.

[17] H. İ. Tol, DH-HeatExchanger, GitHub Repository, 2025. doi: 10.5281/zenodo.17448215.

[18] SWEP International AB, SSP (version 2020.327.1) [Software], 2015. [Online]. Available: http://www.ssponline.swep.net/.